

**CHARACTERIZATION AND IMPROVEMENT OF DIFFERENTIAL ION MOBILITY  
SPECTROMETRY SEPARATIONS**

Brandon G. Santiago

A dissertation submitted to the faculty at the University of North Carolina at Chapel Hill in partial fulfillment of the requirements for the degree of Doctor of Philosophy in the Department of Chemistry.

Chapel Hill  
2016

Approved by:

Gary Glush

Mark Wightman

Michael Ramsey

Jeff Macdonald

Alexander Miller

© 2016  
Brandon G. Santiago  
ALL RIGHTS RESERVED

## **ABSTRACT**

Brandon G. Santiago: Characterization and Improvement of Differential Ion Mobility Spectrometry Separations  
(Under the direction of Gary L. Glish)

The high sensitivity and rapid analysis times of mass spectrometry have led to its importance as an analytical technique; however, low signal-to-background ratios and isomeric/isobaric interferences can be problematic during the analysis of complex mixtures. Separation techniques such as chromatography and electrophoresis are often coupled to mass spectrometry prior to ionization to reduce the complexity of the subsequent mass analysis but these separations are often the speed limiting step. Post-ionization separation techniques such as ion mobility spectrometry are much more rapid and can also be used prior to mass analysis, either as a stand-alone separation method or as a complementary separation step after a liquid phase separation.

At the low electric field strengths used in many ion mobility techniques the mobility of the ions is independent of the electric field strength used, and ions of the same charge state are separated based their collision cross-section. The work described herein couples differential ion mobility spectrometry (DIMS) separations to mass spectrometry. DIMS devices take advantage of the fact that ion mobility becomes dependent on electric field strength at high electric fields strengths ( $>10.0$  kV/cm). By alternating between low and high electric field strengths, DIMS devices separate ions based on the difference between their mobilities in low and high electric field strengths.

Many factors influence the separation achieved with DIMS devices. This work begins by examining the role of the mass spectrometer desolvation gas in keeping solvent vapors from entering the DIMS devices and affecting the DIMS separation. Work characterizing the intra-DIMS fragmentation of peptides is then described, including how the DIMS carrier gas temperature and composition affect the fragmentation of ions as they travel through a DIMS device. The improvement of DIMS separations via two distinct methods are then explained. The first is the use of a newly developed technique wherein the compensation field applied to the DIMS device and the amount of helium present in the DIMS carrier gas are scanned simultaneously. The second is the intentional addition of solvent vapors to the DIMS carrier gas, which is applied to the separation of four glucose isomers and also the separation of three phosphorylated hexose

“There’s been highs and lows, fast lane freeways and bumpy roads  
Cursed the devil and prayed to heaven, lost it all and we rolled some sevens  
There’s been more smiles then there’s been tears, been more good than bad years  
Ain’t it crazy baby how we got here”

## TABLE OF CONTENTS

LIST OF TABLES .....	xi
LIST OF FIGURES.....	xii
LIST OF ABBREVIATIONS AND SYMBOLS .....	xvii
CHAPTER 1: INTRODUCTION TO DIFFERENTIAL ION MOBILITY SPECTROMETRY ..	1
1.1. Introduction to Separations Prior to Mass Analysis.....	1
1.2. Introduction to Differential Ion Mobility Spectrometry .....	2
1.3. Methods to Improve DIMS Separations.....	6
1.4. Quantification of DIMS Separations.....	12
1.5. Summary .....	13
CHAPTER 2: EXPERIMENTAL.....	21
2.1 Materials.....	21
2.2 Ionization Techniques .....	23
2.3 Differential Ion Mobility Spectrometers and Mass Spectrometers .....	25
2.4 Major Modifications to the Standard Workflows/Experimental Set-ups.....	29

2.4.1. Chapter 3: Effects of Desolvation Gas Flow Rate and Temperature on DIMS Separations .....	29
2.4.2. Chapter 4: Characterization of Variables Affecting Internal Energy Deposition inside a Differential Ion Mobility Spectrometer .....	30
2.4.3. Chapter 5: Improved Differential Ion Mobility Spectrometry Separations using Linked Scans of Carrier Gas Composition and Compensation Field .....	31
2.4.5. Chapter 6: Improved Differential Ion Mobility Spectrometry Separations using Solvent Vapors.....	32
2.5 Data analysis .....	33
CHAPTER 3: EFFECTS OF DESOLVATION GAS FLOW RATE AND TEMPERATURE ON DIMS SEPARATIONS .....	36
3.1 Solvent Vapors and Desolvation Gas.....	36
3.2 Comparison of ESI and nESI .....	37
3.3 Comparison of ESI and Low Temperature Plasma Ionization.....	38
3.3.1. Dinitrotoluene and Caffeine.....	38
3.3.2. o-Phthalic Acid .....	43
3.4 Effects of Desolvation Gas Flow and Temperature Setting: ESI vs. LTPI.....	50
3.5 Summary and Conclusions.....	55
Chapter 4: Characterization of Variables Affecting Internal Energy Deposition inside a Differential Ion Mobility Spectrometer .....	60
4.1 Internal Energy Deposition during Ion Mobility Spectrometry .....	60

4.2	Intra-DIMS Fragmentation of Peptides.....	63
4.2.1.	Effect of Temperature on Fragmentation.....	69
4.2.2.	Effect of Carrier Gas Composition on Fragmentation.....	73
4.3.	Conclusions .....	81
CHAPTER 5: IMPROVED DIFFERENTIAL ION MOBILITY SPECTROMETRY SEPARATIONS USING LINKED SCANS OF CARRIER GAS COMPOSITION AND COMPENSATION FIELD.....		86
5.1	Using Helium as a DIMS Carrier Gas.....	86
5.2	Introduction to Linked Scans .....	87
5.3	40 to 0% Linked Scans vs. Compensation Field Scans with Constant Helium .....	89
5.4	Linked Scans vs. Compensation Field Scans with Constant Helium: Peak at Same Helium Percentage in both.....	90
8.8	Issues with Experimental Design to this Point.....	91
5.6	Slope Experiment: One $E_C$ , One Helium % .....	94
5.7	Maximizing Resolving Power.....	96
5.7.1.	Agilent ESI Tuning Mix .....	96
5.7.2.	Syntide 2 .....	97
5.8	Switching Characterization Figures of Merit.....	100
5.8.1.	Ubiquitin .....	100



5.8.2.	Trypsin Digest of BSA.....	103
5.9	Summary and Conclusions .....	109
CHAPTER 6: IMPROVED DIFFERENTIAL ION MOBILITY SPECTROMETRY SEPARATIONS USING SOLVENT VAPORS .....		114
6.1	Benefits of adding Solvent Vapors to DIMS Carrier Gas.....	114
6.2	DIMS Separation of Glucose and Glucose Isomers.....	115
6.3	DIMS Separation of Phosphorylated Sugar Isomers.....	123
6.4	Summary and Conclusions.....	133
CHAPTER 7: SUMARY AND FUTURE DIRECTIONS .....		138
7.1	General Summary.....	138
7.2	Effects of Desolvation Gas Flow Rate and Temperature on Differential Ion Mobility Spectrometry Separations .....	138
7.2.1.	Summary .....	138
7.2.2.	Future Directions .....	139
7.3	Characterization of Variables Affecting Internal Energy Deposition Inside a Differential Ion Mobility Spectrometer.....	140
7.3.1.	Summary .....	140
7.3.2.	Future Directions .....	142

7.4	Improved Differential Ion Mobility Separations using Linked scans of Carrier Gas and Compensation Field .....	143
7.4.1.	Summary .....	143
7.4.2.	Future Directions .....	144
7.5	Separations of Sugar Isomers using Differential Ion Mobility Spectrometry with Solvent Dopants .....	144
7.5.1.	Summary .....	144
7.5.1.	Future Directions .....	145

## LIST OF TABLES

2.1	Temperature measured at the entrance to the DIMS device.....	30
5.1	Peak statistics measured during DIMS scans with constant helium or linked scans.....	106
6.1	Resolution between sugar isomer peaks during DIMS scans at different $E_D$ and solvent vapor conditions.....	116

## LIST OF FIGURES

1.1	Schematic of a DT-IMS instrument.....	2
1.2	Depiction of the three types of ion mobility dependence on electric field .....	3
1.3	Illustration of three ions being separated by a DIMS device.....	5
1.4	(a) Trace of total ion current as $E_C$ is scanned with $E_D = 29.2$ kV/cm for a bradykinin sample. (b) Mass spectrum of the bradykinin sample with DIMS inactive. Mass spectrum averaged over the $E_C$ ranges (c) 100-175 V/cm, (d) 200-225 V/cm, and (e) 310-340 V/cm with $E_D = 29.2$ kV/cm using a bradykinin sample.....	7
1.5	Traces of signal intensity for $m/z$ 259 during $E_C$ scans for a sample containing two isomers at (a) $E_D = 16.7$ kV/cm, (b) $E_D = 25.0$ kV/cm (c) $E_D = 33.3$ kV/cm.....	8
1.6	Schematic of the cluster-decluster process .....	10
1.7	Plot showing the effect of helium on differential mobility of ions.....	12
2.1	Depiction of the LTPI source used .....	23
2.2	Schematics of the two DIMS devices used.....	25
2.3	Simplified representation of generating an asymmetric waveform .....	30
2.4	Depiction of the system used to add solvent vapors to the DIMS carrier gas .....	32
3.1	Plots of the characteristic $E_C$ of (a) leucine enkephalin, (b)angiotensin $1^{2+}$ , and (c) caffeine as a function of desolvation gas temperature setting and $E_D$ .....	42
3.2	Plot showing the characteristic $E_C$ for caffeine when no solvent vapor is added to the carrier gas and when 0.33% methanol (v/v) is added.....	44
3.3	Plots of the characteristic $E_C$ for caffeine and DNT ions formed by ESI and LTPI .....	45
3.4	Initial plot of the characteristic $E_C$ for o-phthalic acid ions formed by ESI and LTPI.....	43
3.5	Mass spectrum generated by CID MS/MS of ions of $m/z$ 541 during the analysis of o-phthalic acid.....	44

3.6	Basic schematic of the Bruker HCTultra including the DIMS device.....	45
3.7	DIMS scan of o-phthalic acid using ESI as the ionization technique.....	50
3.8	DIMS scans of (a) o-phthalic acid fit with two Gaussian peaks using Origin 6.0 and (b) o-phthalic acid using LTPI and ESI as the ionization techniques where the sample ionized by ESI included 15-crown-5 ether .....	51
3.9	Pictures of the ion source setup combining LTPI ionization with the introduction of solvent to the space directly in front of the DIMS device .....	52
3.10	Plot of the characteristic $E_C$ for o-phthalic acid ions formed by LTPI and LTPI in the presence of 50/50 (v/v) methanol/water.....	53
3.11	Plot of the characteristic $E_C$ of DNT ions formed by ESI and LTPI at desolvation gas temperature settings of 100 and 200 °C .....	51
3.12	Plots of the FWHM of peaks in DIMS scans formed by tracing $m/z$ 181. Ions are formed by ESI in (a) and LTPI in (b) .....	51
3.13	Plot of the characteristic $E_C$ of DNT ions formed by ESI and LTPI at desolvation gas flows of 1.0 and 3.0 L/minute .....	53
4.1	Portrayal of intra-DIMS fragmentation and the $E_C$ required to pass the ions through the DIMS device .....	61
4.2	Plot of signal intensity versus the $E_D$ applied for bradykinin $[M+3H]^{3+}$ and $[M+2H]^{2+}$ ions, and a bradykinin fragment ion .....	63
4.3	$E_C$ scans of the $[M+3H]^{3+}$ ion of bradykinin and the $[M+3H-18]^{3+}$ ion formed via fragmentation with (a) $E_D = 20.8$ kV/cm and (b) $E_D = 33.3$ kV/cm.....	64
4.4	CID MS/MS spectrum of bradykinin $[M+3H]^{3+}$ ions.....	70
4.5	Compensation field scan performed at $E_D = 33.3$ kV/cm (a) and a plot of signal intensity versus the dispersion field applied (b).....	71
4.6	CID MS/MS spectrum of (a) GLISH $[M+H]^+$ ions and (b) GLISH $[M+2H]^{2+}$ ions .....	72
4.7	Compensation field scan of GLISH ions with $E_D = 33.3$ kV/cm.....	73

4.8	(a) Plot of how carrier gas temperature affects the $E_D$ at which the $[M+3H]^{3+}$ ions of bradykinin fragment (b) Plot of the $E_D$ where a 50% fragmentation efficiency for the bradykinin $[M+3H]^{3+}$ ions is reached versus the initial internal energy of the bradykinin $[M+3H]^{3+}$ ions .....	75
4.9	(a) Plot of how carrier gas temperature affects the $E_D$ at which the $[M+2H]^{2+}$ ions of GLISH fragment (b) Plot of the $E_D$ where a 50% fragmentation efficiency for the GLISH $[M+2H]^{2+}$ ions is reached versus the initial internal energy of the GLISH $[M+2H]^{2+}$ ions .....	71
4.10	(a) Plot showing the effect of carrier gas temperature on the relationship between $E_D$ and the characteristic $E_C$ of the $[M+3H-18]^{3+}$ fragment ion of bradykinin (b) Plot showing the effect of carrier gas temperature on the peak width of the $[M+3H-18]^{3+}$ fragment ion of bradykinin .....	73
4.11	Plot of fragmentation efficiency versus $E_D$ applied with (a) 100% Nitrogen, (b) 20% Helium, (c) 20% Argon, (d) 40% Argon, (e) 20% Carbon Monoxide, (f) 40% Carbon Monoxide, and (g) 60% Carbon Monoxide carrier gas compositions .....	80
4.12	Plot of the slope of the sigmoidal curves fit to the data in Figure 4.11 versus the $E_D$ applied .....	81
4.13	Plot of the $E_D$ where a 50% fragmentation efficiency for the bradykinin $[M+3H]^{3+}$ ions is reached versus the percentage of the carrier gas that is carbon monoxide .....	83
4.14	(a) Plot showing the effect of carrier gas composition on the relationship between $E_D$ and the characteristic $E_C$ of bradykinin $[M+3H]^{3+}$ ions (b) Plot showing the effect of carrier gas composition on the peak width of bradykinin $[M+3H]^{3+}$ ions .....	84
5.1	A representative linked scan during which $m/z$ 622, 922, 1522, and 2122 from Agilent ESI tuning mix are separated .....	93
5.2	Plot showing the effect helium addition to the DIMS carrier gas has on the characteristic $E_C$ of ions and signal intensity .....	94
5.3	Plots comparing the resolving powers for three charge states of ubiquitin during compensation field scans with constant helium and linked scans .....	90

5.4	Plots comparing the resolving power of linked scans to compensation field scans with constant helium. The scans with constant helium were taken with approximately the same helium content that was present when the peaks passed through DIMS in the linked scan .....	917
5.5	Plots showing how the scanned compensation field range was changed between (a) 40-0% and (b) 60-0% helium linked scans.....	92
5.6	Plots comparing linked scans using different helium ranges where (a) the centroid of a peak is not kept constant in either the helium or compensation field domain and (b) the centroid of a peak is kept constant in both domains .....	100
5.7	Plots of resolving power for $m/z$ 922 versus the rate at which helium percentage is lowered with respect to compensation field at dispersion fields of 24.0 kV/cm and 32.0 kV/cm .....	101
5.8	Plot showing the effect on resolving power of increasing the rate at which helium content is lowered relative to compensation field for two ions formed from Agilent ESI tuning mix .....	102
5.9	Plot of resolution versus the rate at which helium content is lowered relative to compensation field.....	103
5.10	Plot showing the effect on resolving power of increasing the rate at which helium content is lowered relative to compensation field for syntide $2^{3+}$ .....	104
5.11	Comparison of resolution between the $8^{+}$ and $9^{+}$ charge states of ubiquitin using compensation field scans with constant helium and linked scans .....	106
5.12	Signal intensity for the $7^{+}$ , $8^{+}$ , and $9^{+}$ charge states of ubiquitin as a function of helium present in the DIMS carrier gas .....	107
5.13	Comparison of the peak capacities obtained during analyses of BSA using compensation field scans with constant helium and linked scans.....	104
5.14	Signal intensity for the TIC of bovine serum albumin as a function of helium content in the carrier gas for compensation field scans with constant helium (a) and linked scans (b) .....	107
6.1	DIMS spectra taken at the settings that gave the best resolution between each combination of glucose isomers studied .....	116

6.2	DIMS scans showing the effects changing $E_D$ and solvent vapor composition can have on DIMS scans of D-galactose and D-fructose.....	119
6.3	DIMS scans of D-glucose and D-sorbitol with $E_D = 33.3\text{kV/cm}$ and 0.17% (v/v) isopropyl alcohol present in the DIMS carrier gas .....	121
6.4	(a) Plot showing the effect of $E_D$ on resolution between glucose-1 phosphate and glucose-6-phosphate peaks during DIMS scans. DIMS scan at $E_D = 29.2\text{ kV/cm}$ of glucose-1-phosphate and glucose-6-phosphate with (b) no dopant present in the DIMS carrier gas, (c) 0.17% (v/v) isopropyl alcohol present in the DIMS carrier gas, and (d) 0.25% (v/v) acetonitrile present in the DIMS carrier gas.....	124
6.5	DIMS scans of glucose-1-phosphate, glucose-6-phosphate, and fructose-6-phosphate standards. Also shown is a DIMS scan of a mixture of the three isomers .....	125
6.6	(a) MS/MS spectra of ions of $m/z$ 259 from mouse liver extract (b) MS/MS spectra of glucose 1-phosphate, (c) MS/MS spectra of glucose-6-phosphate, and (c) MS/MS spectra of fructose-6-phosphate .....	127
6.7	Three DIMS scans taken with $E_D = 29.2\text{ kV/cm}$ and 0.25% (v/v) acetonitrile added to the DIMS carrier gas .....	127
6.8	(a) DIMS scan taken with $E_D = 29.2\text{ kV/cm}$ , 0.25% (v/v) acetonitrile added to the DIMS carrier gas, and 100 mass spectra averaged each $E_C$ (b) DIMS scan from (a) fit with two Gaussian peaks using Origin 6.0 .....	127
6.9	DIMS scans of glucose-1-phosphate, glucose-6-phosphate, and fructose-6-phosphate standards overlaid with the DIMS scan of mouse liver extract .....	129
6.10	MS/MS spectra of $m/z$ 259 taken with (a) $E_C = -34\text{ V/cm}$ and (b) $E_C = 3\text{ V/cm}$ during the analysis of mouse liver extract .....	129



## LIST OF ABBREVIATIONS AND SYMBOLS

BSA	bovine serum albumin
CID	collision-induced dissociation
cm	centimeter
°C	degrees Celsius
dc	direct current
$d_h$	displacement of ion during high field portion of waveform
DIMS	differential ion mobility spectrometry
$d_l$	displacement of ion during low field portion of waveform
DNT	dinitrotoluene
$\Delta T$	change in temperature
DT-IMS	drift-tube ion mobility spectrometry
E	electric field
e	fundamental charge constant ( $1.602 \times 10^{-19}$ coulombs/mole)
$E_C$	compensation field (compensation voltage divided by gap between electrodes)
$E_{C,high}$	highest characteristic compensation field of a peak detected in a DIMS scan
$E_{C,low}$	lowest characteristic compensation field of a peak detected in a DIMS scan
$E_D$	dispersion field (dispersion voltage divided by gap between electrodes)
EESI	extractive electrospray ionization
$E_l$	low electric field ( $< \sim 10^4$ V/cm)
$E_h$	high electric field ( $> \sim 10^4$ V/cm)
ESI	electrospray ionization

eV	electronvolt
F	phenylalanine
FWHM	full-width at half-max of a Gaussian peak
G	glycine
g	gram
$g$	gravitational constant
GC	gas chromatography
H	histidine
HCT	high capacity trap
He	helium
HPLC	high-performance liquid chromatography
Hz	Hertz
I	isoleucine
i.d.	inner diameter
IMS	ion mobility spectrometry
K	ion mobility ( $\text{cm}^2\text{V}^{-1}\text{s}^{-1}$ )
$k_B$	Boltzmann's constant ( $1.38 \times 10^{-23} \text{ J/K}$ )
$K_h$	high field mobility
$K_l$	low field mobility
kV	kilovolt
L	liter
L	leucine
LC	liquid chromatography

LTPI	low-temperature plasma ionization
M	molar
$M$	mass of the carrier gas
$m$	mass of the ion
$\mu$	reduced mass $\left(\frac{m_1 m_2}{m_1 + m_2}\right)$
mg	milligram
MHz	Megahertz ( $10^6$ Hertz)
mL	milliliter
$\mu\text{L}$	microliter
$\mu\text{m}$	micrometer
$\mu\text{M}$	micromolar
mm	millimeter
MS	mass spectrometry
ms	millisecond
MS/MS	tandem mass spectrometry
$m/z$	mass-to-charge ratio
$[\text{M}+\text{H}]^+$	protonated molecule
$[\text{M}+\text{Na}]^+$	sodiated molecule
N	number density of gas molecules
$\text{N}_2$	nitrogen
nESI	nano-electrospray ionization
nL	nanoliter
$\pi$	pi

q	ion charge
P	proline
PSIG	Pounds per square inch gauge
R	arginine
rf	radio frequency
S	serine
sin	sine
T	temperature
T	threonine
t	time
t <sub>h</sub>	time of high-field portion of waveform
TIC	total ion current
TIMS	trapped ion mobility spectrometry
t <sub>i</sub>	time of low-field portion of waveform
TWIMS	travelling-wave ion mobility spectrometry
U	total internal energy of an ion
U <sub>R</sub>	internal energy supplied by rotational motion
U <sub>T</sub>	internal energy supplied by translational motion
U <sub>V</sub>	internal energy supplied by vibrational motion
V	volt
v	volume
W	peak width
Y	tyrosine

$z$	ion charge state
$\Omega$	collision cross-section
$\omega$	radial frequency ( $2\pi f$ )

## CHAPTER 1: INTRODUCTION TO DIFFERENTIAL ION MOBILITY SPECTROMETRY

### 1.1. Introduction to Separations Prior to Mass Analysis

The high sensitivity and rapid analysis times of mass spectrometry have led to its importance as an analytical technique; however, low signal-to-background ratios and isomeric/isobaric interferences can be problematic during the analysis of complex mixtures. Separation techniques such as chromatography and electrophoresis are often coupled to mass spectrometry prior to ionization to reduce the complexity of the subsequent mass analysis but these separations can be time consuming [1]. Post-ionization separation techniques such as ion mobility spectrometry (IMS) are much more rapid and can also be used prior to mass analysis, either as a stand-alone separation method or as a complementary separation step after a liquid phase separation [2-5]. A commonly used ion mobility technique, drift tube ion mobility spectrometry (DT-IMS), is depicted in Figure 1.1 and uses an electric field to force ions the length of a drift tube filled with a buffer gas [5]. The ion mobility ( $K$ ) through the buffer gas depends directly upon the collisional cross-section of the ion and buffer gas by the Mason-Schamp equation:

$$K = \frac{3}{16} \left( \frac{2\pi}{\mu k_B T} \right)^{1/2} \frac{q}{N\Omega} \quad (1.1)$$

where  $k_B$  is the Boltzmann constant,  $\mu$  is the reduced mass of the ion and buffer gas,  $q$  is the ion charge,  $N$  is the number density of the buffer gas, and  $\Omega$  is the collisional cross-section of the ion in the buffer gas [6]. At the low electric field strengths used in DT-IMS (typically less than

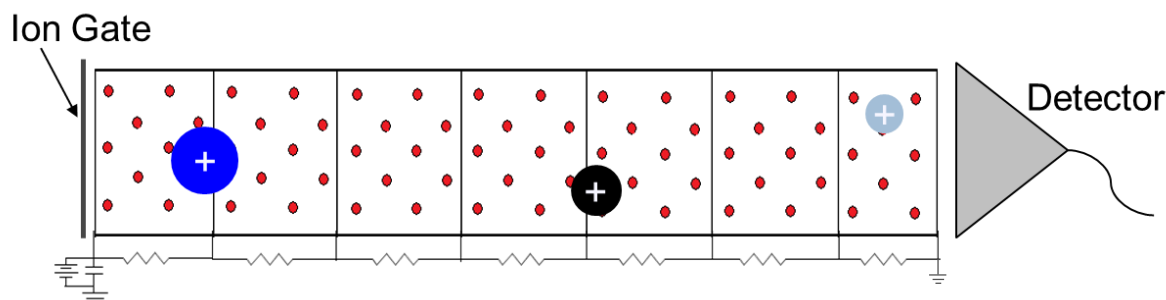


**Figure 1.1. Schematic of a DT-IMS instruments. A voltage gradient is created using successive ring electrodes separated by resistors. Ions with small cross-section in the buffer gas (red circles) traverse the drift tube and reach the detector in less time**

350 V/cm) an ion's mobility is independent of electric field strength ( $E$ ) [7]. Related ion mobility techniques, travelling wave ion mobility spectrometry (TWIMS) and trapped ion mobility spectrometry (TIMS), have been used more in recent years and also operate in the low electric field strength regime [8-11]. Although the instrumentation in these techniques is quite different from DT-IMS, in TWIMS and TIMS ion mobility is still independent of the electric field strength [12,13]. One key benefit to these low field techniques is that they allow for the determination of the collisional cross-section of the ion, which can be used to differentiate between species indistinguishable by mass spectrometry.

## 1.2. Introduction to Differential Ion Mobility Spectrometry

The low field mobility separation techniques described above function at electric field strengths at which ion mobility is independent of field strength. However, as  $E$  is increased ion mobility becomes dependent on  $E/N$  in a complex function (where  $N$  is the number density of the gas) that is characteristic of the ion [6,14-16]. The value at which this dependence begins is not well defined but is typically considered to be approximately 10.0 kV/cm [17]. Once the electric field strength is increased above this value there exist three ways ion mobility can change as a function of electric field strength, with the magnitude of the mobility shift being compound specific. The red trace in Figure 1.2 represents how the ion mobility changes for many ions, with

those ions have a mobility that decreases as electric field strength increases. Alternatively, the ion mobility can increase with increasing electric field strength as represented by the black trace in Figure 1.2. Ions with mobility that follows the third type of electric field strength dependence are represented by the blue trace, and have a mobility that increases and then decreases as the electric field strength is raised. Differential ion mobility spectrometry (DIMS) takes advantage of ion mobility depending on  $E/N$  and separates ions based on the difference between ion mobility in high and low electric fields. Thus, one advantage of DIMS is that it has the ability to separate ions with equal low field mobilities (that would not be separable using low field techniques) but have mobilities that depend on electric field strength in unlike ways or to different extents.

Differential ion mobility spectrometers consist of two parallel electrodes separated by a gap. These electrodes can be planar, as used throughout this work, or consist of two concentric cylinders. A simplified depiction of the DIMS devices used in this work is shown in Figure 1.3 with the DIMS electrodes shown in gray and three ions with various differential mobilities represented by red, purple, and green circles. When interfaced to a mass spectrometer in the way

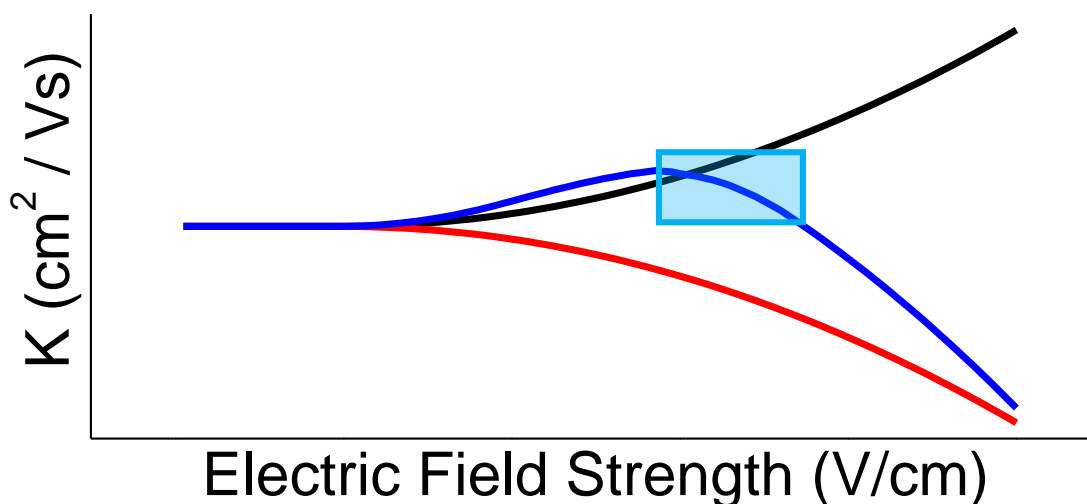


**Figure 1.2.** Depiction of the three types of ion mobility dependence on electric field. The light blue box highlights the  $E_D$  range over which ion mobilities depicted by the blue trace are greater at high electric field strengths than at low electric field strengths, but also decreasing as electric field strength is increased



done throughout this work the gas flow into the mass spectrometer (shown by the red arrow in Figure 1.3) draws ions and gases present at the entrance to the DIMS device through the electrode gap. An asymmetric rf waveform that alternates between low and high voltages of opposite polarity is applied to the electrodes. Thus, the electric field strength between the electrodes alternates in time between low ( $E_l$ ) and high ( $E_h$ ) electric fields strengths of opposite polarity. The motions of the ions in the direction of the electrodes during each portion of the waveform are represented by the line of the corresponding color. During the time spent in the low field strength portion of the waveform ( $t_l$ ), ions are displaced toward one electrode some distance ( $d_l$ ) proportional to the low field mobility ( $K_l$ ) (Equation 2). Then, during the time spent in the high field strength portion of the waveform ( $t_h$ ), ions are displaced toward the opposite electrode a distance ( $d_h$ ) proportional to the high field mobility ( $K_h$ ) (Equation 3) [16].

$$d_l = K_l E_l t_l \quad (1.2)$$

$$d_h = K_h E_h t_h \quad (1.3)$$

Design of the waveform such that  $E_l t_l = E_h t_h$  yields the net ion displacement for each period of the waveform to be proportional to the difference between the high and low field mobilities ( $K_h - K_l$ ). This net displacement is integrated across the transit time through the DIMS device, and ions are separated in space by the difference in their net displacement towards one of the electrodes. The amplitude of the high electric field strength portion of the waveform from zero to peak is commonly referred to as the dispersion voltage, or expressed as a dispersion field ( $E_D$ ), and is the equivalent of  $E_h$  in the above equations. For a waveform with  $E_l t_l = E_h t_h$ , an ion that has equal  $K_l$  and  $K_h$  would have no net displacement and pass through the DIMS device into the mass spectrometer. The net displacement of ions with  $K_h \neq K_l$  can be offset through the application of a dc compensation voltage to one of the electrodes. Also expressed as the

compensation field ( $E_C$ ), an appropriate compensation voltage counterbalances the net displacement of ions towards an electrode, thus passing ions with a selected  $K_h - K_l$  to the mass spectrometer. In Figure 1.3, an  $E_C$  is applied such that the trajectory of the purple ion is stable and it passes through the DIMS device and into the mass spectrometer. Ions with a different  $K_h - K_l$  will strike the electrodes and be neutralized, as occurs to the red and green ions in Figure 1.3. The compensation field can be held constant, such that DIMS acts as a filter for an analyte of choice, or scanned to sequentially pass ions with various differential ion mobilities [18]. The ability of DIMS to act as a filter for ions of interest is another benefit over low field techniques, as it can allow for continuous analysis of the analyte of interest whereas low field techniques cannot [6,18,19].

An example of a DIMS separation is shown in Figure 1.4 using the peptide bradykinin (RPPGFSFPR). The total ion current as the  $E_C$  is scanned at an  $E_D = 29.2$  kV/cm is shown in Figure 1.4a. The three peaks present in the scan make it apparent that ion populations with at least three distinct differential mobilities pass through DIMS at different  $E_C$ . The mass spectrum

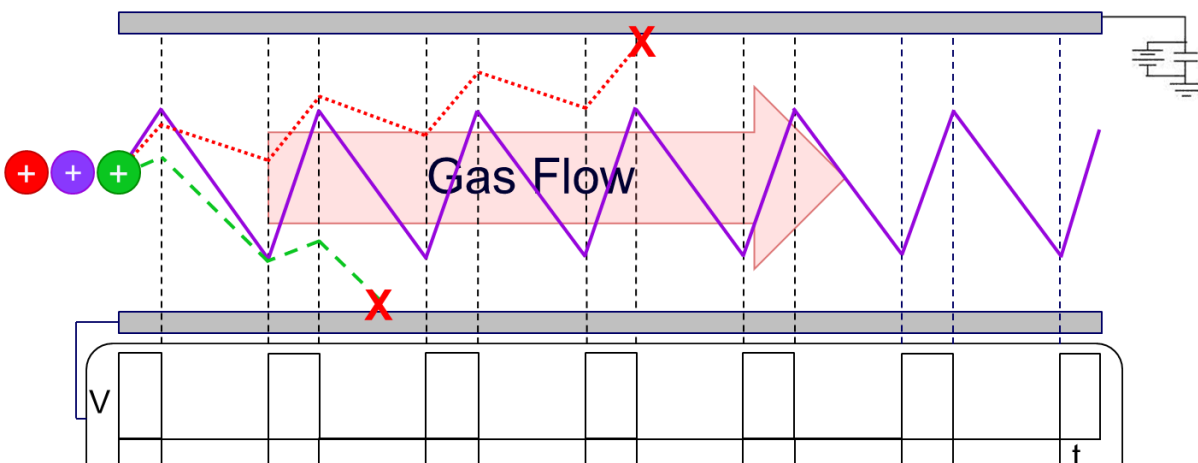


**Figure 1.3. Illustration of three ions being separated by a DIMS device with an  $E_C$  applied that corrects for the trajectory of the ion represented by the purple circle. The movements of the ions represented by the red, purple, and green circles are depicted by the dotted, dashed, and solid lines, respectively, of the corresponding color**

collected when DIMS is inactive ( $E_D = 0$  kV/cm,  $E_C = 0$  V/cm) is shown in Figure 1.4b. This spectrum is dominated by a peak at  $m/z$  354 but also has a prominent peak at  $m/z$  531. Those two peaks correspond to the  $[M+3H]^{3+}$  and  $[M+2H]^{2+}$  ions of bradykinin. This mass spectrum can be compared to the mass spectra averaged over the  $E_C$  ranges highlighted in color in Figure 1.4a. Over the  $E_C$  range highlighted in red, for which the mass spectrum is shown in Figure 1.4c, both the  $[M+H]^{3+}$  and  $[M+H]^{2+}$  ions of bradykinin are neutralized by collisions with the DIMS electrodes prior to entering the mass spectrometer. This causes the ion population detected to no longer consist mainly of bradykinin ions, and lower abundance species account for the ion current detected. Although the intensity of the three peaks in Figure 1.4a are relatively similar, the signal intensity scale Figure 1.4c is significantly lower because the current detected is spread across numerous mass-to-charge ratios and no single peak dominates the spectrum. Alternatively, the  $[M+H]^{3+}$  and  $[M+H]^{2+}$  ions of bradykinin can each be selected for based on their differential mobility as shown in Figures 1.4d and 1.4e, respectively. Although the mass spectrometer could be used to distinguish between many of the ions present in this example based on mass-to-charge, the use of DIMS can aid in the detection of low intensity ions at the same mass-to-charge ratios as the more abundant ions. Using DIMS can also allow for selective accumulation of the ion of interest when using trapping mass spectrometers.

### 1.3. Methods to Improve DIMS Separations

Improvement of DIMS separation characteristics has been a major focus of DIMS research and a few approaches have been most commonly used. The most common of these methods is to increase  $E/N$ , typically through increasing the applied  $E_D$ , although an equivalent method would be to raise the carrier gas temperature which would lower  $N$  [20-26]. The electric field strength dependence of the ion mobility changes as a function of the molecular structure

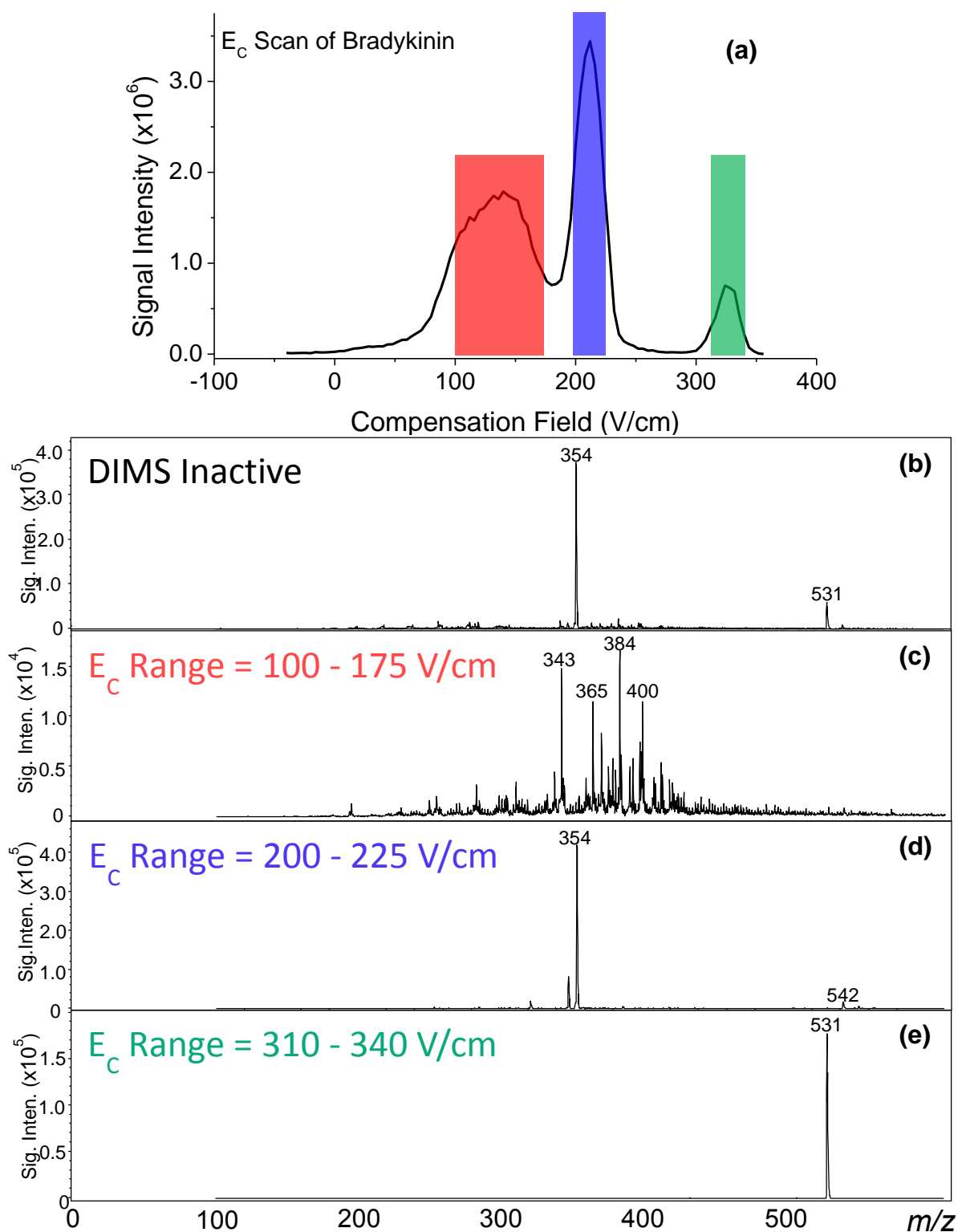


**Figure 1.4.** (a) Trace of total ion current as  $E_c$  is scanned with  $E_D = 29.2$  kV/cm for a bradykinin sample. (b) Mass spectrum of the bradykinin sample with DIMS inactive. Mass spectrum averaged over the  $E_c$  ranges (c) 100-175 V/cm, (d) 200-225 V/cm, and (e) 310-340 V/cm with  $E_D = 29.2$  kV/cm using a bradykinin sample

and increasing  $E_D$  generally improves the opportunity for differences in those dependencies to be detected.

Furthermore, most systems are set up to apply a range of  $E_D$  and thus no alteration of the system need occur to examine the separation as a function of  $E_D$  [20,22,23,27-29]. An example of the improvements that can be made by increasing  $E_D$  is shown in Figure 1.5, where the DIMS separation of two sugar isomers detected at  $m/z$  259 is shown. At the lowest  $E_D$  (Figure 1.5a) little to no separation occurs, but at  $E_D$  of 25.0 kV/cm and 33.3 kV/cm (Figure 1.5b and Figure 1.5c, respectively) the separation between the two ion populations is improved. However, there are limits to the  $E_D$  that can be applied. One issue is the maximum voltage that can be applied before the arcing across the DIMS gap occurs. This breakdown voltage is determined by the product of the distance and pressure between the two surfaces, along with composition of the gas [30]. This potential for

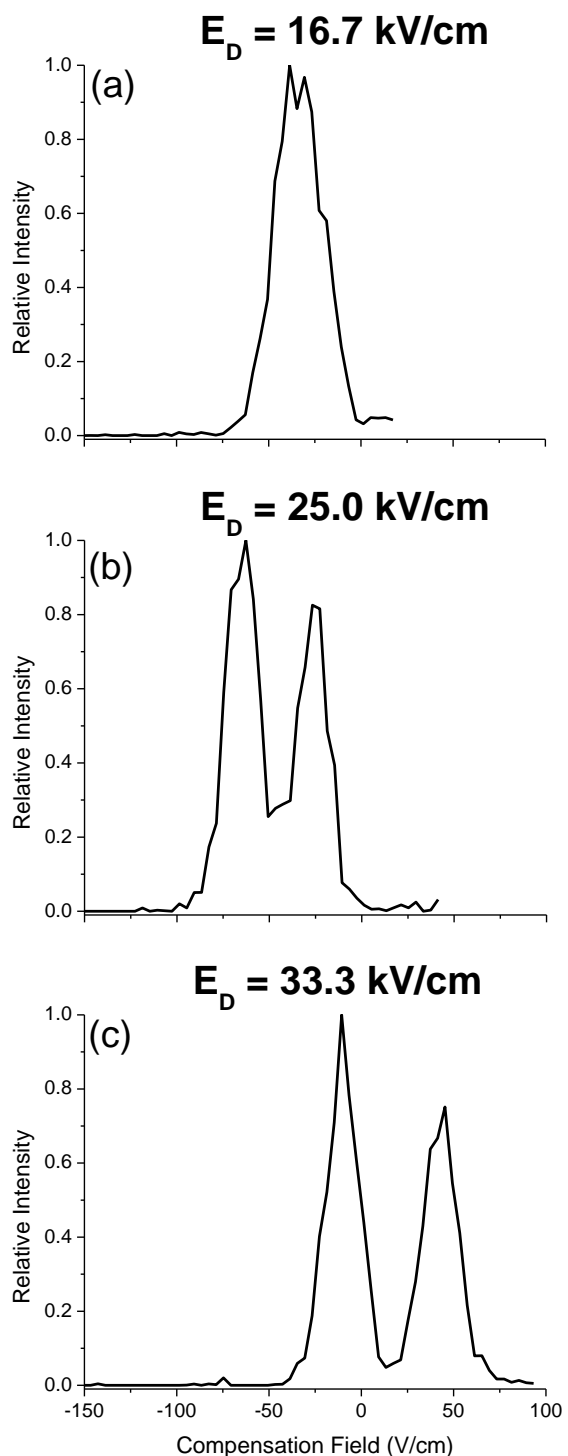


**Figure 1.5. Traces of signal intensity for  $m/z$  259 during  $E_C$  scans for a sample containing two isomers at (a)  $E_D = 16.7 \text{ kV/cm}$ , (b)  $E_D = 25.0 \text{ kV/cm}$  (c)  $E_D = 33.3 \text{ kV/cm}$**

arcing puts an upper limit on the electric field strength that can be applied.

The  $E_D$  might also be limited because the movements of the ions in the DIMS gap orthogonal to the electrodes are influenced by  $E_D$ , the charge state of the ion, and the carrier gas composition [20,31]. The ion movement can lead to the deposition of internal energy into the ion via energetic collisions with the DIMS carrier gas, potentially causing intra-DIMS isomerization and/or fragmentation of ions [28,29,32,33]. Depending on the goals of the analysis, isomerization or fragmentation can result in a loss of the information desired from the DIMS separation.

Within the limits set forth by electrical breakdown and loss of structural stability, many compounds cannot be separated solely on how their mobilities change based on  $E_D$ . Another method used to improve the DIMS separation of ions is to add solvent vapors to the DIMS carrier gas [34-37]. These typically polar molecules travel through the DIMS device with the ions and introduce an added level of chemical specificity based on differences in how they interact with ions. How the solvent molecules affect the differential mobility of the ions has been described by the cluster-decluster theorem, which is based on the ability of solvent molecules to repeatedly and rapidly cluster to and decluster from the ions [34,37,38]. An illustration of this mechanism is shown in Figure 1.6, where an ion is represented by the purple circle and solvent molecules are shown as red circles. During the low electric field strength portion of the dispersion waveform the effective temperature of the ion is cooler, and the solvent molecules are able to cluster around the ion. Thus the ion mobility in the low electric field strength is reduced because it is moving through DIMS as a larger cluster rather than a bare ion. During the high electric field strength portion of the dispersion waveform the cluster is heated by energetic collisions and the effective temperature of the cluster is increased. This results in desolvation of

the ion and it travels based on its high field mobility. This cluster-decluster process takes place during each cycle of the waveform; however, for simplicity in Figure 1.6 both the cluster and decluster processes are only shown to occur during one third of the waveform cycles.

The extent to which the differential ion mobility is affected by the addition of solvent vapors is dependent on how many molecules cluster to the ion and how strongly they are bound to the ion. These traits are based upon characteristics such as the steric hindrance of both the ion and the solvent molecules, and the polarizability of the solvent molecules [39]. Despite the benefits, the chemical specificity that adds value to separations using solvent vapors is also a deterrent for the use of the technique. How the differential ion mobility of ions changes upon the addition of solvent vapors to the carrier gas must be determined empirically, as does the optimization of other variables affecting the cluster-decluster process such as the carrier gas temperature and the concentration of solvent molecules used [40]. This optimization only needs to occur once; however, as the optimized method can be used for all subsequent analysis.

Another method to alter the characteristic  $E_C$  of ions in a sample and improve DIMS separations is to vary the typically nitrogen DIMS carrier gas to include gases such as hydrogen

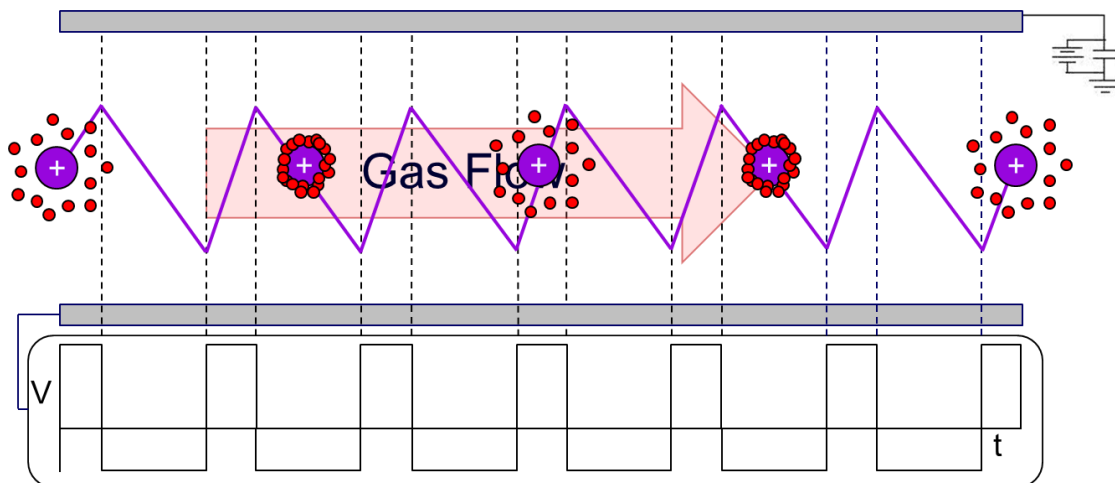


**Figure 1.6. Schematic of the cluster-decluster process that takes place when solvent vapors are added to the DIMS carrier gas**

or helium, with helium being the most commonly added alternative to nitrogen [20,23,41-43]. Using helium in the DIMS carrier gas increases the mobility of all ions, no matter how their mobility changes as a function of  $E_D$  [41]. Ions with a mobility that decreases as a function of  $E_D$ , like that depicted by the red trace in Figure 1.2, exhibit increased differential ion mobility due to the low polarizability of helium. The long-range attractive interactions that occur due to the polarizability of the carrier gas raise mobilities in high electric field strengths. Without these interactions, the decrease in mobility as a function of  $E_D$  becomes even more prominent. Ions with mobilities that only increase as a function of  $E_D$ , such as the ion with mobility shown by the black trace in Figure 1.2, also display greater differential ion mobilities when helium is used. This particular increase in differential ion mobility is believed to be due to large deviations from Blanc's law that outweigh the factors that would otherwise decrease the differential ion mobility [41]. Blanc's law attempts to predict ion mobility in gas mixtures based on the ion mobility in the individual gases and works well with gas mixtures where the gases are very similar, such as nitrogen and oxygen. However, as the characteristics of the gases become more disparate, such as those of nitrogen and helium, the relationships do not hold [6]. Therefore, the differential mobility increases when helium is added for ions with differential mobilities that only increase as a function of  $E_D$ . For ions that have a dependence on electric field strength that first increases and then decreases the change in differential ion mobility upon the addition of helium will be dependent on the electric field strength used and the amount of helium added to the carrier gas [41]. It would be expected that generally the differential ion mobility of these ions would be increased, excepting the  $E_D$  range highlighted in Figure 1.2 by the light blue box. In this  $E_D$  range the ion's high field mobility is greater than the low field mobility, but the high field



mobility will decrease as  $E_D$  increases. The addition of helium during the use of these  $E_D$  would lower the high field mobility, thus decreasing the differential ion mobility.

Despite this, for all three types of ion mobility dependence on  $E/N$ , the increases in differential ion mobility typically observed when helium is used will result in greater absolute values of required  $E_C$  to correct for ion movement towards the electrodes. However, the extent of the shift in  $E_C$  upon the addition of helium to the carrier gas is not equal for all ions. The  $E_C$  of ions with greater differential mobility in nitrogen typically shifts more upon the addition of helium to the carrier gas, resulting in improved separations [32]. This effect is shown in Figure 1.7 where the normalized signal intensity of four different ions is shown as the amount of helium present in the carrier gas is increased from 0 to 60% in 5% increments. Each ion exhibits increasing differential ion mobility as helium is added; however, the rate of change in differential mobility as helium is added is greatest for those ions with highest differential ion mobility in a nitrogen carrier gas. Although this is not universal, the general result is increased dispersion in the compensation field domain and improvement of DIMS separations [32].

#### 1.4. Quantification of DIMS Separations

The improvements in DIMS separations described above have typically been quantified in a similar manner to chromatographic and DT-IMS separations. As such resolving power,

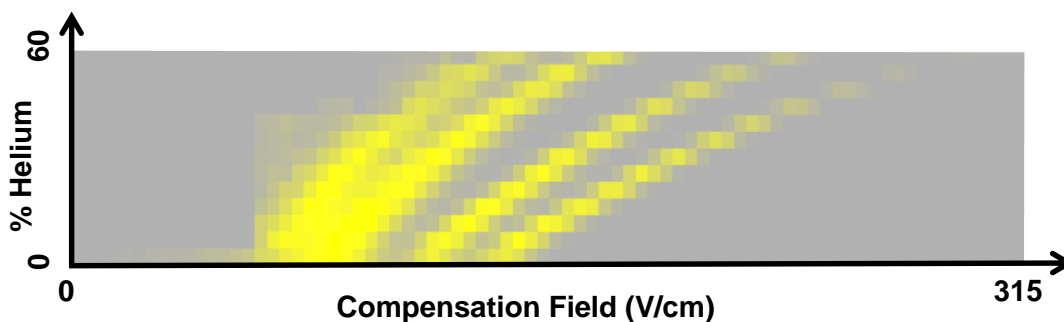


**Figure 1.7.** Plot showing the normalized signal intensity of four ions as a function of the helium content of the carrier gas and compensation field

resolution, and peak capacity are often used to describe the separations [20,23,25,37,38,42].

Resolving power is the most commonly reported value for DIMS separations due to its ease of use. The resolving power of a DIMS separation can be calculated using Equation 1.4, and depends only on the compensation field required to pass an analyte through DIMS and the width of that analyte's peak in the DIMS scan, measured as a full width at half maximum (FWHM) [38]. Therefore, calculating the resolving power of a DIMS separation requires only one analyte be used, and has previously been described as an adequate way to compare separation abilities across DIMS devices [42]. Alternatively, the resolution between two peaks requiring different compensation fields ( $E_{C1}$  and  $E_{C2}$ ) can be calculated (Equation 1.5), or the peak capacity of the entire separation can be determined using the highest ( $E_{C,high}$ ) and lowest ( $E_{C,low}$ ) required  $E_C$  in a DIMS scan, the average FWHM of all the peaks detected in the  $E_C$  scan, and Equation 3 [38]. These values are preferred over resolving power because they describe the separation that is occurring, rather than expressing the theoretical separation capabilities of a DIMS device [44].

$$\text{Resolving Power} = \frac{E_C}{(\text{FWHM})} \quad (1.4)$$

$$\text{Resolution} = \frac{E_{C1}-E_{C2}}{\left(\frac{w_1+w_2}{2}\right)} = \frac{1.178 (E_{C1}-E_{C2})}{(\text{FWHM}_1+\text{FWHM}_2)} \quad (1.5)$$

$$\text{Peak Capacity} = \frac{(E_{C,high}-E_{C,low})}{(\text{Average FWHM})} \quad (1.6)$$

## 1.5. Summary

The purpose of this chapter has been to give an introduction to differential ion mobility spectrometry separations that allows the reader to understand the experiments and insights described throughout the remainder of the work. Much of the work presented herein depends on an understanding of the ion motion within a DIMS device or an understanding of the current

methods used to improve DIMS separations. As such, the presenting this information has been the focus of a majority of **Chapter 1**.

In **Chapter 2** the experimental methods used in the subsequent chapters are provided. Details about the analytes and solvents used are included. The instrumentation used is also covered, including information about the DIMS devices, mass spectrometers, and ion sources. Additionally, the methods employed for data analysis are discussed.

The work presented in **Chapter 3** involves the characterization of the mass spectrometer desolvation gas settings as they pertain to DIMS analyses. Specifically, how lowering of the desolvation gas temperature setting or flow rate affects DIMS analyses when ion sources that use solvent flows are used is described. Initially, electrospray ionization and nano-electrospray ionization sources are compared using the characteristic  $E_C$  required to pass ions formed by each through the DIMS device. The work continues on to describe the results of experiments comparing electrospray ionization and low temperature plasma ionization by examining both the characteristic  $E_C$  of ions formed and the peak FWHM during DIMS scans as a function of desolvation gas flow and temperature setting. The issues that arose during the analysis of o-phthalic acid are also discussed in the chapter.

The intra-DIMS fragmentation of the peptides bradykinin and GLISH caused by collisional heating during the ion's transit through the DIMS device is described in **Chapter 4**. The variables that affect the fragmentation are described including the charge state of the peptide, the temperature of the DIMS carrier gas, and the composition of the DIMS carrier gas. Experiments are presented comparing the internal energy deposition in DIMS to the collisional activation step done during tandem mass spectrometry experiments in an ion trap mass spectrometer. Also shown are methods for either increasing or decreasing the amount of internal

energy deposited into the ions travelling through the DIMS device. The effects on separation capability of changing these variables to adjust internal energy deposition are also discussed.

The beginning of **Chapter 5** includes a brief description of the benefits and downsides of using helium as a DIMS carrier gas. Linked scans of the DIMS carrier gas composition and the compensation field are then introduced. The optimization of the methods used to quantify the improvements observed from linked scans is discussed, including the work focused on improving the resolving power attainable with the system. Why the promising results observed using resolving power were invalid, and the transition to resolution and peak capacity is then explained. The comparison of linked scans to compensation field scans with constant helium is then presented using resolution, peak capacity, and signal intensity as the figures of merit.

DIMS separations where solvent vapors are added to the DIMS carrier gas are explained in **Chapter 6**. The optimization of solvent addition is discussed with regards to the DIMS separation of D-glucose and three of its isomers. Variables manipulated include the dispersion field applied and the solvent utilized. The appearance of multiple peaks during DIMS scans when the analysis of only one sugar isomer was anticipated is also discussed. The experiments using the solvent addition system to separate biological relevant phosphorylated sugars, both in the form of pure standards and from rat liver cell extracts, are then described. Lastly, **Chapter 7** is a summary of the results of each chapter presented and considers potential future directions related to this work.

## REFERENCES

1. Schneider, B.; Covey, T.; Nazarov, E. DMS-MS Separations with Different Transport Gas Modifiers. *Int. J. Ion Mobil. Spec.* **2013**, *16*, 207-216.
2. Kolakowski, B. M.; Mester, Z. Review of Applications of High-Field Asymmetric Waveform Ion Mobility Spectrometry (FAIMS) and Differential Mobility Spectrometry (DMS). *Analyst.* **2007**, *132*, 842-864.
3. Hatsis, P.; Kapron, J. T. A Review on the Application of High-Field Asymmetric Waveform Ion Mobility Spectrometry (FAIMS) in Drug Discovery. *Rapid Commun. Mass Spectrom.* **2008**, *22*, 735-738.
4. Xia, Y.; Wu, S. T.; Jemal, M. LC-FAIMS-MS/MS for Quantification of a Peptide in Plasma and Evaluation of FAIMS Global Selectivity from Plasma Components. *Anal. Chem.* **2008**, *80*, 7137-7143.
5. Kanu, A. B.; Dwivedi, P.; Tam, M.; Matz, L.; Hill Jr., H. H. Ion Mobility–mass Spectrometry. *J. Mass Spectrom.* **2008**, *43*, 1-22.
6. Shvartsburg, A. A. Differential Ion Mobility Spectrometry : Nonlinear Ion Transport and Fundamentals of FAIMS; CRC Press, Boca Raton, 2009.
7. Laphorn, C.; Pullen, F.; Chowdhry, B. Ion Mobility Spectrometry-Mass Spectrometry (IMS-MS) of Small Molecules: Separating and Assigning Structures to Ions. *Mass Spectrometry Reviews.* **2012**.
8. Merenbloom, S. I.; Flick, T. G.; Williams, E. R. How Hot are Your Ions in TWAVE Ion Mobility Spectrometry. *J. Am. Soc. Mass Spectrom.* **2011**, *23*, 553-562.
9. Hilton, G.; Thalassinou, K.; Grabenauer, S., N.; Slade, S.; Wytenbach, T.; Robinson, P.; Pinheiro, T.; Bowers, M.; Scrivens, J. Structural Analysis of Prion Proteins by Means of Drift Cell and Traveling Wave Ion Mobility Mass Spectrometry. *J. Am. Soc. Mass Spectrom.* **2010**, *21*, 845-854.
10. Faull, P.; Florance, H.; Schmidt, C.; Tomczyk, N.; Barlow, P.; Hupp, T.; Nikolova, P.; Barran, P. Utilising Ion Mobility-Mass Spectrometry to Interrogate Macromolecules: Factor H Complement Control Protein Modules 10–15 and 19–20 and the DNA-Binding Core Domain of Tumour Suppressor p53. *Int. J. Mass Spectrom.* **2010**, *298*, 99-110.

11. Michelmann, K.; Silveira, J.; Ridgeway, M.; Park, M. Fundamentals of Trapped Ion Mobility Spectrometry. *J. Am. Soc. Mass Spectrom.* **2015**, *26*, 14-24.
12. Fernandez-Lima, F.; Kaplan, D. A.; Suetering, J.; Park, M. A. Gas-Phase Separation using a Trapped Ion Mobility Spectrometer. *Int. J. Ion Mob. Spectrom.* **2011**, *14*, 93-98.
13. Shvartsburg, A. A.; Smith, R. D. Fundamentals of Traveling Wave Ion Mobility Spectrometry. *Anal. Chem.* **2008**, *80*, 9689-9699.
14. Eiceman, G. A.; Karpas, Z. Ion Mobility Spectrometry, Second ed.; CRC Press, 2005.
15. Mason, E. A.; McDaniel, E. W. Transport Properties of Ions in Gases; Wiley, New York, 1988.
16. Purves, R. W.; Guevremont, R.; Day, S.; Pipich, C. W.; Matyjaszczyk, M. S. Mass Spectrometric Characterization of a High-Field Asymmetric Waveform Ion Mobility Spectrometer. *Rev. Sci. Instrum.* **1998**, *69*, 4094-4105.
17. Guevremont, R.; Purves, R. W. High Field Asymmetric Waveform Ion Mobility Spectrometry-Mass Spectrometry: An Investigation of Leucine Enkephalin Ions Produced by Electrospray Ionization. *Journal of the American Society for Mass Spectrometry.* **1999**, *10*, 492-501.
18. Dharmasiri, U.; Isenberg, S. L.; Glish, G. L.; Armistead, P. M. Differential Ion Mobility Spectrometry Coupled to Tandem Mass Spectrometry Enables Targeted Leukemia Antigen Detection. *J. Proteome Res.* **2014**, *13*, 4356-4362.
19. Barnett, D. A.; Guevremont, R.; Purves, R. W. Determination of Parts-Per-Trillion Levels of Chlorate, Bromate, and Iodate by Electrospray Ionization/High-Field Asymmetric Waveform Ion Mobility Spectrometry/Mass Spectrometry. *Appl. Spectrosc.* **1999**, *53*, 1367-1374.
20. Shvartsburg, A. A.; Prior, D. C.; Tang, K.; Smith, R. D. High-Resolution Differential Ion Mobility Separations using Planar Analyzers at Elevated Dispersion Fields. *Anal. Chem.* **2010**, *82*, 7649-7655.
21. Shvartsburg, A. A.; Creese, A. J.; Smith, R. D.; Cooper, H. J. Separation of a Set of Peptide Sequence Isomers using Differential Ion Mobility Spectrometry. *Anal. Chem.* **2011**, *83*, 6918-6923.

22. Blagojevic, V.; Bohme, D. K. Differential Mobility Spectrometer as an Ion/Molecule Reactor: Peptide H–D Exchange in Mobility Separation. *Int. J. Mass Spectrom.* **2015**, 378, 180-185.
23. Isenberg, S. L.; Armistead, P. M.; Glish, G. L. Optimization of Peptide Separations by Differential Ion Mobility Spectrometry. *J. Am. Soc. Mass Spectrom.* **2014**, 25, 1592-1599.
24. Buryakov, I.; Krylov, E.; Nazarov, E.; Rasulev, U. A New Method of Separation of Multi-Atomic Ions by Mobility at Atmospheric Pressure using a High-Frequency Amplitude-Asymmetric Strong Electric Field. *International Journal of Mass Spectrometry and Ion Processes.* **1993**, 128, 143-148.
25. Shvartsburg, A. A.; Smith, R. D. Scaling of the Resolving Power and Sensitivity for Planar FAIMS and Mobility-Based Discrimination in Flow- and Field-Driven Analyzers. *J Am Soc Mass Spectrom.* **2007**, 18, 1672-1681.
26. Shvartsburg, A. A.; Smith, R. D. Ultrahigh-Resolution Differential Ion Mobility Spectrometry using Extended Separation Times. *Anal. Chem.* **2011**, 83, 23-29.
27. Shvartsburg, A. A.; Creese, A. J.; Smith, R. D.; Cooper, H. J. Separation of a Set of Peptide Sequence Isomers using Differential Ion Mobility Spectrometry. *Anal. Chem.* **2011**, 83, 6918-6923.
28. Kendler, S.; Lambertus, G. R.; Dunietz, B. D.; Coy, S. L.; Nazarov, E. G.; Miller, R. A.; Sacks, R. D. Fragmentation Pathways and Mechanisms of Aromatic Compounds in Atmospheric Pressure Studied by GC-DMS and DMS-MS. *Int. J. Mass Spectrom. Ion Proc.* **2007**, 263, 137-147.
29. An, X.; Eiceman, G. A.; Rodriguez, J. E.; Stone, J. A. Gas Phase Fragmentation of Protonated Esters in Air at Ambient Pressure through Ion Heating by Electric Field in Differential Mobility Spectrometry. *Int. J. Mass Spectrom.* **2011**, 303, 181-190.
30. Friedrich, P. Ueber Die Zum Funkenübergang in Luft, Wasserstoff Und Kohlensäure Bei Verschiedenen Drucken Erforderliche Potentialdifferenz. *Annalen Der Physik.* **1889**, 273, 69-96.
31. Shvartsburg, A. A.; Li, F.; Tang, K.; Smith, R. D. Distortion of Ion Structures by Field Asymmetric Waveform Ion Mobility Spectrometry. *Anal. Chem.* **2007**, 79, 1523-1528.

32. Shvartsburg, A. A.; Danielson, W. F.; Smith, R. D. High-Resolution Differential Ion Mobility Separations using Helium-Rich Gases. *Anal. Chem.* **2010**, 82, 2456-2462.
33. Nazarov, E. G.; Coy, S. L.; Krylov, E. V.; Miller, R. A.; Eiceman, G. A. Pressure Effects in Differential Mobility Spectrometry. *Anal. Chem.* **2006**, 78, 7697-7706.
34. Krylova, N.; Krylov, E.; Eiceman, G. A.; Stone, J. A. Effect of Moisture on the Field Dependence of Mobility for Gas-Phase Ions of Organophosphorus Compounds at Atmospheric Pressure with Field Asymmetric Ion Mobility Spectrometry. *J. Phys. Chem. A.* **2003**, 107, 3648-3654.
35. Eiceman, G. A.; Krylov, E. V.; Krylova, N. S.; Nazarov, E. G.; Miller, R. A. Separation of Ions from Explosives in Differential Mobility Spectrometry by Vapor-Modified Drift Gas. *Anal. Chem.* **2004**, 76, 4937-4944.
36. Schneider, B. B.; Nazarov, E. G.; Covey, T. R. Peak Capacity in Differential Mobility Spectrometry: Effects of Transport Gas and Gas Modifiers. *Int. J. Mass Spectrom.* **2012**, 15, 141-150.
37. Rorrer, L. C. R. L. C.; Yost, R. A. Solvent Vapor Effects on Planar High-Field Asymmetric Waveform Ion Mobility Spectrometry. *Int. J. Mass Spectrom.* **2011**, 300, 173-181.
38. Schneider, B.; Covey, T.; Coy, S.; Krylov, E.; Nazarov, E. Chemical Effects in the Separation Process of a Differential Mobility/Mass Spectrometer System . *Anal. Chem.* **2010**, 82, 1867-1880.
39. Campbell, J. L.; Zhu, M.; Hopkins, W. S. Ion-Molecule Clustering in Differential Mobility Spectrometry: Lessons Learned from Tetraalkylammonium Cations and their Isomers. *J. Am. Soc. Mass Spectrom.* **2014**, 25, 1583-1591.
40. Auerbach, D.; Aspenleiter, J.; Volmer, D. A. Description of Gas-Phase Ion/Neutral Interactions in Differential Ion Mobility Spectrometry: CV Prediction using Calibration Runs. *J. Am. Soc. Mass Spectrom.* **2014**, 25, 1610-1621.
41. Shvartsburg, A. A.; Tang, K. Q.; Smith, R. D. Understanding and Designing Field Asymmetric Waveform Ion Mobility Spectrometry Separations in Gas Mixtures. *Anal. Chem.* **2004**, 76, 7366-7374.



42. Shvartsburg, A. A.; Tang, K. Q.; Smith, R. D. Differential Ion Mobility Separations of Peptides with Resolving Power Exceeding 50. *Anal. Chem.* **2010**, 82, 32-35.
43. Shvartsburg, A.; Smith, R. Accelerated High-Resolution Differential Ion Mobility Separations using Hydrogen. *Anal. Chem.* **2011**, 83, 9159-9166.
44. Santiago, B. G.; Harris, R. A.; Isenberg, S. L.; Ridgeway, M. E.; Pilo, A. L.; Kaplan, D. A.; Glish, G. L. Improved Differential Ion Mobility Separations using Linked Scans of Carrier Gas Composition and Compensation Field. *J. Am. Soc. Mass Spectrom.* **2015**, 26, 1746-1753.

## CHAPTER 2: EXPERIMENTAL

### 2.1 Materials

Methanol (optima grade), acetonitrile (optima grade), water (HPLC grade), ammonium hydroxide (ACS plus), and acetic acid (ACS plus) were purchased from Fisher Scientific (Fairlawn, NJ, USA). A majority of the analytes used were purchased from Sigma (St. Louis, MO, USA), including caffeine (98%), angiotensin I ( $\geq 90\%$  by HPLC), 2,4-dinitrotoluene (97%), o-phthalic ( $\geq 98\%$ ), bradykinin acetate salt (98%), ubiquitin from bovine red blood cells (min. 90% by SDS Page), and syntide 2 (min. 95% by HPLC). D-glucose ( $\geq 99.5\%$ ), D-galactose ( $\geq 99\%$ ), D-fructose ( $\geq 98\%$ ), and D-mannose ( $\geq 99\%$ ) were also purchased from Sigma (St. Louis, MO, USA), as were glucose-1-phosphate ( $\geq 97\%$ ), glucose-6-phosphate ( $\geq 98\%$ ), and fructose-6-phosphate ( $\geq 98\%$ ). Tryptic digest of bovine serum albumin (BSA) was purchased from Waters (Milford, MA, USA). The peptides tyrosine-glycine-glycine-phenylalanine-leucine (YGGFL) and glycine-leucine-isoleucine-serine-histidine (GLISH) were synthesized using a CS036 peptide synthesizer from CS Bio (Menlo Park, CA) and used without purification.

Caffeine, angiotensin I, and YGGFL solutions were prepared at 5  $\mu\text{M}$  in 50/49/1 (v/v/v) methanol/water/acetic acid for experiments where the samples were mass analyzed using the Bruker Esquire 3000 ion trap mass spectrometer. Caffeine samples were further diluted to 1  $\mu\text{M}$  when mass analyzed using the HCTUltra ion trap mass spectrometer. Both 2,4-dinitrotoluene

and o-phthalic acid solutions were prepared at 100  $\mu$ M in 50/49/1 (v/v/v) methanol/water/ammonium hydroxide. Bradykinin samples were diluted to 2.5  $\mu$ M, whereas GLISH samples were diluted to approximately 1  $\mu$ M, both in 50/49/1 (v/v/v) methanol/water/acetic acid. Agilent ESI high concentration tuning mix was diluted 20 fold in 95/5 acetonitrile/water. Ubiquitin, syntide 2, and BSA samples were diluted in 50/49/1 (v/v/v) methanol/water/acetic acid to concentrations of 7.2  $\mu$ M, 6.7  $\mu$ M, and 0.50  $\mu$ M, respectively. Lastly, the sugars D-glucose, D-galactose, D-fructose, D-mannose, glucose-1-phosphate, glucose-6-phosphate, and fructose-6-phosphate solutions were all prepared at a concentration of 10  $\mu$ M in 50/50 methanol/water (v/v). Mixtures of the phosphorylated sugar compounds were prepared by mixing equal volumes of the 10  $\mu$ M solutions.

To collect mouse extracts the mouse was anesthetized with isofluran, decapitated, and the liver was removed. Immediately after removal, the liver was flash-frozen in liquid nitrogen. The time from removal to flash freezing was under 20 seconds. The liver sample was then pulverized in liquid nitrogen, weighed ( $70 \pm 3$  mg per tube), and stored at -86 °C. The liver samples were then re-suspended in 600  $\mu$ l of ice-cold acetonitrile, freeze-thawed on ice for 15 minutes, and vortexed for 30 seconds. Then 400  $\mu$ L of ice-cold deionized water was added before the suspension was vortexed and freeze-thawed two more times. Samples were then centrifuged at 4500 x g for 5 minutes, and the supernatant was collected and lyophilized. Prior to the experiment described in Chapter 6, 2 mL of 60/40 methanol/water was added to the lyophilized samples. The samples were then shaken using a Qiagen TissueLyser II in the presence of six stainless steel beads for two rounds, each 30 seconds in length. Using an Eppendorf Centrifuge 5414, the samples were centrifuged for 10 minutes and the supernatant was then diluted 2x in 50/50 methanol/water.

## 2.2 Ionization Techniques

Ions were formed during the experiments presented in this work using one of three ion sources. Ions were formed via electrospray ionization (ESI) using the Agilent ESI emitter that came standard with both the Bruker Esquire 3000 and the Bruker HCTUltra. Samples were infused at a flow rate of 2  $\mu\text{L}/\text{minute}$ , and a nebulization gas pressure of 10 PSIG was used. ESI was used as the ionization technique for a portion of Chapter 3, and the entirety of the subsequent chapters. Chapter 3 also includes experiments where ions were formed by nano-electrospray ionization (nESI). These experiments were performed using sprayers constructed using a custom-built copper block that accepted 0.060" O.D. x 0.045" I.D. glass capillaries (Drummond Scientific Company, Broomall, PA) that were pulled at one end to  $\sim 4\text{ }\mu\text{m}$  using a Narishige model PP-830 dual stage glass electrode puller (Narishige International USA, Inc., Easy Meadow, NY). Solutions were injected into the sprayer through the non-tapered end. The copper block also has a hole tapped for a metal screw that can be tightened into contact with a stainless steel wire inserted into the open end of the sprayer. In this way electrical contact with the nESI spray solution is made, and application of a sufficiently high electric field between the wire electrode and the inlet of the mass spectrometer generates spray without the need for pneumatic assistance.

The third ion source discussed and used in Chapter 3 is a custom built miniature low temperature plasma ionization (LTPI) source like that depicted in Figure 2.1. LTPI utilizes a dielectric barrier discharge to generate a reaction cascade that in this work results in the protonation or deprotonation of the analyte molecule [1,2]. The LTPI source was built around a stainless steel Upchurch female-to-female fingertight zero-dead-volume union. A glass melting point capillary (Custom Glass Tubing, Drummond Scientific Company, Broomall, PA, item

number 9-000-2313-A; i.d. 1.0 mm, o.d. 1.6 mm) was cut to a length of ~40 mm and inserted into an Upchurch PEEK fingertight HPLC fitting. The PEEK fitting was then tightened into one side of the female-to-female union, securing the glass capillary. A SW-10 stylet wire (SGE Analytical Science, Austin, TX; P/N 031745, diameter = 0.10 mm) was then inserted through the female-to-female union and into the glass capillary until it was ~8 mm from the end of the glass capillary. The wire was held in place by tightening the female-to-female union onto another Upchurch PEEK fingertight fitting. This second fingertight fitting secured the wire between the threads of the union, and was also connected to a gas line that supplied the flow of nitrogen gas used for the formation of plasma.

Copper tape (10 mm wide) was wrapped around the female-to-female union for connection of the union to a ground potential through an alligator clip. This also grounded the stylet wire because it is in direct electrical contact with the stainless steel union. Leaving ~3 mm of glass exposed, copper tape was also wrapped around the end of the glass capillary. Thus, the stylet wire traverses approximately  $\frac{1}{2}$  of the way through the portion of the glass capillary wrapped in copper tape. A high voltage sine wave was then applied to copper tape surrounding

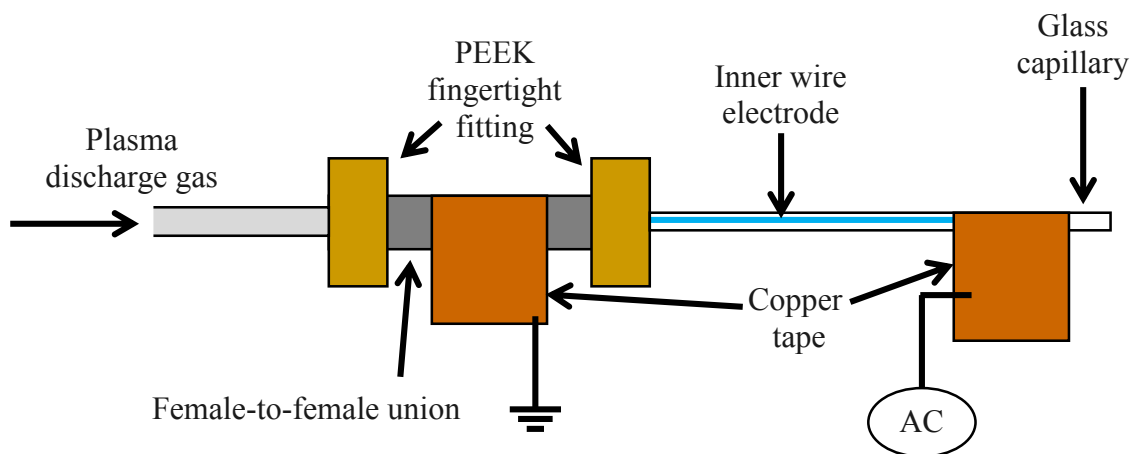


**Figure 2.1. Depiction of the LTPI source used in Chapter 3. The stainless steel female-to-female union is shown in grey, PEEK fingertight fittings are shown in brown, copper tape is shown in orange, and the inner electrode is shown in blue**

the glass capillary. The glass capillary is an insulating barrier between the inner electrode (the grounded stylet wire) and the outer electrode (the copper tape wrapped around the glass capillary) and a plasma is created within the glass capillary. In the experiments described in Chapter 3 that use LTPI, solid analyte was placed on the tip of the glass capillary prior to starting the plasma gas flow and applying voltage to the outer electrode. With this set-up, a portion of the plasma plume directly interacts with the analyte and ions are generated. A full optimization of the voltage and plasma gas flow was not completed as this work focused on the DIMS separations that occurred after ionization, and therefore settings were varied until sufficient signal intensity was obtained for the analytes being studied.

### **2.3 Differential Ion Mobility Spectrometers and Mass Spectrometers**

Two DIMS devices with planar electrodes were used during the experiments presented herein. One device was coupled to an Esquire 3000 ion trap mass spectrometer whereas the other coupled to a Bruker HCTUltra ion trap mass spectrometer to produce the data shown. The device that worked in conjunction with the Bruker Esquire 3000 is shown in Figure 2.2a and has been previously described [3-5]. The electrodes used are 25 mm long x 6 mm wide, with interchangeable electrode sets that allow for the gap between the electrodes to be switched between 0.3 and 0.5 mm. The DIMS assembly threads onto the Apollo I source of the Bruker Esquire 3000 ion trap mass spectrometer, replacing the spray shield. The DIMS device that couples to the Bruker HCTUltra is shown in Figure 2.2b and has stainless steel electrodes that are 4mm wide x 10 mm long separated by a 0.3 mm gap [6]. The assembly is designed so that it slides over the end of the instrument's resistive glass transfer capillary. Both systems are designed such that the DIMS electrodes are enclosed in a housing that reroutes the mass spectrometer desolvation gas around the electrodes. This is shown for the system depicted in

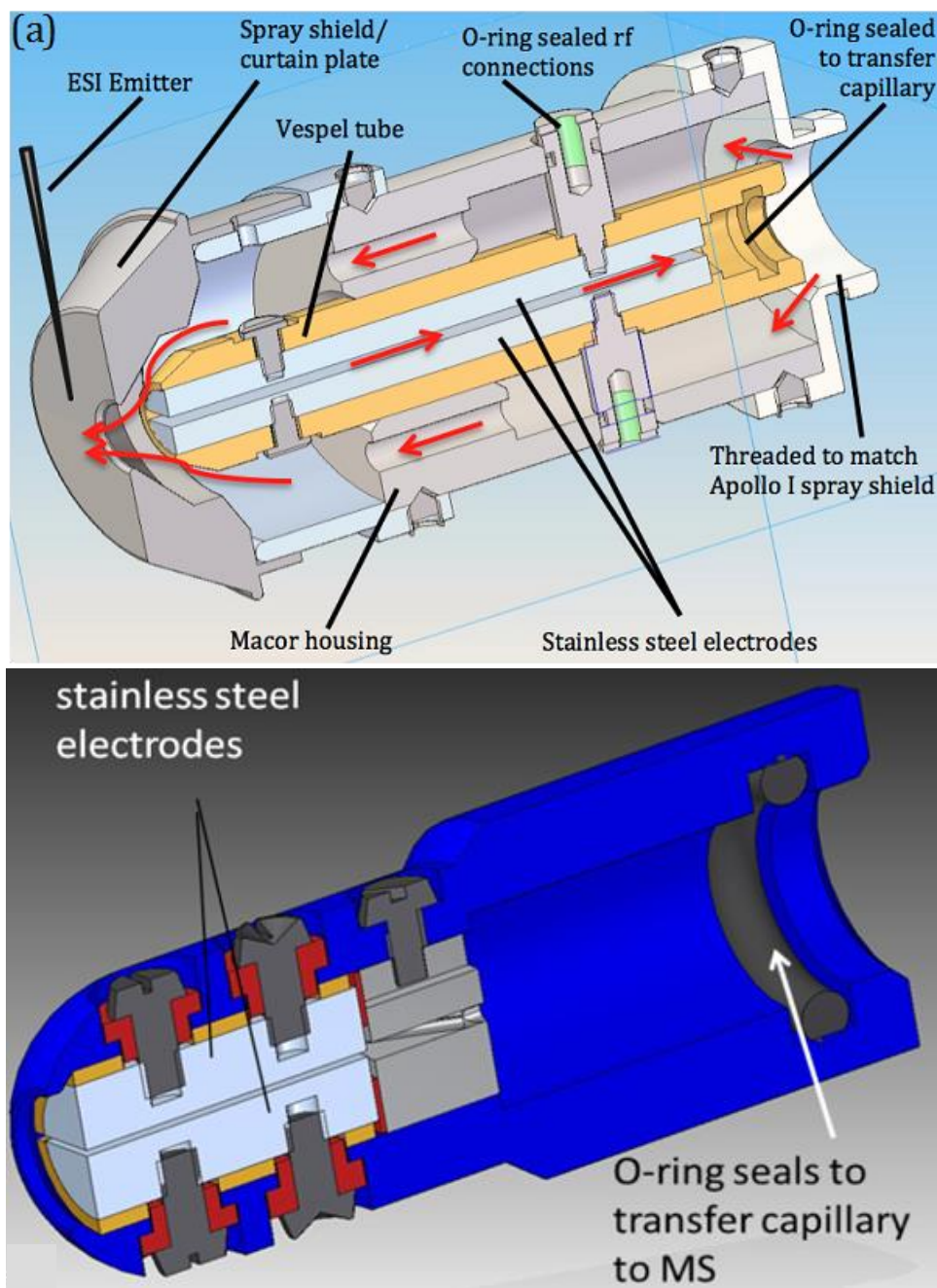


**Figure 2.2. (a) Planar DIMS assembly that couples to the Bruker Esquire 3000 ion trap mass spectrometer. The flow of the desolvation gas coming out of the instrument and the flow of the DIMS carrier gas are indicated by red arrows (b) Planar DIMS assembly that couples to the Bruker HCTUltra ion trap mass spectrometer without the housing that redirects the desolvation gas flow. The relative sizes between the two systems are not shown to scale**

Figure 2.2a, but is not shown for the system in Figure 2.2b. This housing design causes the entire DIMS system to be heated by the desolvation gas while also allowing the gas flow to maintain its function as a desolvation gas. The design also allows for the desolvation gas to be in excess at the entrance to the DIMS device at typical desolvation gas flow rates. Therefore the composition of the desolvation gas and the DIMS carrier gas are assumed to be the same.

That the actual temperature of the desolvation gas, and hence the DIMS carrier gas, is not as high as the set temperature in the mass spectrometer software because the temperature displayed in the software is measured at the heating block rather than the inlet to the DIMS device. As the desolvation gas travels from the heating block to the inlet of the DIMS device it transfers heat to the metal tubing and the DIMS housing. This results in the temperature of the desolvation gas at the inlet to the DIMS device being cooler than the temperature measured at the heating block. The flow rate of the desolvation gas also affects the temperature measured at the inlet to the DIMS device. A higher desolvation gas flow rate causes a greater amount of heat to be conducted to the gas transfer tubing and the DIMS device. Thus the desolvation gas, transfer tubing, and the DIMS device come to equilibrium at a higher temperature. The effect of this is that the temperature of the DIMS carrier gas is higher when greater desolvation gas flow rates are used for a given set temperature.

Each DIMS device used also had a corresponding custom-built power supply that provides both the dispersion voltage and the compensation voltage. Both power supplies produce DIMS waveforms of bisinusoidal design, where a sinusoidal waveform is applied to each DIMS electrode. A simplified depiction of this is shown in Figure 2.3, where the two waveforms are capacitively coupled across the DIMS gap and an asymmetric bisinusoidal waveform is created. This method is used rather than the more ideal square wave because of the lower power



requirements necessary for the bisinusoidal waveform [7]. The power supply for the DIMS device that couples to the Bruker Esquire 3000 outputs two sinusoidal waveforms approximately 90° phase shifted that are 1.7 and 3.4 MHz in frequency and 2:1 in amplitude, respectively. The power supply for the DIMS device that works with the Bruker HCTUltra also outputs two sinusoidal waveforms approximately 90° phase shifted and 2:1 in amplitude; however, the frequency of those waveforms are of 2 and 4 MHz, respectively.

One of the key differences between the two DIMS devices used in this work is the ability for the dispersion and compensation voltages applied to the DIMS device that couples with the Bruker HCTUltra to use the dc voltage applied to the inlet capillary of the mass spectrometer as

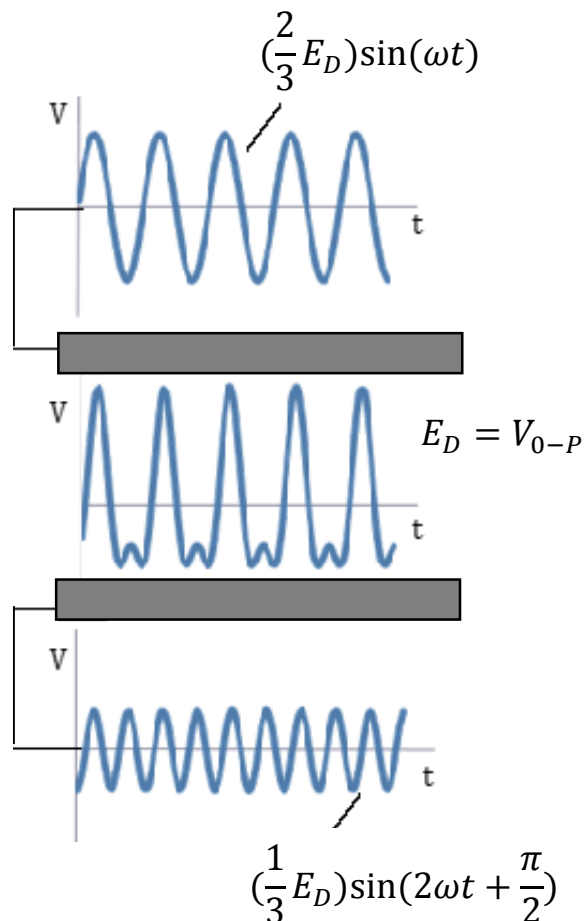


**Figure 2.3. Simplified depiction of the addition of two sinusoidal waveforms across the DIMS gap to form the asymmetric bisinusoidal waveform**

an electrical reference. This allows a voltage gradient from the ion source to the inlet of the DIMS device to exist when the ion source is held at ground potential. The ability to create this gradient while holding the ion source at ground potential affords greater ion source design options, and in the case of this work allows for the coupling of LTPI and DIMS. Additionally, using the inlet capillary voltage as an electrical reference for the DIMS voltages allows for the electrospray ionization source to be mounted in the door that encloses the source region of the mass

spectrometer. Mounting the sprayer in the door creates a direct electrical connection between the sprayer and the housing of the mass spectrometer, and therefore a sufficient voltage to cause electrospray cannot be applied to the sprayer. Use of the door also causes the source region to be more thoroughly heated by the dry gas flow, resulting in more efficient desolvation/evaporation prior to the inlet of the DIMS device or mass spectrometer. DIMS experiments performed using the DIMS device coupled to Esquire 3000 cannot utilize the door designed to enclose the ion source region, and the voltage gradient into the DIMS device must be generated by applying a voltage to the ion source.

DIMS scans performed with each DIMS device were controlled using a LabVIEW program interfaced to the instrument control software. Unless otherwise stated, the compensation voltage was increased after every 10 mass spectra recorded by the instrument. The time duration of each step in the DIMS scan was dependent upon the speed of the ion trap mass spectrometer and the number of spectra averaged. The same LabVIEW program was used to control the compensation field applied during experiments where the compensation field was parked to select for particular analyte ions.

## **2.4 Major Modifications to the Standard Workflows/Experimental Set-ups**

### **2.4.1. Chapter 3: Effects of Desolvation Gas Flow Rate and Temperature on DIMS Separations**

The work presented in Chapter 3 began using the DIMS device coupled to the Bruker Esquire 3000, with the spray voltages applied to the ESI and nESI sources and no door used to enclose the ion source region. When the work transitioned to the DIMS device that works with the Bruker HCTUltra the door was still not utilized, but the voltage gradient to the inlet of the DIMS device was created by using the spray voltage applied to the inlet capillary of the mass spectrometer as the ground reference for the DIMS device. The same experimental design was

used for the comparison between ions formed by ESI and LTPI. Not using the door assured that the gas dynamics and temperature of the source region were as consistent as possible between experiments using different ion sources. Further differences from the standard experimental workflows will be discussed in Chapter 3 within the context of the results.

#### 2.4.2. Chapter 4: Characterization of Variables Affecting Internal Energy Deposition inside a Differential Ion Mobility Spectrometer

Typically the mass spectrometer software is used to control both the desolvation gas flow and temperature. However, as the gas flow composition was varied from the standard 100% nitrogen for the work presented in Chapter 4, the instrument's built in mass flow controller could not be used to control the flow of the gas mixture. Instead, for the experiments using a 100% nitrogen carrier gas performed at a flow rate of 5.0 L/minute and temperature setting of 300 °C the instrument desolvation gas was disconnected prior to the heater and replaced with the output of a MKS model 1179 mass flow controller. For experiments with a mixed desolvation gas composition the instrument desolvation gas was again replaced, and the flow rate and composition were controlled through the MKS model 1179 and an Alicat MC-10SLPM-D mass flow controller.

As mentioned previously, the actual temperature of the desolvation gas, and hence the DIMS carrier gas, is not as high as the set temperature within the mass spectrometer software. The heat transfer to the DIMS device is dependent on the desolvation gas flow and the gas composition. The temperatures measured at the inlet to the DIMS device for each flow rate and composition used in Chapter 4 are listed in Table 2.1. The measurements were taken with a Klein Tool MM400 and a bead wire type K temperature probe.

Another difference between the experimental set-up used in Chapter 4 and the other work presented in this dissertation is the optimization of the ion optics of the mass spectrometer.

Typically the voltages applied to the ion optic components are optimized to yield the highest signal intensity for the analyte ions being studied. However, due to how easily the ions studied in Chapter 4 fragment, the voltage applied to both the skimmer and capillary exit was set to 10.0 V. This reduced the amount of fragmentation that occurred within the instrument ion optics so that intra-DIMS fragmentation could be more easily studied.

#### 2.4.3. Chapter 5: Improved Differential Ion Mobility Spectrometry Separations using Linked Scans of Carrier Gas Composition and Compensation Field

The linked scans presented in Chapter 5 were controlled using a LabVIEW program and a differential amplifier. The LabVIEW output directly controlled the nitrogen flow controller while the output of the differential amplifier controlled the helium flow controller. In this way, the total flow that was added to the 1.0 L/minute desolvation gas flow from the mass spectrometer was maintained at 4.0 L/minute. This total flow exceeds the gas flow drawn

Gas Composition	Gas Flow Rate	°C Setting	°C Measured
100% Nitrogen	5.0 L/minute	300 °C	133.4 ± 1.0
100% Nitrogen	5.0 L/minute	200 °C	91.7 ± 0.6
100% Nitrogen	7.5 L/minute	300 °C	155.8 ± 0.9
20% Helium	5.0 L/minute	300 °C	125.91 ± 0.3
20% Argon	5.0 L/minute	300 °C	131.2 ± 1.0
40% Argon	5.0 L/minute	300 °C	128.3 ± 0.6
20% Carbon Monoxide	5.0 L/minute	300 °C	133.7 ± 0.7
40% Carbon Monoxide	5.0 L/minute	300 °C	134.1 ± 0.8
60% Carbon Monoxide	5.0 L/minute	300 °C	134.0 ± 0.8

**Table 2.1. Table showing the temperature measured at the entrance to the DIMS device for each desolvation gas flow, temperature setting, and gas composition used during the experiments described in Chapter 4**

through DIMS by the mass spectrometer vacuum system by ~2 fold, and based on the geometry of the system the desolvation gas is expected to make up essentially the entirety of the carrier gas. The percent helium present in the carrier gas was stepped down every 10 spectra recorded by the instrument, with step size being dependent on the range of helium to be scanned. The helium reached the designated percentage in less than 2 seconds, allowing the helium content to move in synchrony with the compensation field scan. Compensation field scans and helium scans were set to an equal number of steps during each individual scan. The same LabVIEW program also allowed the helium percentage to be set at a particular value, as was done for compensation field scans with constant helium. These experiments were performed on the DIMS device coupled to the Bruker Esquire 3000, and therefore were done with the door to the source region of the mass spectrometer removed and the spray voltage applied to the ESI sprayer.

#### 2.4.5. Chapter 6: Improved Differential Ion Mobility Spectrometry Separations using Solvent Vapors

Many of the separations described in Chapter 6 implement the addition of solvent vapors to the DIMS carrier gas. This addition of solvent vapors was accomplished by adding a ¼ inch Swagelok® tee to the HCTultra desolvation gas line between the mass flow controller and the desolvation gas heater. As depicted in Figure 2.4, one side of the Swagelok tee was coupled to a Cole Palmer 74900 series syringe pump, which flowed solvent at a flow rate of 1.8 mL/hour into the path of the desolvation gas flow. This solvent flow rate results in the vapors being added at a much lower concentration compared to experiments where gases such as helium are mixed with the nitrogen carrier gas. For example, a flow rate of 1.8mL/hour of methanol equates to 0.045 moles/hour of methanol. Based on the assumption of an expansion at STP this equates to

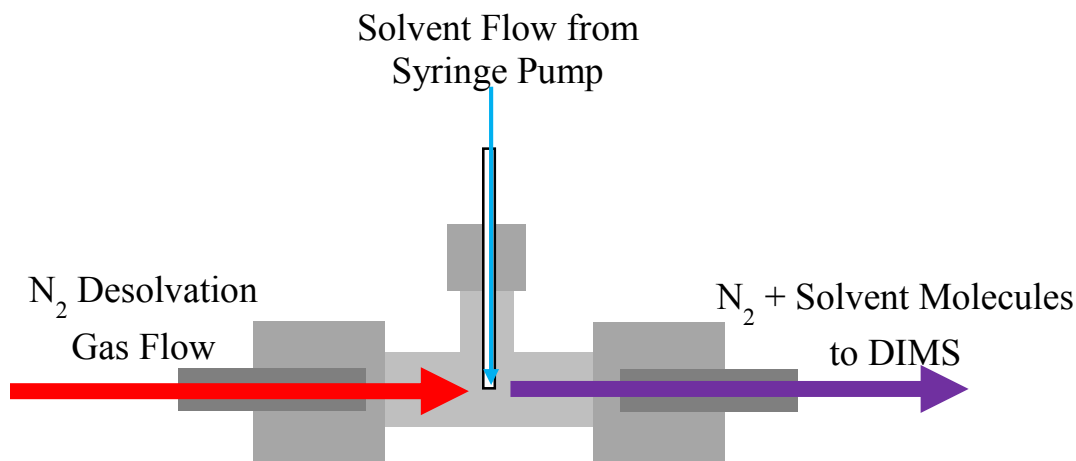


**Figure 2.4. Simplified depiction of the system used to add solvent vapors to the DIMS carrier gas. Tubing and Swagelok fittings are shown in grey**

1.0 L of gas, or 0.33% (v/v) when mixed with the 5 L/minute flow of the desolvation gas. During the experiments described in Chapter 6 that did not use solvent vapors the solvent was removed and the connection leading to the syringe was closed. Another adjustment to the experimental set-up was to lower temperature setting of the desolvation gas, and thus the carrier gas, to 200 °C.

## 2.5 Data analysis

For a majority of the work presented, peak centroids and widths were calculated using Microcal Origin 6.0, under the assumption of Gaussian distributions. Alternatively, some experiments in Chapters 3 and 5 used a Wolfram Mathematica 7.0 script, also under the assumption of Gaussian distributions. The program utilized for peak characterization was consistent within each comparison. The peak centroids and peak widths were used with the resolving power and resolution equations below (reprinted from Chapter 1) as part of the characterization of the DIMS separations taking place.

$$\text{Resolving Power} = \frac{E_C}{(\text{FWHM})} \quad (2.1)$$

$$\text{Resolution} = \frac{E_{C1} - E_{C2}}{\left(\frac{w_1 + w_2}{2}\right)} = \frac{1.178 (E_{C1} - E_{C2})}{(\text{FWHM}_1 + \text{FWHM}_2)} \quad (2.2)$$

Calculations comparing the peak capacities of separations when analyzing ions from a tryptic digest of BSA used the 50 most intense mass-to-charge peaks from the mass spectrum of BSA. During data analysis the extracted ion currents were plotted for these mass-to-charge ratios and the calculated peak statistics were used for the comparison. The identity of these peaks was not thoroughly investigated as the goal was to evaluate the separation capability for a complex mixture. Due to loss of analyte signal intensity upon the application of the DIMS waveform and use of helium in the carrier gas, not all 50 peaks were detected in each DIMS scan. Peak capacities were calculated using the centroid of the analytes detected requiring the highest and lowest compensation fields ( $E_{CH}$  and  $E_{CL}$ , respectively), and average FWHM of all analytes detected during the scan (Equation 2.3).

$$\text{Peak Capacity} = \frac{(E_{CH} - E_{CL})}{FWHM_{Avg.}} \quad (2.3)$$

## REFERENCES

1. Harper, J. D.; Charipar, N. A.; Mulligan, C. C.; Zhang, X. R.; Cooks, R. G.; Ouyang, Z. Low-Temperature Plasma Probe for Ambient Desorption Ionization. *Anal. Chem.* **2008**, *80*, 9097-9104.
2. Garcia-Reyes, J.; Harper, J. D.; Salazar, G. A.; Charipar, N. A.; Zheng, O.; Cooks, R. G. Detection of Explosives and Related Compounds by Low-Temperature Plasma Ambient Ionization Mass Spectrometry. *Anal. Chem.* **2010**, *83*, 1084-1092.
3. Isenberg, S. L.; Armistead, P. M.; Glish, G. L. Optimization of Peptide Separations by Differential Ion Mobility Spectrometry. *J. Am. Soc. Mass Spectrom.* **2014**, *25*, 1592-1599.
4. Santiago, B. G.; Harris, R. A.; Isenberg, S. L.; Ridgeway, M. E.; Pilo, A. L.; Kaplan, D. A.; Glish, G. L. Improved Differential Ion Mobility Separations using Linked Scans of Carrier Gas Composition and Compensation Field. *J. Am. Soc. Mass Spectrom.* **2015**, *26*, 1746-1753.
5. Santiago, B. G.; Harris, R. A.; Isenberg, S. L.; Glish, G. L. Resolving Powers of >7900 using Linked Scans: How Well does Resolving Power Describe the Separation Capability of Differential Ion Mobility Separations. *Analyst.* **2015**, *140*, 6871-6878.
6. Dharmasiri, U.; Isenberg, S. L.; Glish, G. L.; Armistead, P. M. Differential Ion Mobility Spectrometry Coupled to Tandem Mass Spectrometry Enables Targeted Leukemia Antigen Detection. *J. Proteome Res.* **2014**, *13*, 4356-4362.
7. Krylov, E. V.; Coy, S. L.; Vandermeij, J.; Schneider, B. B.; Covey, T. R.; Nazarov, E. G. Selection and Generation of Waveforms for Differential Mobility Spectrometry. *Rev. Sci. Instrum.* **2010**, *81*.



## **CHAPTER 3: EFFECTS OF DESOLVATION GAS FLOW RATE AND TEMPERATURE ON DIMS SEPARATIONS**

### **3.1 Solvent Vapors and Desolvation Gas**

The deliberate addition of solvent vapors to the DIMS carrier gas has been shown to improve differential ion mobility separations; however, the unintentional introduction of solvent molecules can inhibit accurate detection and quantitation of the analytes present in a sample [1-4]. Considerable efforts to maintain a highly controlled carrier gas have been made for many DIMS systems to avoid issues due to solvent vapor introduction via pathways such as humidity and gas impurities [1,2,5-7]. However, ionization techniques such as electrospray ionization (ESI) and nano-electrospray ionization (nESI) are often used for the analysis of nonvolatile analytes [8-13]. These ion sources introduce solvents into the area directly in front of the entrance to the DIMS device at concentrations that would be much higher than through pathways such as humidity, raising concern over the potential for introduction of solvents into the DIMS device.

The Bruker mass spectrometers used in this work implement a heated desolvation gas flow counter to the movement of ions into the transfer capillary of the instrument. This gas serves the dual role of keeping neutral molecules from entering the instrument and desolvating the ions formed using ion sources such as ESI. Both the DIMS device for the Esquire 3000 and the DIMS device for the HCTultra used in this work reroute the desolvation gas from the mass spectrometer such that it functions as both desolvation gas and the DIMS carrier gas as discussed

in Chapter 2. As this desolvation gas flow is typically a factor of 4-8 times higher than the gas flow into the DIMS device, the amount of solvent expected to enter into the DIMS device is not believed to be significant enough to affect the differential mobility of ions. In this chapter the effects of changing the flow rate or temperature of the desolvation gas flow are discussed, with particular attention being focused on the coupling of DIMS to ion sources that introduce different amounts of solvent into the area in front of the DIMS device.

### **3.2 Comparison of ESI and nESI**

Both ESI and nESI typically ionize samples via protonation or deprotonation at atmospheric pressure; however, the two ion sources function in different size and flow regimes. In ESI ions are generated by passing a solution-based sample through a capillary with an inner diameter (i.d.) less than 250  $\mu\text{m}$  at a flow rate typically greater than 500 nL/minute [11,14-16]. These values are significantly higher than those used in nESI sources, which have an i.d. of less than 10  $\mu\text{m}$  and use less than 100 nL/minute [11,14,15]. In both types of ion sources an aerosol of charged droplets is formed, which would ideally be evaporated prior to the ions entering the mass spectrometer or, for the experiments herein, the DIMS device [11,17,18]. The mean droplet size created by ESI sources is larger than that from nESI and typically requires a concentric flow of gas to assist in nebulization, along with higher desolvation gas temperatures and flow rates to fully desolvate ions [11,14,18]. Based on these differences in desolvation properties, a comparison between the coupling of ESI and nESI to a DIMS device was conducted at various desolvation gas temperatures.

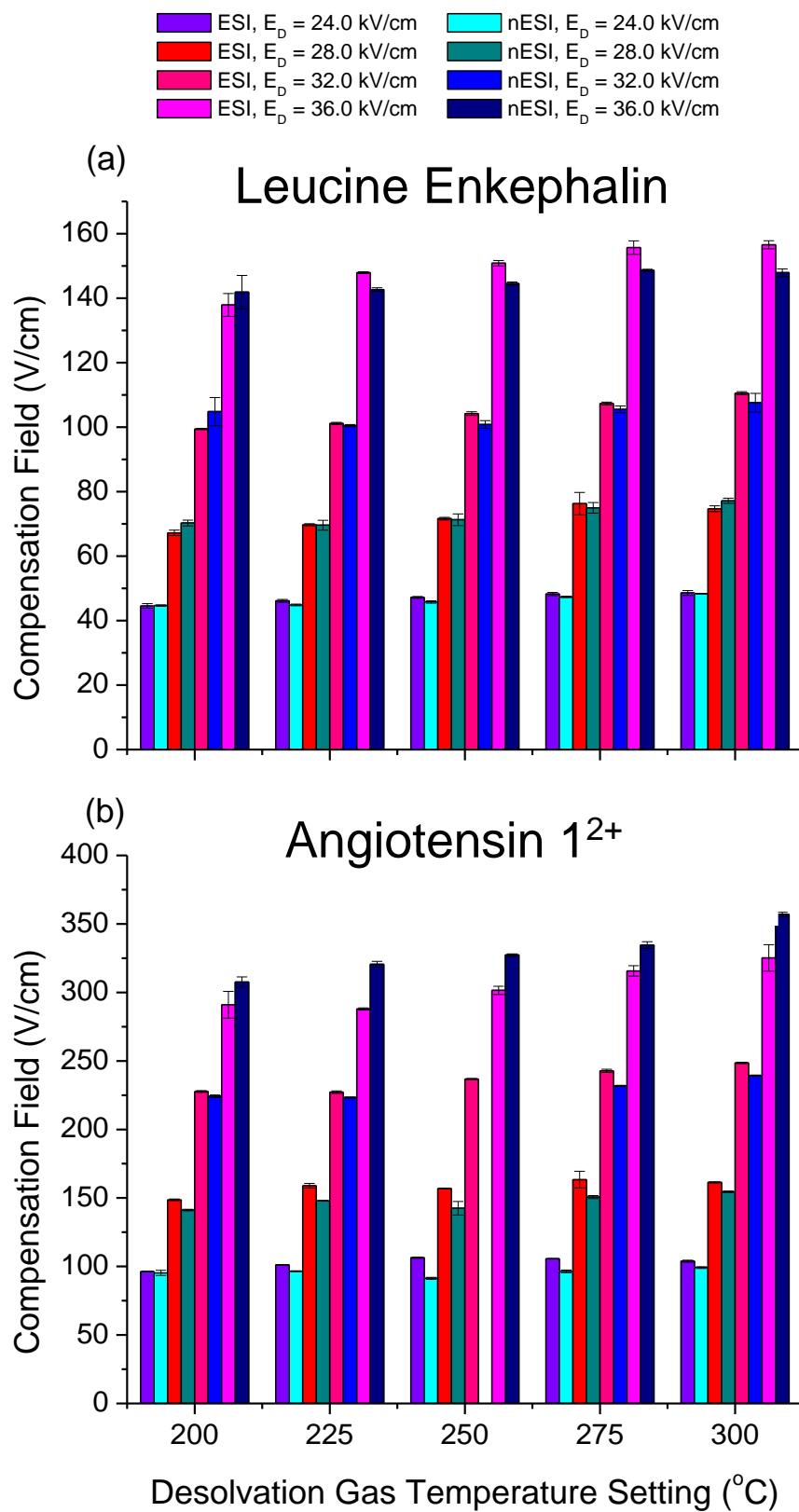
It was believed that the introduction of solvent into the DIMS device, potentially due to incomplete droplet evaporation when ESI and lower desolvation gas temperature were used, would cause dissimilarities in the differential mobility of ions based on the cluster-decluster

mechanism described in Chapter 1. This change in differential ion mobility would then be measured as an alteration of the compensation field ( $E_C$ ) necessary to pass the ions through the DIMS device and into the mass spectrometer. Studies were conducted using the DIMS device (0.5 mm gap) coupled to a Bruker Esquire 3000 ion trap mass spectrometer. A comparison of the characteristic  $E_C$  for the protonated species formed by ESI and nESI using a 50/49/1 methanol/water/acetic acid spray solvent mixture is shown in Figure 3.1. The desolvation gas temperature settings were varied between 200 and 300 °C (flow rate 5.0 L/minute), and  $E_C$  scans were performed at dispersion fields ( $E_D$ ) stepped between 24.0 and 36.0 kV/cm. ESI and nESI were used to form  $[M+H]^+$  leucine enkephalin (Figure 3.1a),  $[M+2H]^{2+}$  angiotensin 1 (Figure 3.1b), and  $[M+H]^+$  caffeine (Figure 3.1c) ions. Each ion has the same characteristic  $E_C$  when formed by ESI or nESI, and thus the same differential ion mobility. Although some differences might exist within a single set of experiments, such as  $[M+2H]^{2+}$  angiotensin 1 ions formed by nESI having a higher  $E_C$  than ions formed by ESI when a  $E_D = 36.0$  kV/cm is used, these differences are not consistent across the three analytes and four  $E_D$ . Neither ESI nor nESI give consistently higher  $E_C$  throughout the experiments, suggesting the error is due to variability in the dispersion field applied rather than a true difference in  $E_C$  or the extent of solvation. Based on these results it is believed that at desolvation gas temperature settings between 200 and 300 °C either no solvent enters the DIMS device or an equal amount of solvent is present within the DIMS device during the use of both ion sources.

### **3.3 Comparison of ESI and Low Temperature Plasma Ionization**

#### **3.3.1. Dinitrotoluene and Caffeine**

Despite the differences in solvent flow and droplet size between ESI and nESI, the two ion sources both inherently introduce solvent into the space directly in front of the entrance to the



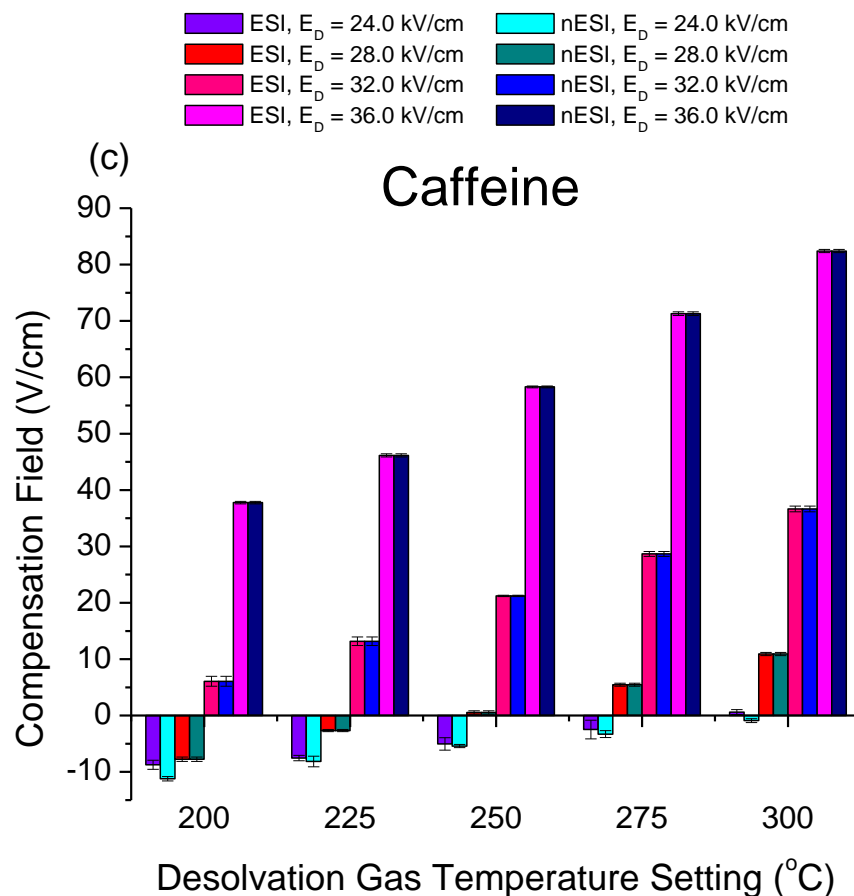


**Figure 3.1. Plot of the characteristic  $E_C$  for (a) leucine enkephalin, (b) angiotensin  $1^{2+}$ , and (c) caffeine as a function of desolvation gas temperature setting**

DIMS device. To further investigate how solvent from the ion source might affect the differential mobility of an ion, the measured  $E_C$  was compared for ions formed by ESI and low temperature plasma ionization (LTPI). Using no solvent, LTPI utilizes a dielectric barrier discharge to generate a reaction cascade that in this work results in the protonation or deprotonation of the analyte molecule [19,20]. Thus, a comparison between ESI and LTPI would allow for determination of whether the use of ESI and nESI resulted in equal amounts of solvent being introduced to DIMS or insufficient solvent to cause a measurable effect. The characteristic  $E_C$  was measured for caffeine, dinitrotoluene (DNT), and o-phthalic acid using the DIMS device coupled to the Bruker HCTultra with desolvation gas settings of 300 °C and 5.0 L/minute. DNT and o-phthalic acid have been shown in the literature to undergo shifts in characteristic  $E_C$  upon

the addition of water or methanol to the DIMS carrier gas, and our work has shown that the characteristic  $E_C$  of caffeine shifts upon the addition of methanol to the DIMS carrier gas [3]. As example of the changes in  $E_C$  observed for the protonated caffeine ion when as little as 0.33% (v/v) methanol is added to the carrier gas is shown in Figure 3.2. Despite the relatively small amounts of solvent needed to cause a change in  $E_C$ , it is shown in Figure 3.3 that ionization via ESI or LTPI resulted in no difference in characteristic  $E_C$  for the protonated caffeine and deprotonated DNT ions. These results furthered the belief that when using ion sources such as ESI or nESI that either no solvent entered the DIMS device or that insufficient solvent is present in the DIMS device to affect differential ion mobility.

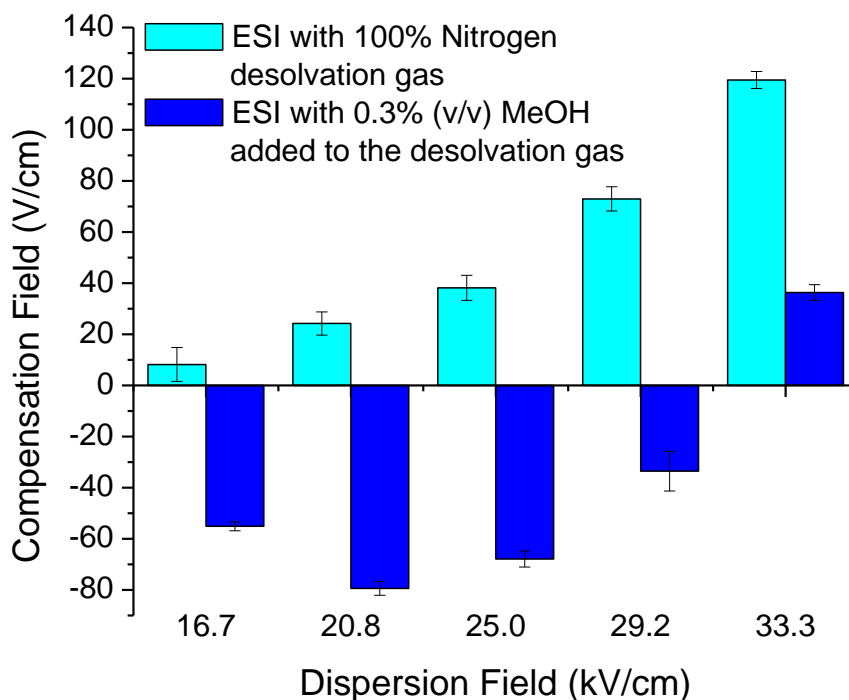


**Figure 3.2. Plot showing the characteristic  $E_C$  for caffeine when no solvent vapor is added to the carrier gas and when 0.33% methanol is added**

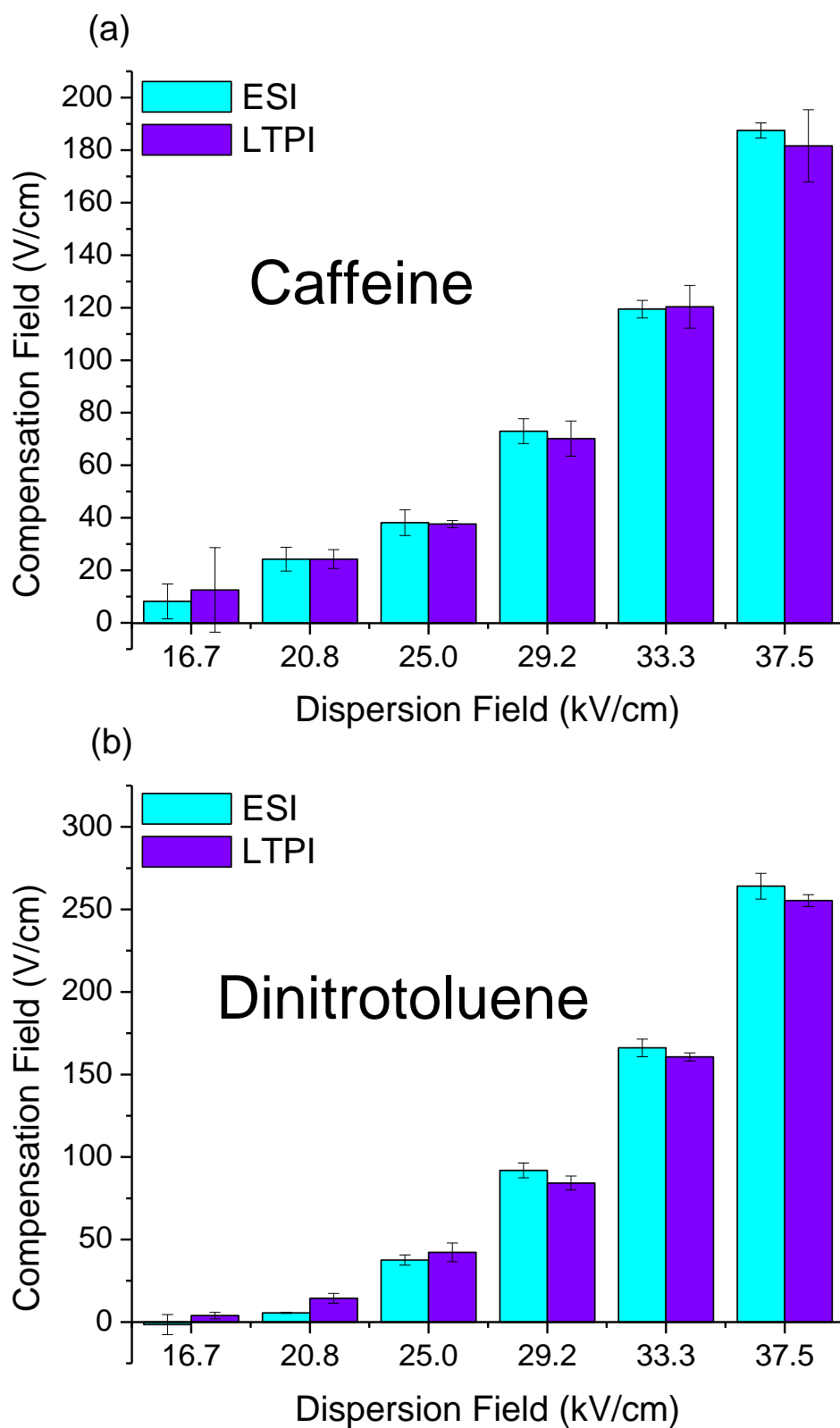


**Figure 3.3. Plots of the characteristic  $E_c$  for (a) caffeine and (b) DNT ions formed by ESI and LTPI**

### 3.3.2. o-Phthalic Acid

During the comparison of ESI and LTPI with o-phthalic acid as the analyte, significant differences were observed in  $E_C$  for the ions formed using the two ion sources. Shown in Figure 3.4, the ions produced via ESI initially passed through DIMS at a higher  $E_C$  than ions formed by LTPI before shifting to a considerably lower required  $E_C$  at higher  $E_D$ . To verify that this drop in  $E_C$  was not due to the accidental application of an incorrect  $E_D$ , the required  $E_C$  was measured at three higher  $E_D$ . Both the differences in  $E_C$  between ion sources and the different trends in response to  $E_D$  pointed to the introduction of droplets or solvent molecules into the DIMS device in a sufficient quantity as to change the differential ion mobility of the o-phthalic acid ions. However, the pattern of required  $E_C$  as a function of  $E_D$  also did not match those measured during the intentional addition of dopants to the carrier gas for other analytes. An increase in  $E_C$  followed by a sharp decrease, rather than a decrease and subsequent increase like

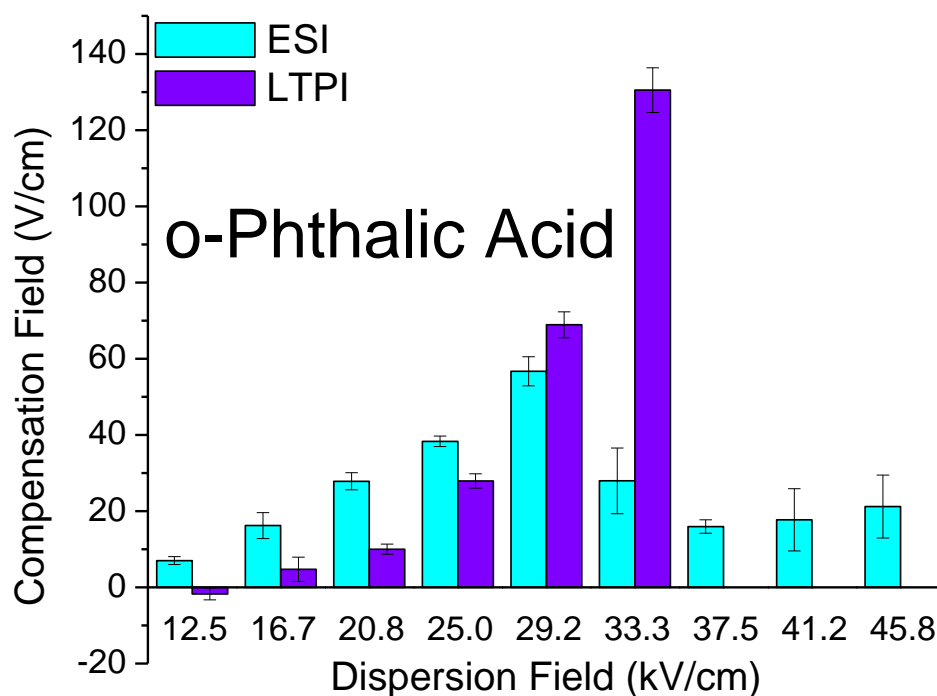


**Figure 3.4. Initial plots of the characteristic  $E_C$  for o-phthalic acid ions formed by ESI and LTPI**



that shown in Figure 3.2, caused suspicion that an unforeseen difference might have arisen. During the initial comparison between ESI and LTPI for o-phthalic acid the instrument optics were optimized for  $m/z$  165, the mass-to-charge ratio of deprotonated o-phthalic acid. Upon changing the ion optics settings to more favorably pass ions with higher mass-to-charge ratios peaks were detected at  $m/z$  353 and 541, which potentially corresponded to the sodium bound dimer ( $[2M-2H+Na]^-$ ) and trimer ( $[3M-3H+2Na]^-$ ) of deprotonated o-phthalic acid ions. Although sodium was not added to the samples, it not an uncommon occurrence for sodium contamination of the solvents or glassware used to prepare samples to occur. Tandem mass spectrometry of the peak at  $m/z$  541 yielded the mass spectra shown in Figure 3.5. The neutral losses confirmed that the peaks were the sodium bound oligomers of deprotonated o-phthalic acid, the presence of which gave a clue about the unexplained differences between how the ions formed via ESI and LTPI travelled through the DIMS device.

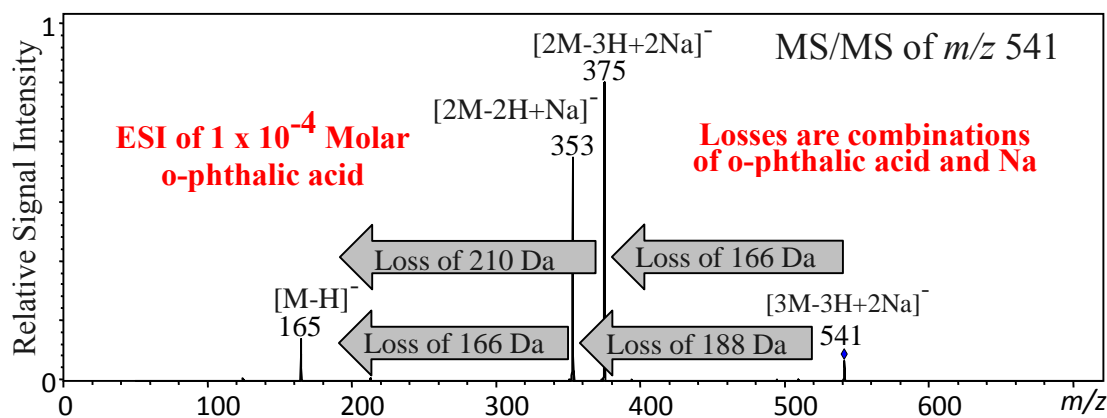


**Figure 3.5. Mass spectrum generated by tandem mass spectrometry of ions of  $m/z$  541**

To explain how those oligomers might be affecting the detection of the deprotonated o-phthalic acid monomer, a brief description of ion optics is required. For mass spectrometers to be coupled with atmospheric ionization techniques, ions formed at atmospheric pressure must be transferred into the vacuum of the mass spectrometer. This is commonly done using a transfer capillary followed by ion optic components [21-23]. An example of how this is done is shown in Figure 3.6, where the transfer capillary and ion optics of the Bruker HCTultra are depicted. Though the voltage settings within the ion optics are typically set to optimally pass the mass-to-charge ratio of the analyte of interest, the voltages also produce a voltage gradient along which ions are drawn. The acceleration due to this voltage gradient and the lower than atmospheric pressures that exist in the first differential pumping region of the mass spectrometer (2.0 Torr in the HCTultra) combine to cause collisions between the ions and the gas molecules present that can increase the internal energy of the ions and result in fragmentation. When ions pass through the capillary as a loosely bound oligomer, such as is the case with the sodium bound oligomers of deprotonated o-phthalic acid, this increase in internal energy can cause the oligomer to break apart and be analyzed and detected as the monomer.

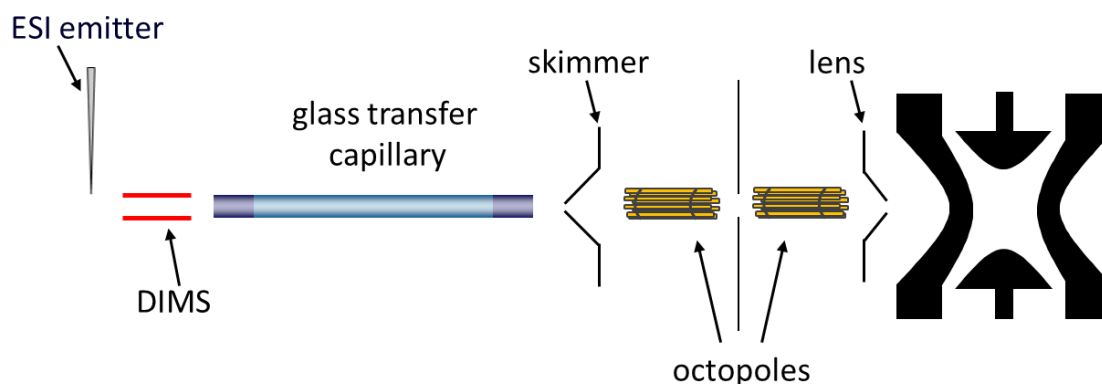


**Figure 3.6. Basic schematic of the Bruker HCTultra including the DIMS device. The voltages applied to the exit of the capillary and the skimmer when the instrument was tuned for  $m/z$  165 were -103.4 V and -40.0 V, respectively**

It is believed that this fragmentation of sodium bound oligomers to the deprotonated o-phthalic acid monomer post-DIMS was the cause for the irregularities shown in Figure 3.4. If a deprotonated monomer passes through the DIMS device as part of a sodium bound oligomer, and the oligomer subsequently fragments within the ion optics of the mass spectrometer to the deprotonated monomer, the deprotonated monomer will be detected at the  $E_C$  necessary to stably pass the sodium bound oligomer through the DIMS device. If DIMS is unable to fully separate the deprotonated monomer and the sodium bound oligomers, as occurs in Figure 3.7, the signal for the deprotonated monomer formed in the ion source and the deprotonated monomer formed in the ion optics will sum. This will cause the peak for  $m/z$  165 to be centered at a  $E_C$  shifted towards the  $E_C$  of the sodium bound oligomer.

Also shown in Figure 3.7 is the trace of  $m/z$  121, which is the main product ion detected when tandem mass spectrometry is performed on the deprotonated monomer of o-phthalic acid. This fragment is also detected due to the fragmentation of o-phthalic acid in the ion optics of the mass spectrometer, which was confirmed with experiments using LTPI. Although enough internal energy can be deposited into the oligomer to cause fragmentation to the ion of  $m/z$  121, the fragment ion at  $m/z$  121 is formed more readily when the monomer enters the ion optics than when the oligomer does, and therefore would be detected at the true characteristic  $E_C$  of deprotonated o-phthalic acid monomer ions. In Figure 3.7 it is shown that the fragmentation of the sodium bound dimer to the deprotonated monomer shifts the characteristic  $E_C$  for  $m/z$  165 away from the  $E_C$  of  $m/z$  121, and fitting the peak for  $m/z$  165 with multiple Gaussian fits using Origin 6.0 yields the two distributions of ions shown in Figure 3.8a. Of those two distributions the characteristic  $E_C$  of one closely aligns with the ion detected at  $m/z$  121 whereas the other corresponds to that of the sodium bound dimer detected at  $m/z$  353.

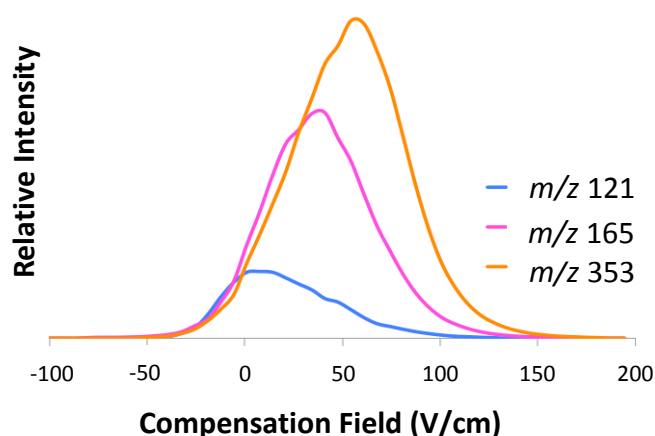


**Figure 3.7. DIMS scan of o-phthalic acid using ESI as the ionization technique**

In an attempt to reduce the amount of sodium bound oligomer present during the analysis, 10  $\mu\text{L}$  of 15-crown-5 ether was added to 1 mL of  $1 \times 10^{-4}$  o-phthalic acid solution. Crown ethers have been shown to bind to sodium ions, and it was supposed that insufficient sodium would be available for sodium bound deprotonated o-phthalic acid oligomers to form during ESI after the addition of the 15-crown-5 ether to the solution [24]. An example compensation field scan of this solution at  $E_D = 16.7$  kV/cm shown in Figure 3.8b, where the trace of  $m/z$  165 is overlaid with an  $E_C$  scan of o-phthalic acid performed after ionization via LTPI. The key point of this figure is the obvious difference in peak width when 15-crown-5 ether was added to the ESI solution. This is believed to have occurred due to the simultaneous attachment of both o-phthalic acid and 15-crown-5 ether molecules to the sodium present in solution. Thus, the ions traveled through the DIMS device as a cluster consisting of an unknown and variable number of o-phthalic acid and 15-crown-5 ether molecules attached to sodium. This led to a large distribution of differential ion mobilities and a wide array of  $E_C$  that pass the cluster through the DIMS device and into the mass spectrometer. Once inside the mass spectrometer the

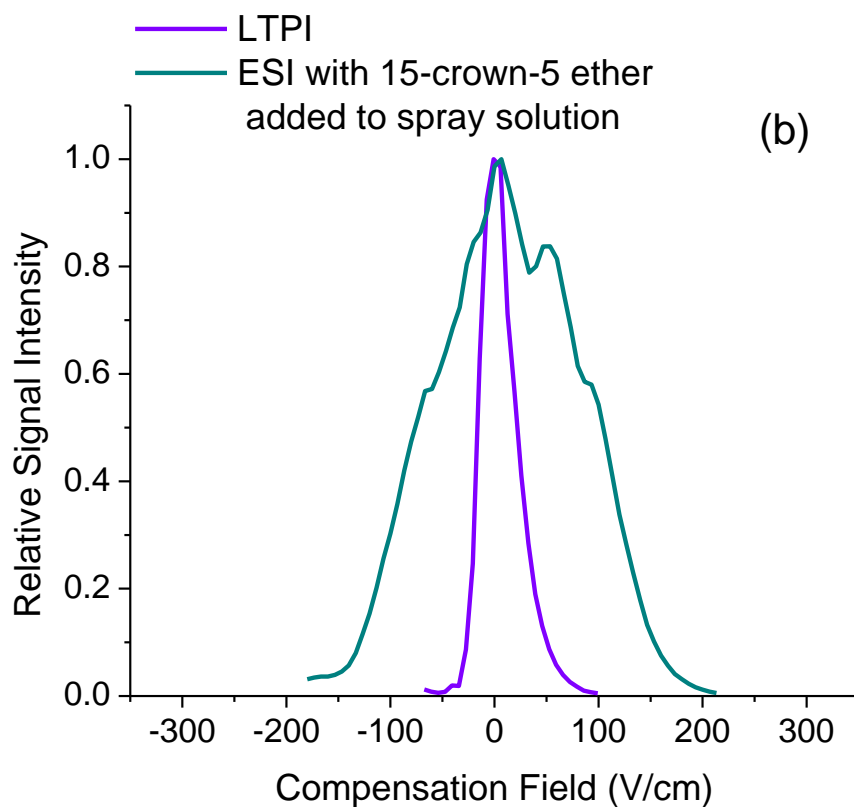
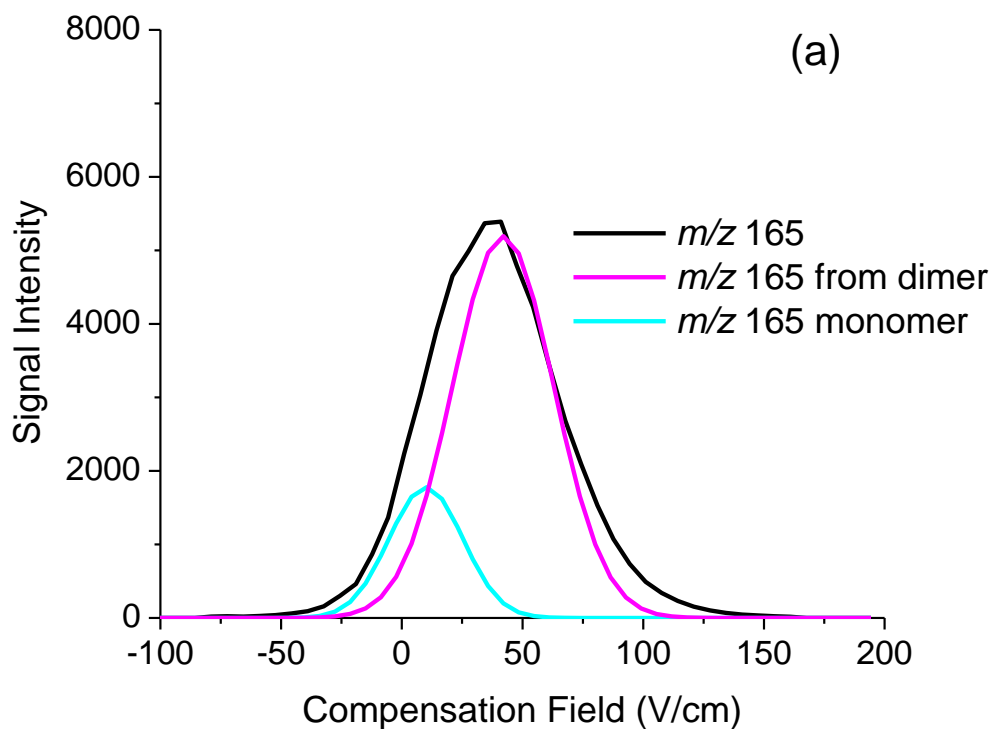


**Figure 3.8. (a) DIMS scan of o-phthalic acid fit with two Gaussian peaks using Origin 6.0 (b) DIMS scans of o-phthalic acid using LTPI and ESI as the ionization techniques. The sample ionized by ESI included 15-crown-5 ether**

cluster was fragmented in the ion optics and detected as the deprotonated monomer of o-phthalic acid at  $m/z$  165.

To more closely approximate the environment produced when ESI is used as an ion source while avoiding the formation of sodium bound oligomers, ionization by LTPI was used and an ESI sprayer held at ground potential was placed near the DIMS entrance as shown in Figure 3.9. The solvent flow rate through the ESI sprayer and the distance from the DIMS inlet were kept consistent with typical ESI experiments; however, with this experimental set-up the ESI sprayer was angled at  $\sim 45^\circ$  from the typical upright position. It is believed that because of the shape of the nebulized solvent plume an equal amount of solvent would be introduced in front of the inlet as when ESI is used, which allowed for the determination of whether or not the introduction of solvent affected the characteristic  $E_C$  of o-phthalic acid. The outcome of the

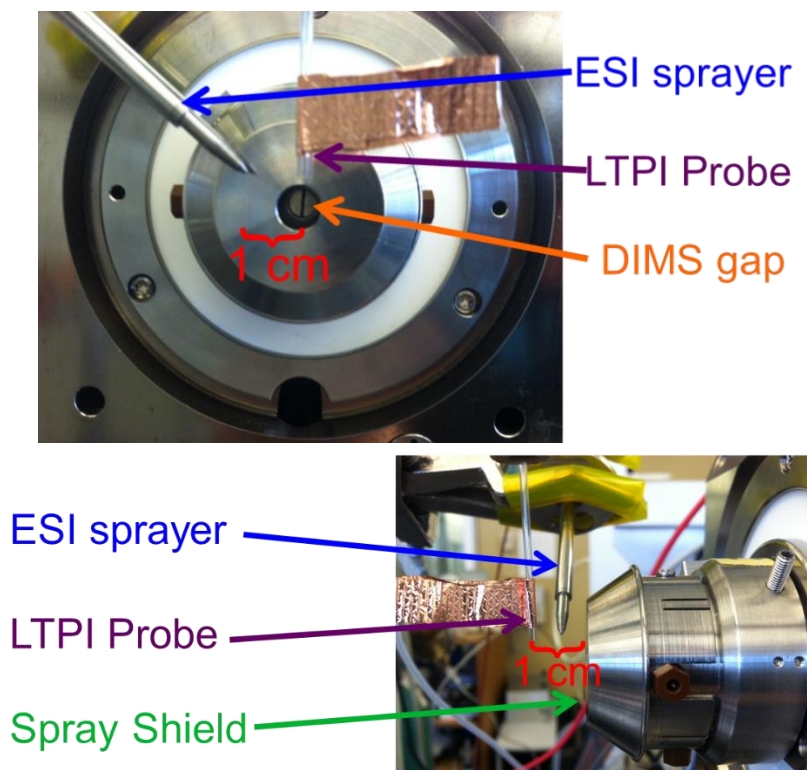


**Figure 3.9. Pictures of the ion source setup combining LTPI ionization with the introduction of solvent to the space directly in front of the DIMS device**

comparison between LTPI and LTPI with solvent present is shown in Figure 3.10. As with caffeine and DNT, the solvent flow from the ESI sprayer was insufficient to cause a change in the characteristic  $E_C$  of the analyte ions. Therefore it is believed that at desolvation gas settings of 5.0 L/minute and 300 °C there is not enough solvent from ESI present in the DIMS device to affect the  $E_C$  at which analyte ions are detected.

### 3.4 Effects of Desolvation Gas Flow and Temperature Setting: ESI vs. LTPI

Although the previous experiments provided evidence that the desolvation gas settings most commonly used on the Bruker HCT in our laboratory provided sufficient desolvation prior to DIMS analysis, novel experiments or ion sources might require different desolvation gas settings. To further study how low desolvation gas flow and temperature settings might influence the desolvation of ions prior to their entering the DIMS device, ESI and LTPI were compared using DNT as the analyte of choice. In Figure 3.11 it is shown that the characteristic  $E_C$  of DNT ions formed by ESI and LTPI are the same, whether a desolvation gas temperature setting of 200

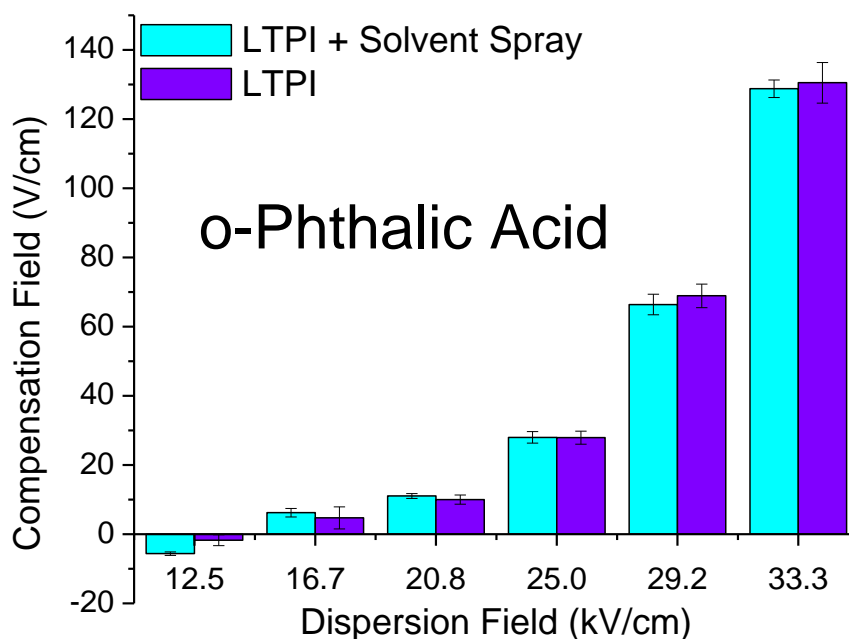


**Figure 3.10. Plot of the characteristic  $E_C$  for o-phthalic acid ions formed by LTPI and LTPI in the presence of 50/50 (v/v) methanol/water**

or 100 °C (flow rate = 5.0 L/minute) is used. The shift from negative  $E_C$  to positive  $E_C$  in Figure 3.11 can be explained in terms of DNT behaving at these temperatures as an ion with mobility that first increases and then decreases as a function of  $E/N$ . This is in contrast to Figure 3.3, where the higher temperature results in greater  $E/N$ , causing the mobility of DNT ions to only decrease as electric field strength increases.

Upon examination of the FWHM of the peaks, shown in Figure 3.12a, it is revealed that when using ESI with a desolvation gas temperature setting of 100 °C the average FWHM at some  $E_D$  is greater than those typically observed. Closer review of the spectra showed that at both low and high  $E_D$  the peak for DNT overlaps with peaks for a significant number of background ion species which appear to affect the measured peak width for DNT ions

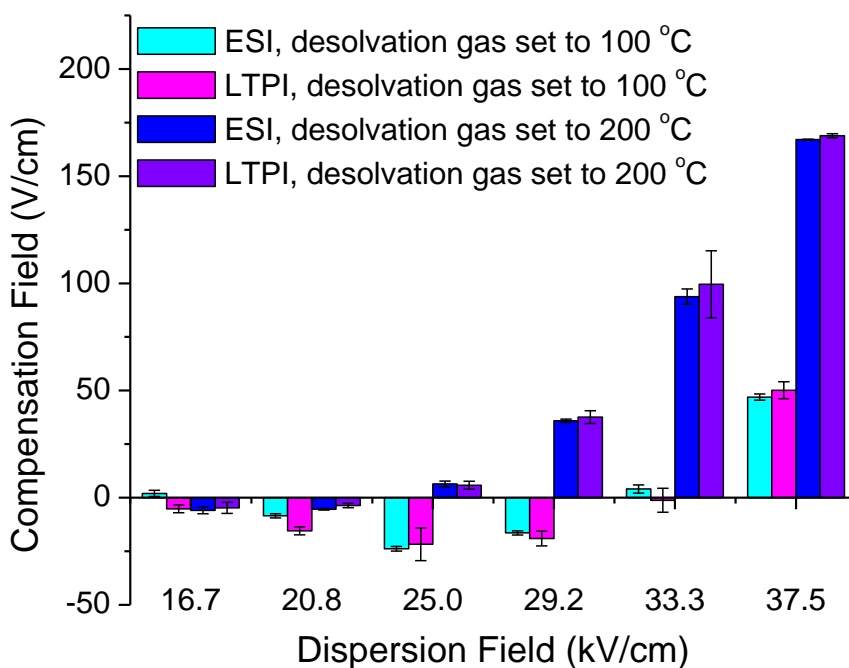


**Figure 3.11. Plot of the characteristic  $E_C$  of DNT ions formed by ESI and LTPI at desolvation gas temperature settings of 100 and 200°C**



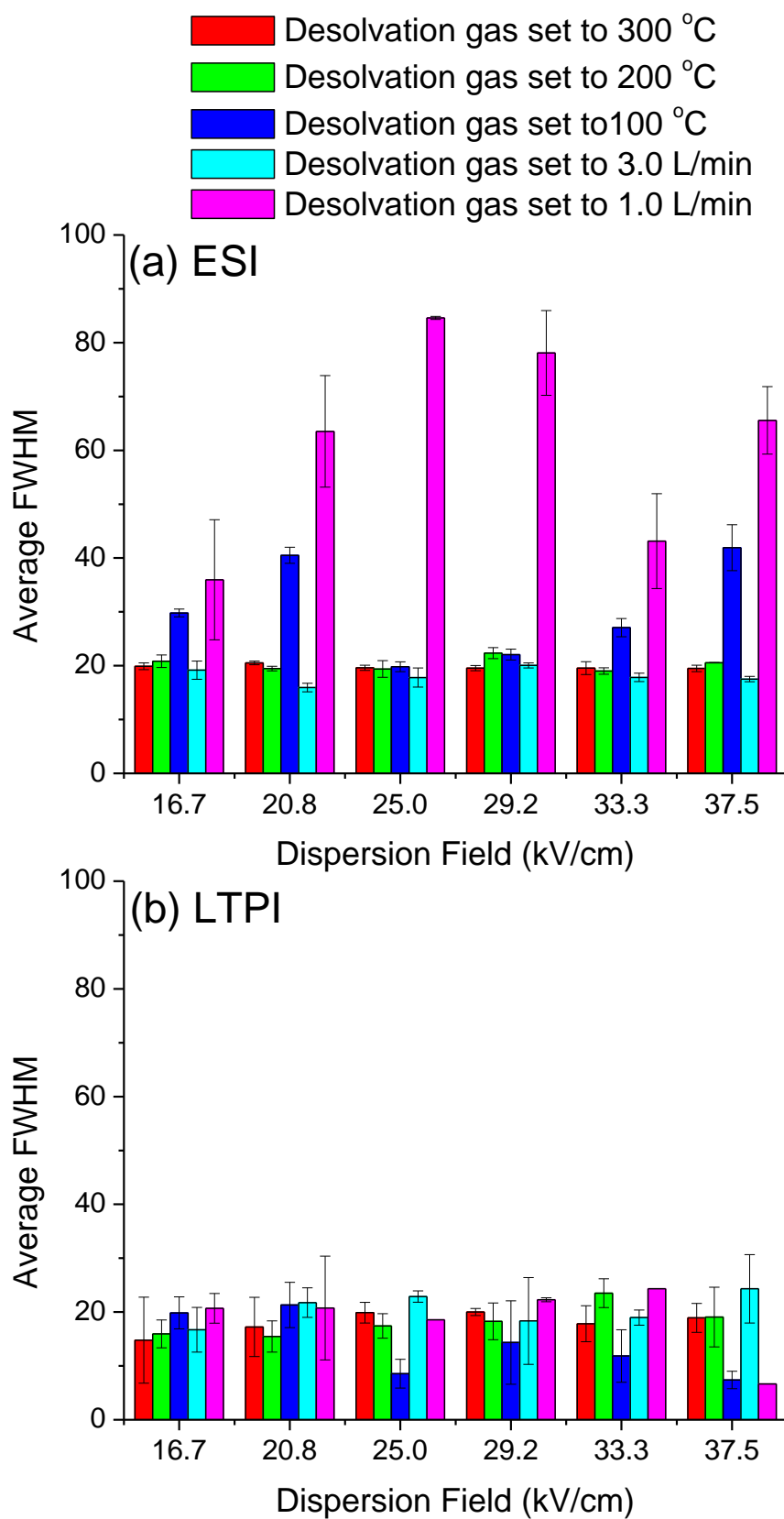


**Figure 3.12. Plots of the FWHM of peaks in DIMS scans formed by tracing  $m/z$  181. Ions are formed by ESI in (a) and LTPI in (b)**

in some way. The lower temperature setting causes the DNT signal intensity to drop such that it is on the same order of magnitude as that of the background ions, and also coalesces the characteristic  $E_C$  of DNT and the background ions at particular field strengths. At those field strengths DNT peak widths are slightly higher than the normal values. One potential cause might be a low intensity background ion that is isobaric to DNT and was not detected at higher temperatures; however, the cause of this issue was not further studied. At  $E_D$  of 25.0 and 29.2 kV/cm the overlap of the DNT signal and that of the background ions is minimal in the  $E_C$  domain, and thus the FWHM of the DNT peaks is expected to be representative of solely the DNT ions. As such, reducing the temperature is not believed to cause solvent to enter into the DIMS device because the FWHM at those two  $E_D$  is the same as during experiments using hotter carrier gas settings and LTPI (Figure 3.12b).

Shown in Figure 3.13, lowering the desolvation gas flow rate to 3.0 L/minute (temperature setting = 300 °C) resulted in no significant change in  $E_C$  for ions formed by ESI versus LTPI. However, at the same temperature setting further reducing the desolvation gas flow rate to 1.0 L/minute resulted in changes in the measured  $E_C$ , the data for which is also shown in Figure 3.13. Although these changes are significant, they do not completely portray the magnitude of the changes that occur when the desolvation gas flow rate is lowered to this extent. The changes in FWHM of the DNT peak are shown in 3.12, where a desolvation gas flow rate of 1.0 L/minute gives notably higher average FWHM at all  $E_D$  when ESI is used. Though it might be suspected the change in FWHM is due once again to the overlap of the DNT peak with background ion peaks, the peaks for those background species undergo the same transition to much more broad peaks. This data is suggestive of a concentration of solvent in the DIMS device high enough to affect differential ion mobility, yet too low to allow for each ion to reach the

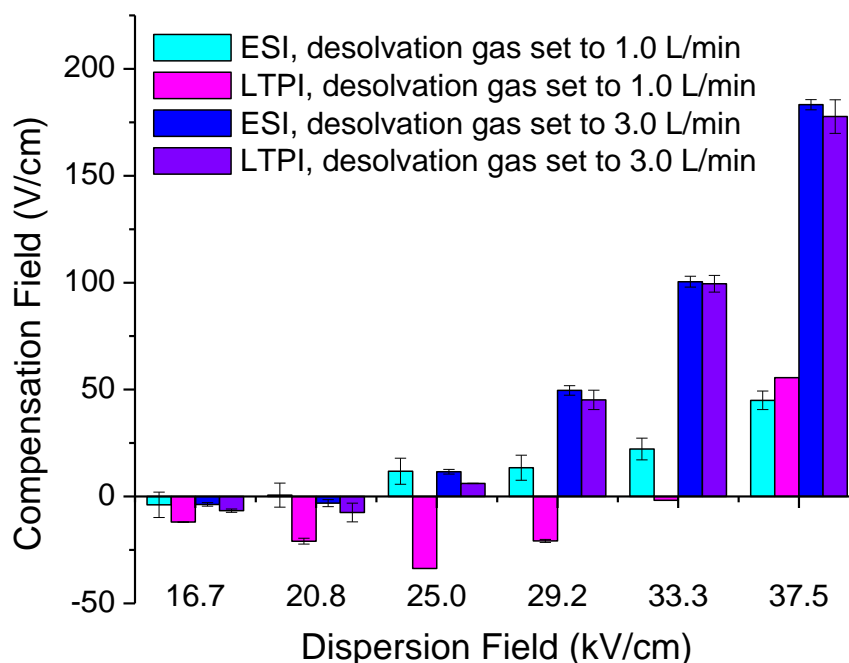


**Figure 3.13. Plot of the characteristic  $E_c$  of DNT ions formed by ESI and LTPI at desolvation gas flows of 1.0 and 3.0 L/minute**

same solvation level. Had the solvent concentration been high enough for the ions to all reach the same solvation level, a peak width similar to the FWHM during standard experiments would have been measured [3].

This intake of solvent into the DIMS device is consistent with the fact that the gas flow into the DIMS device is on the order of 0.6 L/minute, and that at a desolvation gas flow of 1.0 L/minute the desolvation gas is no longer in as an extreme of an excess. At this small of an excess it could be expected that the volume between the DIMS device and the ESI sprayer is significantly cooler. This will result in less evaporation/desolvation and the ions would travel in larger droplets. The lower excess of flow would then be unable to sufficiently redirect the larger droplets, as they are drawn in by the flow of gas into the mass spectrometer along with the charge of the ions in the droplet and the voltage gradient between the ESI sprayer and the entrance to the DIMS device. Thus, both ions and solvent molecules would enter into the DIMS device, where a cluster-decluster mechanism could then take place.

### 3.5 Summary and Conclusions

The use of ion sources that use solvents has become widespread; however, the introduction of solvents directly in front of a DIMS device can present challenges. Insufficient desolvation prior to DIMS analyses can drastically alter the separation characteristics and the necessary  $E_C$  to pass ions through the DIMS device. Using desolvation gas settings of 5.0 L/minute and temperatures between 200 and 300 °C, a comparison of the  $E_C$  required for multiple analyte ions formed by ESI and the more easily desolvated nESI was conducted. The results of these experiments provided evidence that either no solvent passes through the DIMS device with the ions, or that a similar enough amount of solvent was permitted between the DIMS electrodes during use of each ion source as to not cause significant differences in the  $E_C$  measured.

This work was corroborated by experiments comparing caffeine and DNT ions formed using either ESI or LTPI. Although these analytes had previously been shown to be affected by the introduction of solvent into the DIMS carrier gas, in this case no change in  $E_C$  was observed. After initial experiments using o-phthalic acid were complicated by sodiated oligomers, an experimental setup in which ions were formed using LTPI in the presence of solvent supplied by an ESI sprayer was utilized. This setup also yielded no difference in measured  $E_C$  between experiments with and without solvent present. These results led to the conclusion that at desolvation gas settings of 5.0 L/minute flow and 300 °C either no solvent is permitted into the DIMS device or only an amount insufficient to change  $E_C$  enters the device.

To expand on the effects of the desolvation gas, additional experiments at lower desolvation gas temperature and flow rate settings were performed. At desolvation gas settings of 200 °C and 5.0 L/minute no changes in  $E_C$  were observed when comparing DNT ions formed by ESI or LTPI. Further lowering of the temperature setting to 100 °C also resulted in no change in

$E_C$ ; however, inspection of the peak widths shows the introduction of inconsistencies in FWHM. Upon closer examination these inconsistencies were attributed to a combination of lower signal intensities for DNT and overlap with background ions. The DNT peaks at  $E_D$  where there was not considerable overlap with the background peaks gave the same FWHM for DNT as standard experimental conditions. Thus, it was determined that lowering the desolvation gas temperature setting to 100 °C did not introduce solvent into the DIMS device.

A comparison at desolvation gas settings of 300 °C and 3.0 L/minute showed no change in  $E_C$  between ions formed by ESI and LTPI, but lessening the gas flow to 1.0 L/minute resulted in changes in  $E_C$ . In this case, the comparison shows a considerable difference in both characteristic  $E_C$  and peak FWHM. The peak widths when using ESI at these settings are approximately 2-4 times greater than those observed at all other desolvation gas settings, strongly suggesting the introduction of solvent into the DIMS carrier gas in significant quantities. Based on these findings it is suggested that the desolvation gas settings be kept greater than the discussed values at which peak broadening occurs, as not doing so could result in the introduction of solvent into the DIMS device in sufficient quantities to affect the measured differential ion mobilities.

## REFERENCES

1. Krylova, N.; Krylov, E.; Eiceman, G. A.; Stone, J. A. Effect of Moisture on the Field Dependence of Mobility for Gas-Phase Ions of Organophosphorus Compounds at Atmospheric Pressure with Field Asymmetric Ion Mobility Spectrometry. *J. Phys. Chem. A*. **2003**, *107*, 3648-3654.
2. Eiceman, G. A.; Krylov, E. V.; Krylova, N. S.; Nazarov, E. G.; Miller, R. A. Separation of Ions from Explosives in Differential Mobility Spectrometry by Vapor-Modified Drift Gas. *Anal. Chem.* **2004**, *76*, 4937-4944.
3. Rorrer, L. C. R. L. C.; Yost, R. A. Solvent Vapor Effects on Planar High-Field Asymmetric Waveform Ion Mobility Spectrometry. *Int. J. Mass Spectrom.* **2011**, *300*, 173-181.
4. Obee, T. N.; Piech, M.; Mantese, J. V.; Dardona, S. Effect of Water Vapor and Formaldehyde Detection with Differential Mobility Spectrometry. *Int. J. Ion Mob. Spectrom.* **2012**, *3*, 131-139.
5. Barnett, D. A.; Belford, M.; Dunyach, J. J.; Purves, R. W. Characterization of a Temperature-Controlled FAIMS System. *J. Am. Soc. Mass Spectrom.* **2007**, *18*, 1653-1663.
6. Shvartsburg, A. A.; Ibrahim, Y. M.; Smith, R. D. Differential Ion Mobility Separations in Up to 100% Helium using Microchips. *J. Am. Soc. Mass Spectrom.* **2014**, *25*, 480-489.
7. Guo, D.; Wang, Y.; Li, L.; Wang, X.; Luo, J. Precise Determination of Nonlinear Function of Ion Mobility for Explosives and Drugs at High Electric Fields for Microchip FAIMS. *J. Mass Spectrom.* **2015**, *50*, 198-205.
8. Fenn, J. B.; Mann, M.; Meng, C. K.; Wong, S. F.; Whitehouse, C. M. Electrospray Ionization for Mass Spectrometry of Large Biomolecules. *Science*. **1989**, *246*, 64-71.
9. Emmett, M. R.; Caprioli, R. Micro-Electrospray Mass Spectrometry: Ultra-High-Sensitivity Analysis of Peptides and Proteins. *J. Am. Soc. Mass Spectrom.* **1994**, *5*, 605-613.
10. Körner, R.; Wilm, M.; Morand, K.; Schubert, M.; Mann, M. Nano Electrospray Combined with a Quadrupole Ion Trap for the Analysis of Peptides and Protein Digests. *J. Am. Soc. Mass Spectrom.* **1996**, *7*, 150-156.
11. Glush, G. L.; Vachet, R. W. The Basics of Mass Spectrometry in the Twenty-First Century. *Nat. Rev. Drug Discov.* **2003**, *2*, 140-150.

12. Gabelica, V.; De Pauw, E. Internal Energy and Fragmentation of Ions Produced in Electrospray Sources. *Mass Spec. Rev.* **2005**, *24*, 566-587.
13. Patriksson, A.; Marklund, E.; van der Spoel, D. Protein Structures Under Electrospray Conditions. *Biochemistry.* **2007**, *46*, 933-945.
14. Wilm, M.; Mann, M. Analytical Properties of the Nanoelectrospray Ion Source. *Anal. Chem.* **1996**, *68*, 1-8.
15. Fong, K. W. Y.; Chan, T. -. D. A Novel Nonmetallized Tip for Electrospray Mass Spectrometry at Nanoliter Flow Rate. *J. Am. Soc. Mass Spectrom.* **1999**, *10*, 72-75.
16. Bushey, J. M.; Kaplan, D. A.; Danell, R. M.; Glish, G. L. Pulsed Nano-Electrospray Ionization: Characterization of Temporal Response and Implementation with a Flared Inlet Capillary. *Instrum. Sci. Tech.* **2009**, *37*, 257-273.
17. Mann, M. Electrospray: Its Potential and Limitations as an Ionization Method for Biomolecules. *J. Mass Spectrom.* **1990**, *25*, 575-587.
18. Karas, M.; Bahr, U.; Dulcks, T. Nano-Electrospray Ionization Mass Spectrometry: Addressing Analytical Problems Beyond Routine. *Fresenius J. Anal. Chem.* **2000**, *366*, 669-676.
19. Harper, J. D.; Charipar, N. A.; Mulligan, C. C.; Zhang, X. R.; Cooks, R. G.; Ouyang, Z. Low-Temperature Plasma Probe for Ambient Desorption Ionization. *Anal. Chem.* **2008**, *80*, 9097-9104.
20. Garcia-Reyes, J.; Harper, J. D.; Salazar, G. A.; Charipar, N. A.; Zheng, O.; Cooks, R. G. Detection of Explosives and Related Compounds by Low-Temperature Plasma Ambient Ionization Mass Spectrometry. *Anal. Chem.* **2010**, *83*, 1084-1092.
21. Chowdhury, S.; Katta, V.; Chait, B. An Electrospray-Ionization Mass Spectrometer with New Features. *Rapid Commun. Mass Spectrom.* **1990**, *4*, 81-87.
22. Lin, B.; Sunner, J. Ion Transport by Viscous Gas Flow through Capillaries. *J. Am. Soc. Mass Spectrom.* **1994**, *5*, 873-885.

23. Krutchinsky, A.; Padovan, J. C.; Cohen, H.; Chait, B. Maximizing Ion Transmission from Atmospheric Pressure into the Vacuum of Mass Spectrometers with a Novel Electrospray Interface. *J. Am. Soc. Mass Spectrom.* **2015**, 26, 649-658.
24. Liou, C.; Brodbelt, J. S. Determination of Orders of Relative Alkali Metal Ion Affinities of Crown Ethers and Acyclic Analogs by the Kinetic Method. *J. Am. Soc. Mass Spectrom.* **1992**, 3, 543-548.



## **Chapter 4: Characterization of Variables Affecting Internal Energy Deposition inside a Differential Ion Mobility Spectrometer**

### **4.1 Internal Energy Deposition during Ion Mobility Spectrometry**

Ion mobility separations are a group of techniques that can be implemented post-ionization to separate ions based on structural differences; however, the ability of these separation techniques to fully retain the structural attributes of ions has been the subject of much investigation. A majority of the studies examining the preservation of structure have attempted to either minimize the amount of internal energy deposited into ions or study the change in effective temperature of the ion [1-5]. As with other ion mobility separation techniques, the ability of DIMS separations to retain the structural characteristics of analytes has been of concern. For DIMS separations, this potential loss of ion structure originates from the fact that the separations take place at atmospheric pressures in DIMS devices, and therefore the ions undergo repeated collisions with the DIMS carrier gas [6-8]. The acceleration of the ions due to the dispersion field causes these collisions with the carrier gas to increase the internal energy of the ion. The ion velocity and the gas number density, along with the carrier gas temperature and identity, affect the ion-molecule interactions that take place within the DIMS device and ultimately determine the amount of internal energy deposited into the ion during transit through the device [9-11]. The extent of the collisional heating has been studied using various approaches, including attempts to determine the effective temperature of the ions experimentally and comparisons to heating in DT-IMS instruments [2,3,12,13]. Previously reported work has

also shown that collisions in a DIMS device can impart enough internal energy to cause isomerization of multiply charged protein ions, or the fragmentation of proton bound dimer and ions formed from small molecules resulting in the detection of fragment ions [2,3,10-16].

A schematic representation of this intra-DIMS fragmentation is shown in Figure 4.1, where a triply charged ion enters the DIMS device while an  $E_C$  of 150 V/cm is applied to the DIMS device. The  $E_C$  does not sufficiently compensate for the trajectory of the triply charged ion and after some number of dispersion field waveform cycles the ion collides with an electrode and is neutralized. This is representative of an ion without sufficient internal energy to undergo fragmentation in the DIMS device. An  $E_C$  of 150 V/cm does correct for the trajectory of the doubly charged ion shown in Figure 4.1b, which is formed prior to entering the DIMS device. In Figure 4.1c the internal energy of the triply charged ion is increased enough in DIMS that fragmentation can occur before the ion is neutralized. In Figure 4.1c the triply charged ion fragments into a doubly charged ion and a singly charged ion. The newly formed species will then travel through the DIMS device based on their own differential ion mobility and be detected at the characteristic  $E_C$  that permits them to stably move through the DIMS device and into the mass spectrometer. This characteristic  $E_C$  is the same  $E_C$  that passes the ion through the DIMS device and into the mass spectrometer when the ion is formed prior to entering DIMS. This is shown in Figures 4.1b and 4.1c, where a compensation field of 150 V/cm corrects for the trajectory of the doubly charged ion formed prior to DIMS and the double charge ion formed in DIMS. An alternative example might have the charge retained entirely by one fragment ion, with a neutral fragment traveling through the DIMS device carried by the gas flow and unaffected by the dispersion field. It should be noted that the signal detected for each of the fragment ions is not

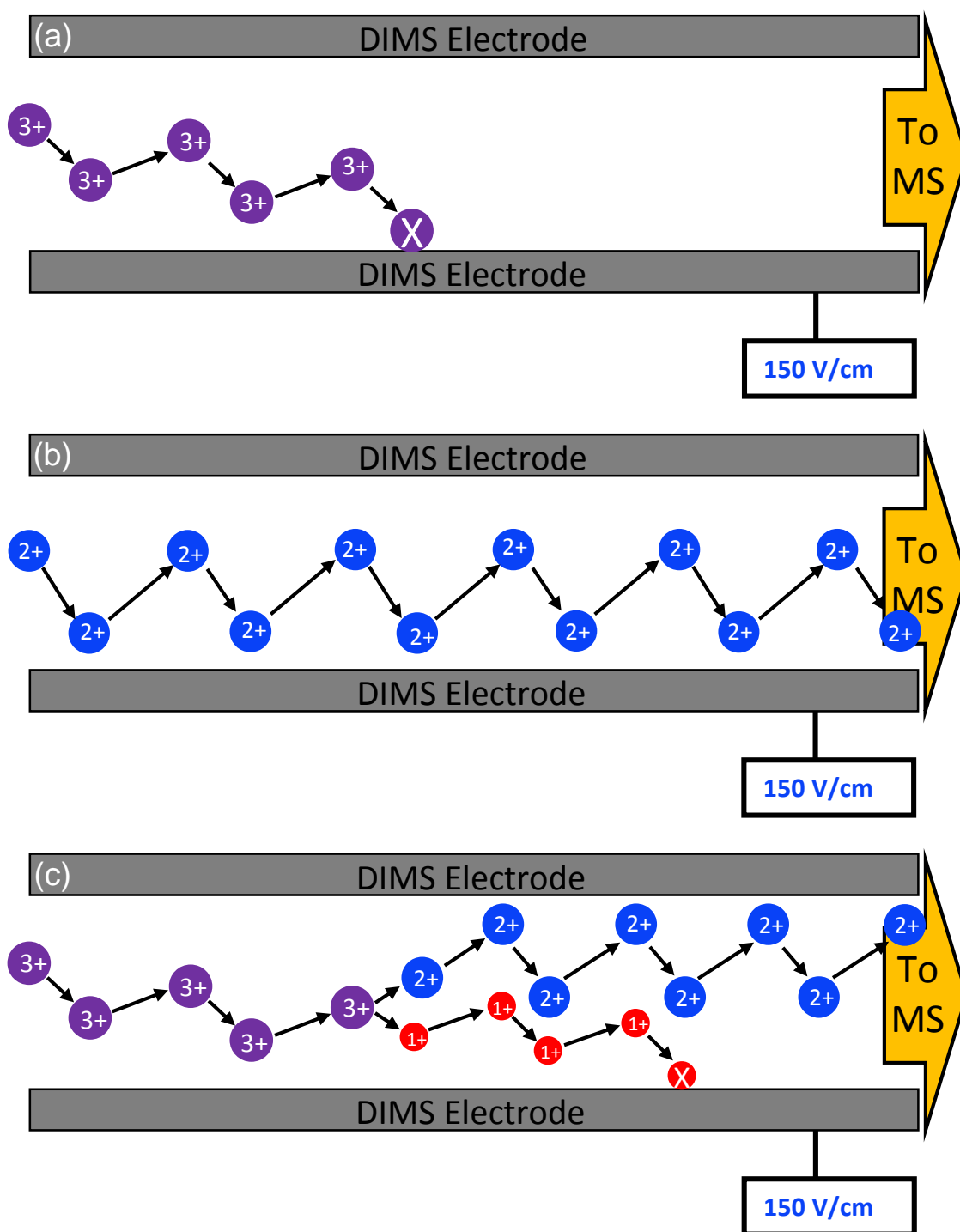


**Figure 4.1. (a) A compensation field of 150 V/cm does not correct for the trajectory of the triply charged ion and it is neutralized (b) A compensation field of 150 V/cm does correct for the trajectory of the doubly charged ion (c) The triply charge ion undergoes intra-DIMS fragmentation, and the doubly charged fragment ion stably passes through DIMS**

solely based on the amount of fragment formed. Other factors including the diffusion characteristics of the fragment ion, the mobility of the fragment ion in low and high fields, and the difference between the characteristic  $E_C$  of the parent ion and the fragment ion all affect the signal detected.

Within the reports of intra-DIMS fragmentation to this point there has been no discussion on the intra-DIMS fragmentation of larger ions such as peptides. The fragmentation of these larger ions would not be expected because of the redistribution of internal energy among the greater degrees of freedom within the ion. This redistribution would lessen the likelihood that a sufficient amount of energy would be deposited into one of the ion's covalent bonds for it to be broken. Despite this expectation, the intra-DIMS fragmentation of both bradykinin (RPPGFSPFR) and GLISH peptide ions was observed using the DIMS device coupled to the Bruker HCT mass spectrometer, and the characterization of the internal energy deposition that caused this fragmentation is discussed herein.

#### **4.2 Intra-DIMS Fragmentation of Peptides**

During DIMS analyses of bradykinin, it was observed that the signal intensity for the  $[M+3H]^{3+}$  ( $m/z$  354) ion decreased more much rapidly as a function of  $E_D$  than that of the  $[M+2H]^{2+}$  ( $m/z$  531) ion. This data is depicted in Figure 4.2. A decrease in signal as  $E_D$  is increased is expected as the effective analytical gap is narrowed and ions become more likely to strike an electrode and be neutralized; [17] however, the more rapid fall off in signal intensity above  $E_D = 29.2$  kV/cm for the  $[M+3H]^{3+}$  ions compared to that of the  $[M+2H]^{2+}$  ions was interesting. Though not unprecedented because of differences in charge and possibly conformation, this behavior was further investigated to better understand how  $E_D$  might affect ion transmission through the DIMS device. It was observed that as the signal intensity for the

$[M+3H]^{3+}$  ions decreased sharply as a function of  $E_D$ , peaks corresponding to other mass-to-charge ratios increased in signal intensity as a function of  $E_D$ .

The most prominent of the peaks observed to increase in intensity as a function of  $E_D$  during the analysis of bradykinin ions corresponds to ions of  $m/z$  348, the signal intensity of which is also

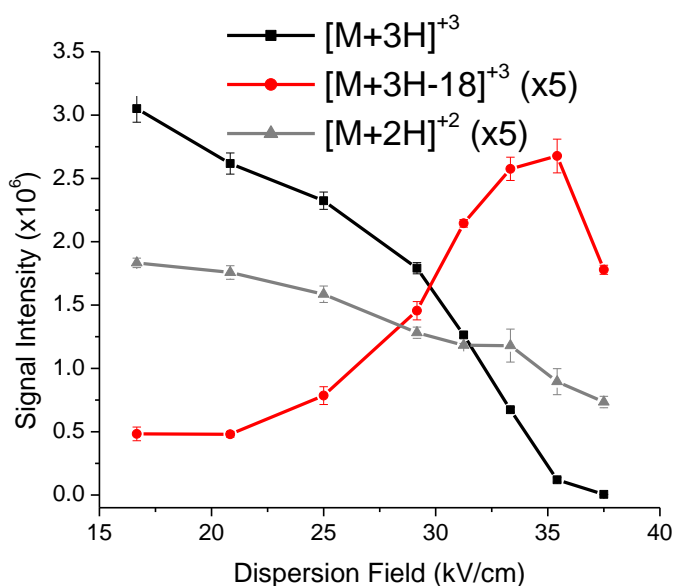


**Figure 4.2. Plot of signal intensity versus the  $E_D$  applied for bradykinin and a bradykinin fragment ion**

shown in Figure 4.2. It should be noted from this figure that at all  $E_D$  some ions of  $m/z$  348 are detected; however, at the lower  $E_D$  shown these ions are due to the fragmentation of  $[M+3H]^{3+}$  ions within the ion optics of the mass spectrometer and are detected at the same  $E_C$  as the  $[M+3H]^{3+}$  ions. An example  $E_C$  scan at  $E_D = 20.8$  kV/cm is shown in Figure 4.3a, including traces of the signal intensity for the mass-to-charge ratio of both the  $[M+3H]^{3+}$  ion and the fragment ion. The fragment ions are detected at the same  $E_C$  as the parent ions because the ions travel through the DIMS device as the parent and fragmentation takes place after the device in the mass spectrometer ion optics. As the  $E_D$  is raised and signal increases for  $m/z$  348, the characteristic  $E_C$  for the peak detected for  $m/z$  348 shifts to a value slightly higher than that of the  $[M+3H]^{3+}$  ions. This small shift in  $E_C$  is shown in Figure 4.3b. The corresponding decrease in signal intensity for the  $[M+3H]^{3+}$  ions and increase in signal intensity for the ions of  $m/z$  348, along with the close proximity in terms of both mass-to-charge ratio and differential ion mobility

suggested that ions of  $m/z$  348 were related to the  $[M+3H]^{3+}$  ions. To further substantiate the relation CID was performed on the  $[M+3H]^{3+}$  ions, and the resulting MS/MS mass spectrum is shown in Figure 4.4. It is believed that although significantly higher voltages are used in DIMS than during collisional activation in an ion trap, the higher pressures in DIMS devices shorten the mean free path such that the acceleration between collisions is limited. This causes the internal energy gained per collision to be small and for the heating to be similar to that which occurs during resonant excitation in an ion trap. The net result of this is that fragmentation proceeds via the lowest energy pathway.

During both CID and intra-DIMS fragmentation of the  $[M+3H]^{3+}$  ions of bradykinin the primary fragment ion observed was of  $m/z$  348, which is formed via a loss of neutral water. In both experiments peaks were also observed for ions of  $m/z$  322 ( $b_6^{2+}$ ), 419 ( $y_3^+$ ), 506 ( $y_4^+$ ), and 555 ( $b_5^+$ ). The intensity of the peaks for the ions formed via these less favorable pathways was increased in  $E_C$  scans at higher  $E_D$ ;

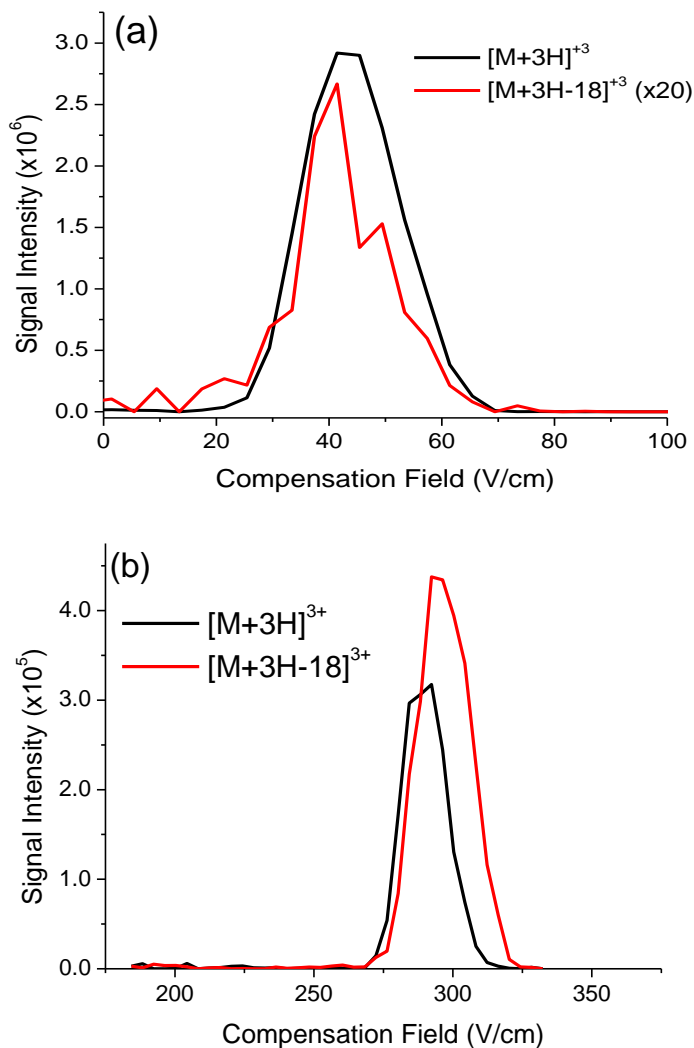


**Figure 4.3.  $E_C$  scans with (a)  $E_D = 20.8$  kV/cm and (b)  $E_D = 33.3$  kV/cm. Traces for the  $[M+3H]^{3+}$  ion of bradykinin and the  $[M+3H-18]^{3+}$  ion formed via fragmentation are shown**

however, the dissimilarities between the differential ion mobility of the fragment and parent ions have the potential to cause significant disparities in ion transmission. These differences in ion transmission would complicate the comparison of signal intensities. In general, the

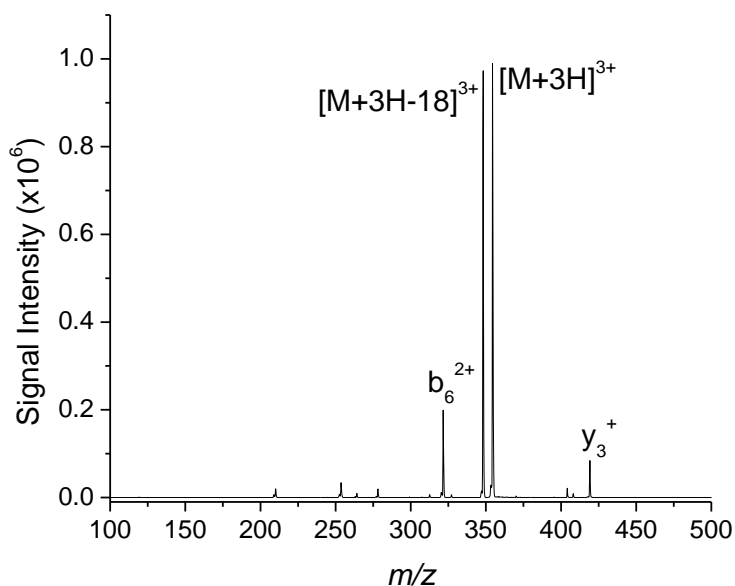


**Figure 4.4. CID MS/MS spectrum of bradykinin  $[M+3H]^{3+}$  ions**

greater the change in differential ion mobility between the fragment ion and parent ion the lower ion transmission would be expected to be for the fragment ion. During the intra-DIMS fragmentation of the  $[M+3H]^{3+}$  ions via the neutral loss of water the ions detected retain all three charges and are expected to have a similar structure to the  $[M+3H]^{3+}$  ions. As a result the  $[M+3H]^{3+}$  ions and the water loss fragment ions have similar differential ion mobilities, with their characteristic  $E_C$  separated by only  $6.0 \pm 0.7$  V/cm at an  $E_D$  of 33.3 kV/cm. Thus, it is expected that ion transmission for the  $[M+3H]^{3+}$  ions and the ions formed by the intra-DIMS loss of water would be similar, and signal intensities could be compared without attempting to correct for ion transmission.

A similar intra-DIMS fragmentation phenomenon is observed with the peptide GLISH, wherein  $y_3^+$  ions formed by intra-DIMS fragmentation passed through the DIMS device at an  $E_C$  just slightly shifted from that of  $[M+H]^+$ . An example of the  $E_C$  scans taken is shown in Figure 4.5a and the increase in  $y_3^+$  signal intensity as a function of  $E_D$  is displayed in Figure 4.5b.

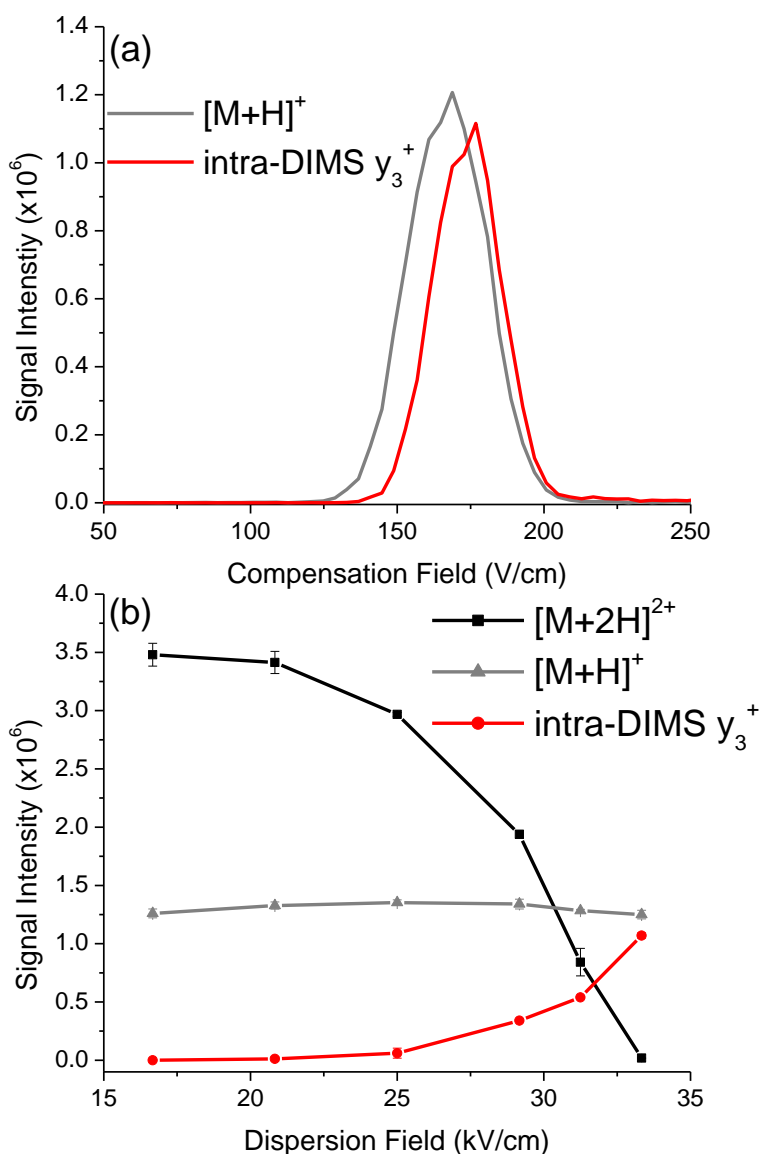


**Figure 4.5. (a) Compensation field scan performed at  $E_D = 33.3$  kV/cm (b) Plot of signal intensity versus the dispersion field applied. At an  $E_D = 16.7$  kV/cm signal from  $y_3^+$  ions formed via intra-DIMS fragmentation cannot be distinguished from that of  $y_3^+$  ions formed by the fragmentation of  $[M+2H]^{2+}$  ions in the mass spectrometer ion optics. The signal intensity for  $y_3^+$  formed via intra-DIMS fragmentation was assumed to be zero at this  $E_D$**

The close proximity in terms of  $E_C$  for the  $[M+H]^+$  ion and the  $y_3^+$  ion formed by intra-DIMS fragmentation lead to the belief that  $[M+H]^+$  ions underwent fragmentation during transit through the DIMS device. However, CID experiments performed on the  $[M+H]^+$  ions revealed that the formation of the  $b_5^+$  ion was favorable (Figure 4.6a), yet no significant peak for the  $b_5^+$  ion was observed to appear as a function of  $E_D$  in  $E_C$  scans. Alternatively, in Figure 4.6b it is shown that the most prominent product from CID of the  $[M+2H]^{2+}$  ion is the  $y_3^+$  ion. The CID spectra of the  $[M+H]^+$  and  $[M+2H]^{2+}$  ions of GLISH,



combined with the similar fragmentation patterns observed for CID and intra-DIMS

fragmentation of the  $[M+3H]^{3+}$  ions of bradykinin, allow for the conclusion that the  $y_3^+$  formed via intra-DIMS fragmentation originate from  $[M+2H]^{2+}$  ions of GLISH rather than  $[M+H]^+$  ions.

The  $y_3^+$  ion is presumably detected at an  $E_C$  closer to that of the  $[M+H]^+$  ion of GLISH than the  $[M+2H]^{2+}$  ion, as shown in Figure 4.7, because of the role charge state plays in determining the

differential mobility of an ion.

It is also worth noting that for both bradykinin and GLISH only the more highly charged peptide species undergo intra-DIMS fragmentation. Neither the  $[M+2H]^{2+}$  ions of bradykinin nor the  $[M+H]^+$  ions of GLISH was observed to fragment during transit through the DIMS device. This is particularly interesting for the  $[M+2H]^{2+}$  and  $[M+3H]^{3+}$  ions of

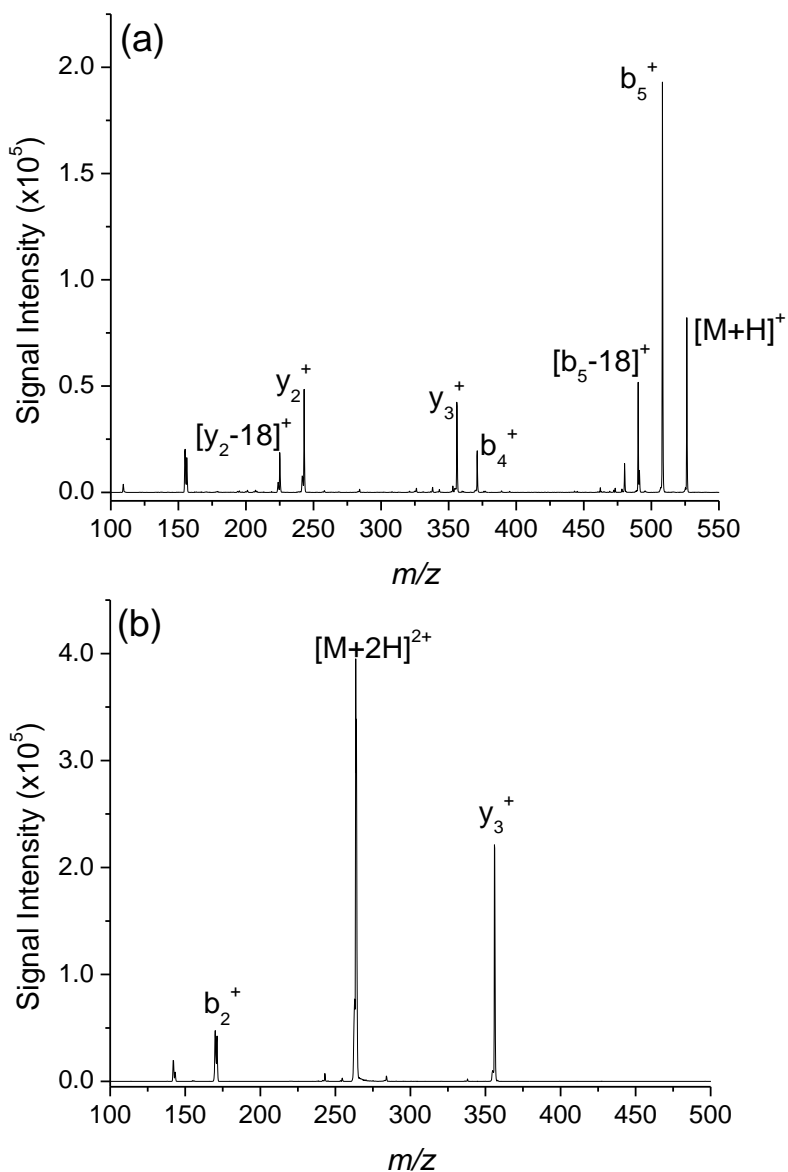


**Figure 4.6.** CID MS/MS spectrum of (a) GLISH  $[M+H]^+$  ions and (b) GLISH  $[M+2H]^{2+}$  ions

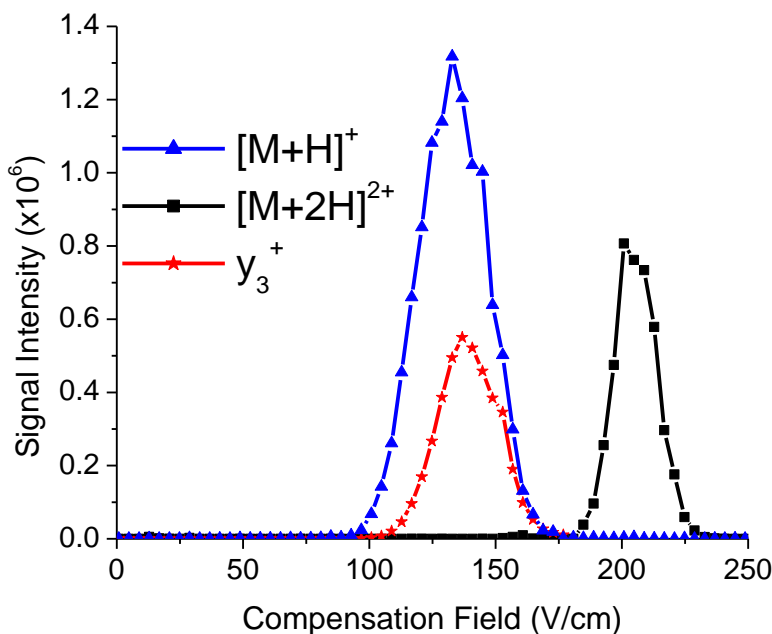


**Figure 4.7. Compensation field scan of GLISH ions with  $E_D = 33.3$  kV/cm**

bradykinin as they have nearly identical critical energies for the lowest energy dissociations [18]. That no fragmentation occurs for the  $[M+2H]^{2+}$  ions despite such similar internal energies being required for dissociation highlights the greater acceleration experienced by

the higher charge state ions as a critical factor for the addition of internal energy.

#### 4.2.1. Effect of Temperature on Fragmentation

To further interrogate the intra-DIMS fragmentation of bradykinin  $[M+3H]^{3+}$  ions the temperature setting of the instrument desolvation gas, and therefore the DIMS carrier gas, was varied. The principle of this work was based on studies where elevating the bath gas temperature during CID in a quadrupole ion trap was shown to increase the initial internal energy of the ions prior to collisional activation and facilitate fragmentation [19]. In the current work, the ions are thermalized with the carrier gas and therefore the temperature of the carrier gas determines the initial internal energy of the ions. This gives the internal energy of the bradykinin ions to initially be 14.24, 15.87, and 16.72 eV at carrier gas temperatures of 91.7, 133.4, and 155.8 °C, respectively, using

$$U = U_T + U_R + U_V \quad (4.1)$$

where  $U$  is the total internal energy of the ion,  $U_T$  is the amount of internal energy supplied by translational motion,  $U_R$  is the internal energy added by rotational energy, and  $U_V$  is the by vibrational contribution to internal energy.

Based on these internal energy calculations, as the temperature of the carrier gas is increased less internal energy would need to be added via collisional heating for the ions to reach the internal energy required for intra-DIMS fragmentation to occur. This effect is shown in Figure 4.8a where the fragmentation efficiency of the  $[M+3H-18]^{3+}$  ion is calculated according to Equation 4.2.

$$\text{Fragmentation Efficiency} = \frac{\text{Signal Intensity Fragment}}{\text{Signal Intensity (Fragment+Parent)}} \quad (4.2)$$

As the temperature of the carrier gas is increased lower dispersion field strengths are required for the appearance of  $[M+3H-18]^{3+}$  ions to take place. Fitting the values shown in Figure 4.8a obtained at carrier gas temperatures of 133.4 and 155.8 °C with sigmoidal curves, it can be determined that the 0.85 eV difference in initial internal energy requires an  $E_D$  3.3 kV higher for the ions to reach an internal energy where the fragmentation efficiency of the  $[M+3H-18]^{3+}$  ions is 50%. Using Origin to extrapolate the data measured at 91.7 °C the plot shown in Figure 4.8b can be generated. This shows a linear relationship between the initial internal energy of the  $[M+3H]^{3+}$  ions and the  $E_D$  at which fragmentation efficiency reaches 50%.

The experiment was also completed using the  $[M+2H]^{2+}$  ions of GLISH, which were calculated to have internal energies of 7.26, 8.09, and 8.53 eV at carrier gas temperatures of 91.7, 133.4, and 155.8 °C, respectively. The data for the  $y_3^+$  fragment ion from GLISH  $[M+2H]^{2+}$  is shown in Figure 4.9a. Here again the ions with the higher initial internal energies required that

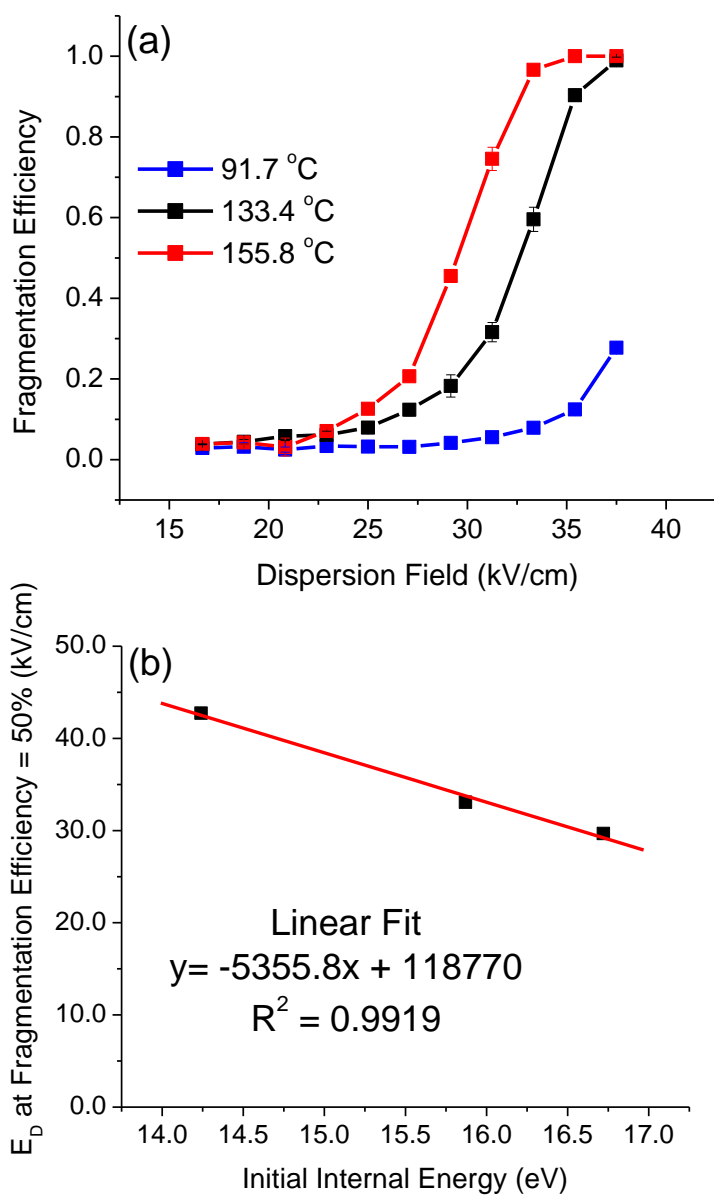


**Figure 4.8. (a) Plot of how carrier gas temperature affects the  $E_D$  at which the  $[M+3H]^{3+}$  ions of bradykinin fragment (b) Plot of the  $E_D$  where a 50% fragmentation efficiency for the bradykinin  $[M+3H]^{3+}$  ions is reached versus the initial internal energy of the bradykinin  $[M+3H]^{3+}$  ions**

less internal energy be added by collisional heating for intra-DIMS fragmentation to occur and the fragment ion is detected at lower  $E_D$ . Fitting the data in Figure 4.9a with sigmoidal curves yields the  $E_D$  at which the fragmentation efficiency of the  $[M+2H]^{2+}$  ions reaches 50%. These values are plotted in Figure 4.9b versus the initial internal energy of the  $[M+2H]^{2+}$  ions.

As with bradykinin, the relationship was found to be linear. Thus, the difference in  $E_D$  where the fragmentation efficiency of the parent ions reaches 50% can be converted to a difference in the amount of internal energy gained during

transit through the DIMS device. A comparison of the slopes in Figure 4.8b and Figure 4.9b shows that as  $E_D$  is increased the effect on the internal energy of the  $[M+3H]^{3+}$  ions of

bradykinin is greater than that on the  $[M+2H]^{2+}$  ions of GLISH. In other words, each V/cm increase in  $E_D$  increases the internal energy of the ions more for the  $[M+3H]^{3+}$  ions of bradykinin. Although bradykinin has significantly more degrees of freedom over which to spread the energy, the higher charge state of the ion could account for this greater internal energy increase as  $E_D$  is increased.

Changing the temperature of the DIMS carrier gas to manipulate the internal energy of ions during an analysis by DIMS must be used in balance with achieving the separation required. Decreasing the carrier gas/ion temperature could be valuable for compounds with low isomerization/fragmentation barriers, at the risk of limiting separation abilities. Changes to the temperature of the DIMS carrier gas alter the number density ( $N$ ) within DIMS, and because ion mobilities are

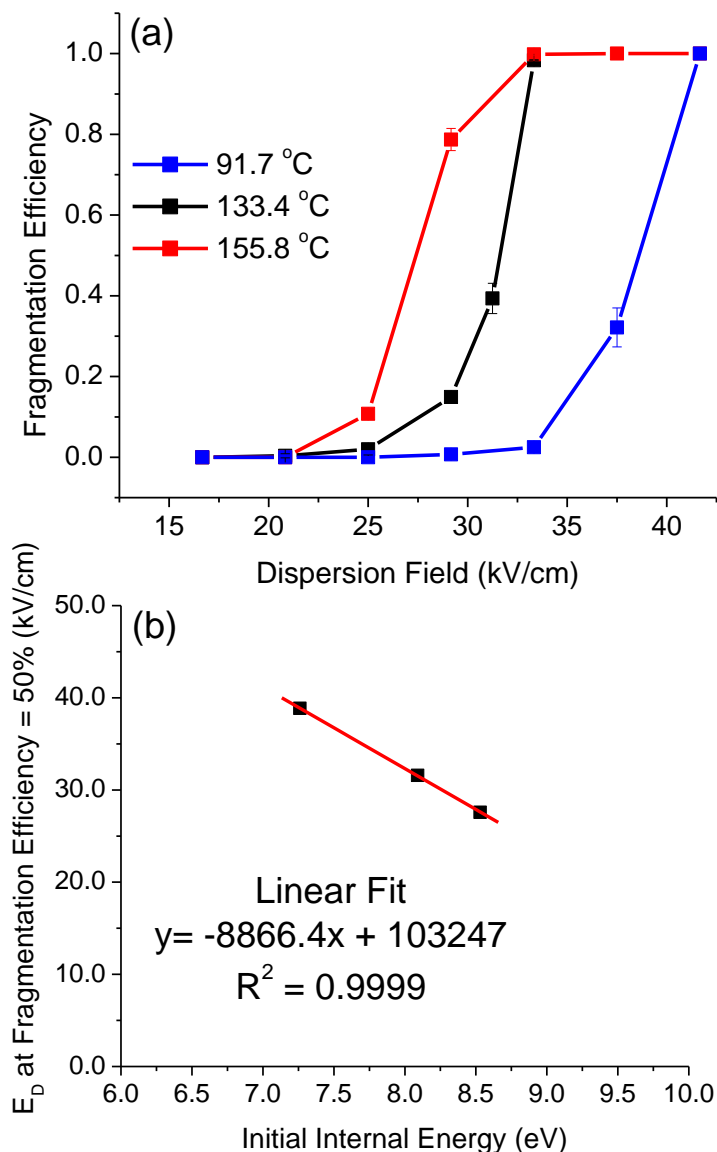


**Figure 4.9. (a) Plot of how carrier gas temperature affects the  $E_D$  at which the  $[M+2H]^{2+}$  ions of GLISH fragment (b) Plot of the  $E_D$  where a 50% fragmentation efficiency for the GLISH  $[M+2H]^{2+}$  ions is reached versus the initial internal energy of the GLISH  $[M+2H]^{2+}$  ions**

dependent on E/N, varying temperature modifies the separation characteristics [20,21]. For the ions formed by the water loss from the  $[M+3H]^{3+}$  ions used in this work, the overall separation ability was observed to be directly related to temperature of the DIMS carrier gas.

The characteristic  $E_C$  and width of the peaks are shown in Figure 4.10 for all temperature and  $E_D$  settings used. It was observed that hotter DIMS carrier gas settings lead to higher  $E_C$ , and thus the potential separation power of DIMS for these ions is highest at the same settings that facilitate fragmentation. This improvement in separation ability at higher carrier gas temperatures applies to all peptide ions examined by DIMS, as they have exhibited differential mobilities that increase as E/N is raised [2]. Therefore increasing the temperature of the carrier gas will increase the characteristic  $E_C$  of peptide ions and improve the separation ability of the DIMS device for these species, but also increase the likelihood of intra-DIMS fragmentation. Hence, the potential tradeoff between separation capability and the retention of structural information must be considered based on the experimental circumstances.

#### 4.2.2. Effect of Carrier Gas Composition on Fragmentation

Another method that has been previously shown to change the amount of internal energy deposited into ions during DIMS analyses is to vary the composition of the carrier gas using non-polar gases [4,12]. The change in internal energy of an ion due to collisional heating in a DIMS device, measured as the change in the temperature of the ion ( $\Delta T$ ), has been shown to depend on the inverse square of the collisional cross section ( $\Omega$ ) by

$$\Delta T = \frac{3\pi}{128k_B^2T} \left(1 + \frac{M}{m}\right) \left(\frac{zeE}{N\Omega}\right)^2 \quad (4.3)$$

where  $k_B$  is the Boltzmann constant,  $T$  is the temperature of the carrier gas,  $M$  is the mass of the carrier gas,  $m$  is the mass of the ion,  $z$  is the ion charge state,  $e$  is elementary charge,  $E$  is the electric field strength, and  $N$  is the number density of the gas [4,21]. Thus, implementing carrier gases other than nitrogen would affect the amount of internal energy deposited. The effect on

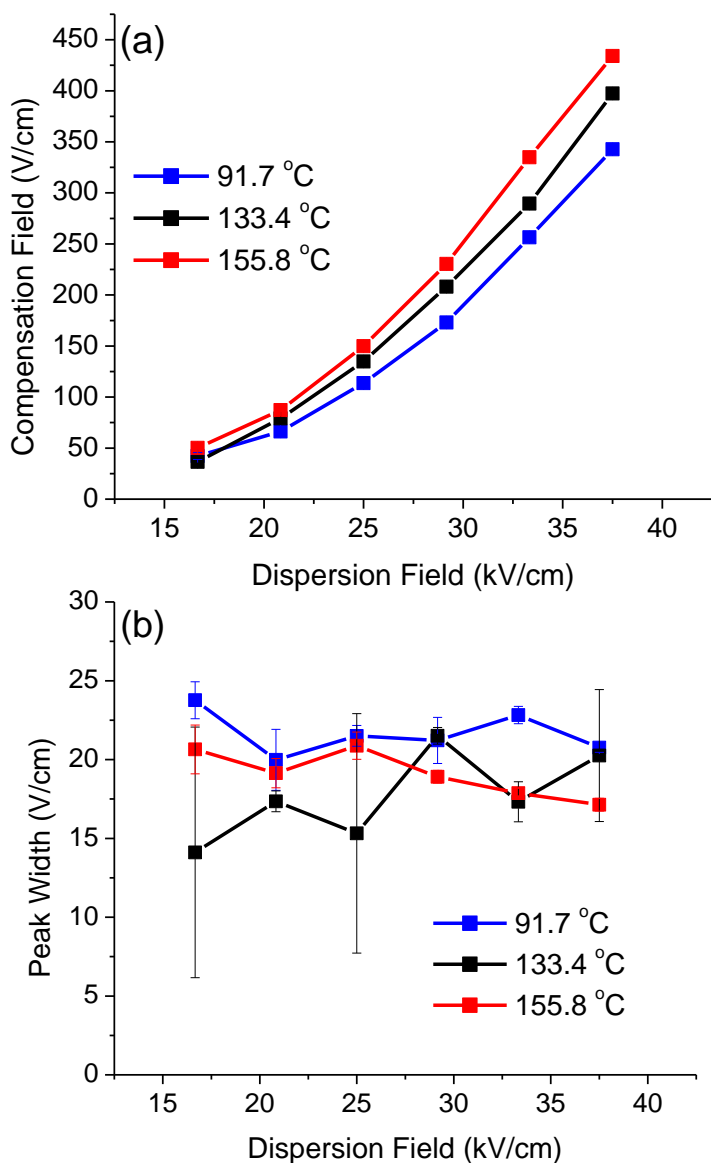


**Figure 4.10. (a) Plot showing the effect of carrier gas temperature on the relationship between  $E_D$  and the characteristic  $E_C$  of the  $[M+3H-18]^{3+}$  fragment ion of bradykinin (b) Plot showing the effect of carrier gas temperature the peak width of the  $[M+3H-18]^{3+}$  fragment ion of bradykinin**

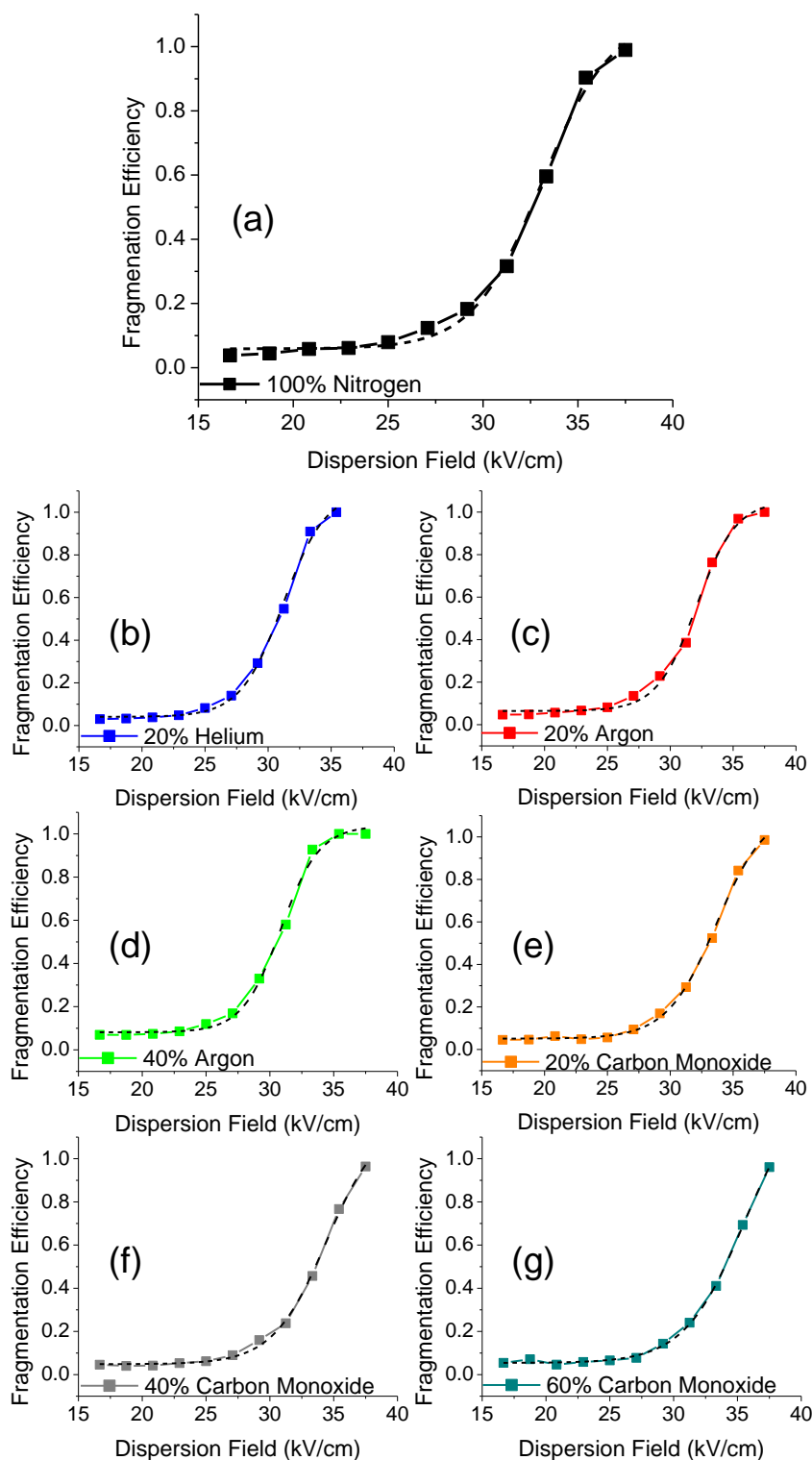
intra-DIMS fragmentation of changing the carrier gas composition to be a mixture of nitrogen with either helium, argon, or carbon monoxide is shown in Figure 4.11. Similar to the Figure 4.8a and 4.9a, Figure 4.11 plots fragmentation efficiency of the bradykinin  $[M+3H]^{3+}$  ion versus the applied  $E_D$ . Although the differences are difficult to observe using Figure 4.11, plotting the derivative of the sigmoidal fits to the data as done in Figure 4.12 more clearly shows differences in the relationship between  $E_D$  and intra-DIMS fragmentation

with different carrier gas compositions.

Though Figure 4.12 shows these changes in a qualitative way, the data obtained during experiments varying the carrier gas temperature allows for a more quantitative approach to comparing internal energy deposition by a nitrogen carrier gas versus a gas mixture. Comparing Figures 4.11a and 4.11b, which were obtained using a 100% nitrogen carrier gas and a 20% helium / 80% nitrogen mixture, respectively, shows that the  $E_D$  needed for intra-DIMS fragmentation to occur when helium is added to the carrier gas is significantly lower. When the DIMS carrier gas is 20% helium the  $E_D$  where 50% fragmentation efficiency is reached is 1.9 kV/cm lower compared to a 100% nitrogen carrier gas. Based on the relationship shown in Figure 4.8a, a decrease of 1.9 kV/cm in the  $E_D$  where fragmentation efficiency reaches 50% is equivalent to an increase in internal energy of 0.35 eV. However, the ions also start with lower internal energies when 20% helium is used because of the difference in heat transfer between the carrier gases. The amount of internal energy gained by the ions in a 20% helium carrier gas compared to a 100% nitrogen carrier gas must also include the 0.29 eV difference in initial internal energy. Therefore at the  $E_D$  where fragmentation efficiency reaches 50% when 20% helium is used ( $E_D = 31.2$  kV/cm), the DIMS carrier gas including helium has added 0.64 eV more internal energy to the ions.

Similar to the addition of helium to the carrier gas, the use of 20 and 40% argon (Figures 4.11c and 4.11d, respectively) resulted in more internal energy deposition into the bradykinin  $[M+3H]^{3+}$  ions than a 100% nitrogen carrier gas. Use of 20% argon causes the  $E_D$  where a 50% fragmentation efficiency is reached to be 1.0 kV/cm lower than when a 100% nitrogen carrier gas is used. That 1.0 kV/cm difference is the equivalent of the ions being 0.19 eV higher in internal energy. As with helium, carrier gas mixtures including argon are cooler than when 100%





**D**

**Figure 4.11. Plot of fragmentation efficiency versus  $E_D$  applied with (a) 100% Nitrogen, (b) 20% Helium, (c) 20% Argon, (d) 40% Argon, (e) 20% Carbon Monoxide, (f) 40% Carbon Monoxide, and (g) 60% Carbon Monoxide carrier gas compositions. Plots shown in solid lines with sigmoidal fits shown in dashes**

nitrogen is used. Therefore, the difference in initial internal energy must be included to determine how much more internal energy has been added by the carrier gas including argon. Thus, the 0.19 eV must be combined with the 0.09 eV difference in initial internal energy, meaning that at an  $E_D = 32.1$  kV/cm the carrier gas including 20% argon has increased the internal energy of the ions 0.28 eV more than the 100% nitrogen carrier gas. The use of 40% argon in the carrier gas lowers the  $E_D$  required for a fragmentation efficiency of 50% by 2.2 kV/cm, equating to the ions having an internal energy 0.41 eV higher. The 40% argon carrier gas is also significantly cooler than the 100% nitrogen carrier gas, and the initial internal energy of the ions is 0.20 eV lower. Based on these values, at an  $E_D$  of 30.9 kV/cm the use of 40% argon carrier gas has raised the internal energy of the ion 0.61 eV more than when 100% nitrogen is

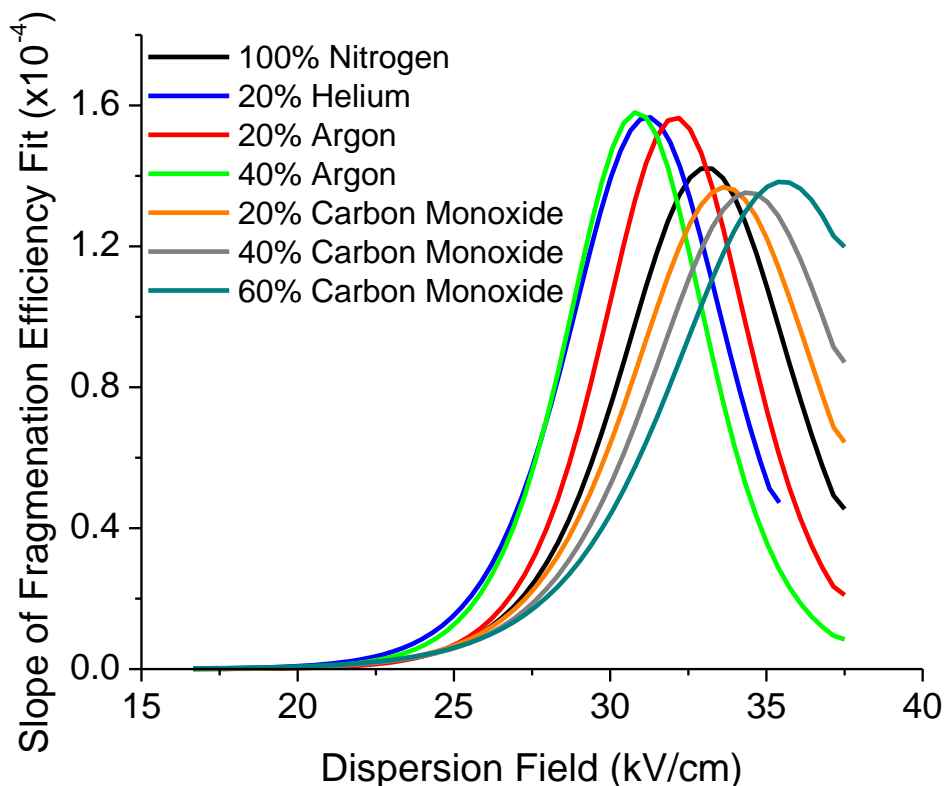


**Figure 4.12.** Plot of the slope of the sigmoidal curves fit to the data in Figure 4.11 versus the  $E_D$  applied

used. Had the temperature difference between the gas mixtures and 100% nitrogen not been present, the more efficient internal energy deposition that occurs when helium and argon are used would have caused fragmentation at even lower  $E_D$ .

Also worth noting is the fact that 20% helium and 40% argon compositions cause fragmentation at nearly the same  $E_D$ . This highlights the importance of collisional cross section on the change in internal energy as ions pass through a DIMS device. Although argon has a mass nearly ten times that of helium, which increases the maximum amount of center of mass collision energy available by a factor of almost ten, the heavier argon atoms increase the internal energy of the ions less than the lighter helium atoms. This is believed to occur because argon has a greater collisional cross section with the ions [22]. This results in more frequent collisions and thus less acceleration between collisions, leading to lower collision energies. Interestingly, this is contrary to what is observed using gases other than helium as the collision gas in an ion trap, where heavier gases cause more fragmentation than helium [23,24]. This can be rationalized based on the collision frequency, which is much lower in the ion trap and thus significant acceleration can occur between collisions. Because of the higher kinetic energy of the ions in the ion trap the collision cross sections will be smaller and there will be smaller differences in collision cross section between gases. This results in the collision gas mass, and therefore the available center of mass collision energy, being the dominant variable for the addition of internal energy in an ion trap.

Changing the carrier gas composition can also lower the amount of internal energy added as an ion travels through a DIMS device. Using a more polar gas such as carbon monoxide increases collisional cross-section and the internal energy deposition can be lowered [25]. Gas mixtures containing 20, 40, and 60% carbon monoxide result in significantly less intra-DIMS

fragmentation, the data for which is presented in Figure 4.11 e-g. A plot of the percentage of carbon monoxide present in the carrier gas versus the  $E_D$  at which the fragmentation efficiency of the  $[M+3H]^{3+}$  ions of bradykinin reaches 50% yields the linear relationship shown in Figure 4.13. The positive correlation shown in this plot is counter to the expected relationship for internal energy deposition in DIMS previously described using the two temperature theorem [13]. Based on that work carbon monoxide and nitrogen should increase the internal energy of the ions equally due to their equivalent masses and therefore the line in Figure 4.13 would be flat; however, the current works suggests that collisional cross-section also plays a role in the internal energy deposition process.

The same calculations that were completed for helium and argon carrier gas mixtures to describe the difference in internal energy added with different carrier gas compositions can be done for carrier gas mixtures using carbon monoxide. However, carrier gas mixtures including

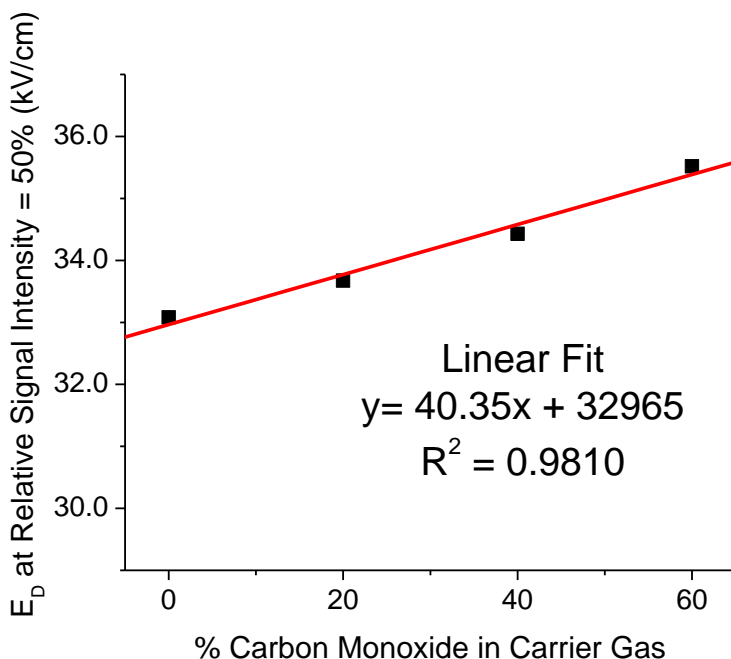


**Figure 4.13. Plot of the  $E_D$  where a 50% fragmentation efficiency for the bradykinin  $[M+3H]^{3+}$  ions is reached versus the percentage of the carrier gas that is carbon monoxide**

carbon monoxide add less internal energy compared to a 100% nitrogen carrier gas. When 20, 40, and 60% carbon monoxide mixtures are used as the DIMS carrier gas and an  $E_D = 33.1$  kV/cm is applied the internal energy of the ions are 0.12, 0.28, and 0.48 eV lower, respectively, compared to a 100% nitrogen

carrier gas. These values include the slight differences in initial internal energies based on gas temperature.

Based on the results obtained it can also be concluded that changing the composition of the carrier gas has similar implications to manipulating temperature. Whereas adding helium

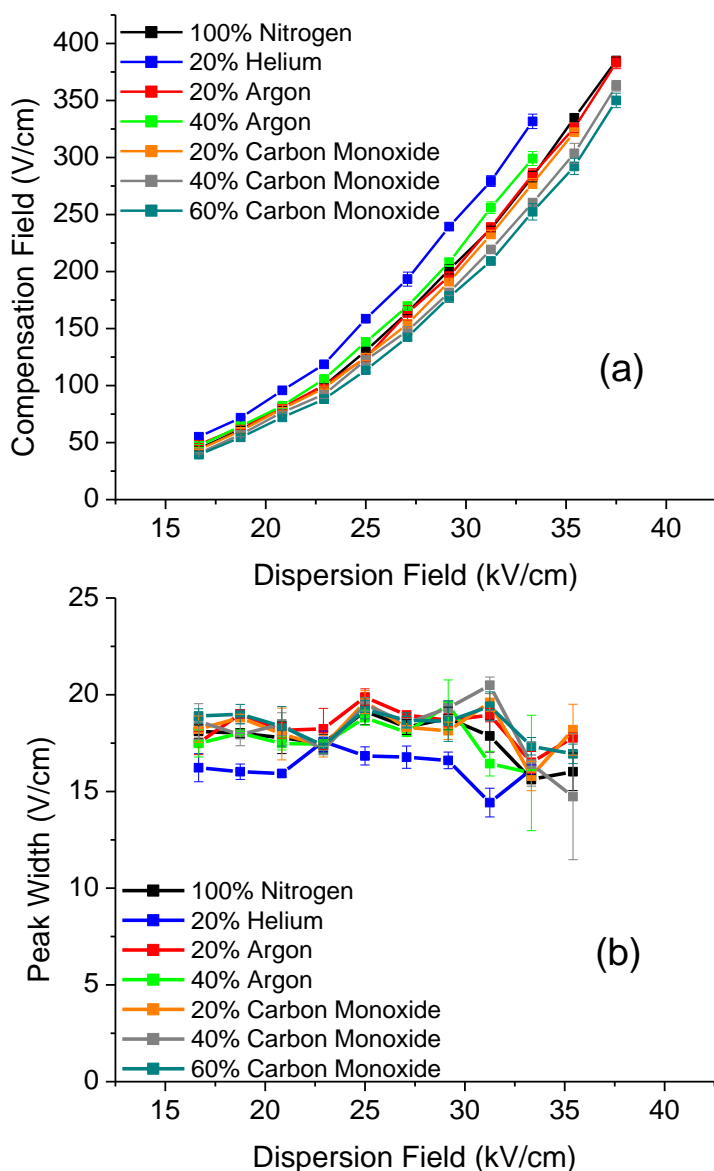


**Figure 4.14. (a) Plot showing the effect of carrier gas composition on the relationship between  $E_D$  and the characteristic  $E_C$  of bradykinin  $[M+3H]^{3+}$  ions (b) Plot showing the effect of carrier gas composition on the peak width of bradykinin  $[M+3H]^{3+}$  ions**

increases the differential mobilities of ions (data shown in Figure 4.14) and has been shown to improve separations, it also increases the amount of internal energy deposited into an ion at any  $E_D$  [4,26-28]. Furthermore, helium has a considerably lower breakdown voltage than nitrogen at the pressures and distances typically used in DIMS, placing an upper limit on the  $E_D$  that can be utilized [28,29]. The use of higher amounts of carbon monoxide reduces the amount of internal energy ions gain during their transit through a DIMS device, but also potentially reduces the separation power of

the analysis [26,27]. For the  $[M+3H]^{3+}$  ions in this work, the use of carbon monoxide lowers the characteristic  $E_C$  while peak widths remain constant (data shown in Figure 4.14). These effects will be compound specific based on the interactions of the ion and the carrier gas, but for peptides the use of carbon monoxide will lower the characteristic  $E_C$  of the ions and therefore reduce the separation ability of the DIMS device [21]. Thus, the tradeoffs must be considered based on the experimental requirements and limitations.

### 4.3 Conclusions

The intra-DIMS fragmentation of peptides has been observed, and the fragmentation patterns strongly correlate with those of CID performed in an ion trap mass spectrometer. Thus, it is believed that the collisions that occur within DIMS add energy via a slow heating process that favors fragmentation proceeding via the lowest energy pathway. The effect of varying the DIMS carrier gas temperature, and therefore the ion internal energy prior to collisional heating, was studied. The  $E_D$  at which the fragmentation efficiency of the parent ion reached 50% was found to have a linear relationship with the initial internal energy of the ions. Thus, over the  $E_D$  range studied internal energy increased in a linear fashion with the  $E_D$  applied. The internal energy deposition was also found to be more efficient for the  $[M+3H]^{3+}$  ions of bradykinin versus the  $[M+2H]^{2+}$  ions of GLISH, which is believed to occur because of the higher charge state of the bradykinin ions studied.

It was also shown that by varying the composition of the DIMS carrier gas the amount of internal energy deposited into ions could be adjusted. Gases such as helium and argon yielded greater internal energy deposition than the typically used nitrogen carrier gas, whereas the more polar carbon monoxide has a greater collisional cross section with ions and the amount of internal energy gained by the ions is lower when they pass through a DIMS device with carbon

monoxide in the carrier gas. The difference in internal energy deposited when using different carrier gas compositions compared to a 100% nitrogen carrier gas was calculated using the relationship between  $E_D$  and the internal energy of the ions determined while varying the temperature of the carrier gas. The relationship between the amount of carbon monoxide present in the carrier gas and  $E_D$  required for the fragmentation efficiency of the parent ion to reach 50% was also found to be linear with a positive correlation, meaning that collisional cross-section plays a role in the internal energy deposition process.

Thus, both varying the carrier gas temperature and altering the carrier gas composition yield the ability to tune the amount of internal energy deposited into ions during their transit through the DIMS device. However, changing the carrier gas temperature and composition were shown to alter the separation capability of the DIMS analysis for the  $[M+3H]^{3+}$  and  $[M+3H-18]^{3+}$  bradykinin ions studied. With regards to carrier gas temperature and composition, the separation capabilities of a DIMS device for peptide ions will be greatest at those conditions that most facilitate fragmentation. Based in this observation, the optimum use of the ability to vary internal energy deposition through manipulation of the carrier gas temperature and composition must be determined on a case-by-case scale.

## REFERENCES

1. Merenbloom, S. I.; Flick, T. G.; Williams, E. R. How Hot are Your Ions in TWAVE Ion Mobility Spectrometry. *J. Am. Soc. Mass Spectrom.* **2011**, *23*, 553-562.
2. Shvartsburg, A. A.; Prior, D. C.; Tang, K.; Smith, R. D. High-Resolution Differential Ion Mobility Separations using Planar Analyzers at Elevated Dispersion Fields. *Anal. Chem.* **2010**, *82*, 7649-7655.
3. Kendler, S.; Lambertus, G. R.; Dunietz, B. D.; Coy, S. L.; Nazarov, E. G.; Miller, R. A.; Sacks, R. D. Fragmentation Pathways and Mechanisms of Aromatic Compounds in Atmospheric Pressure Studied by GC-DMS and DMS-MS. *Int. J. Mass Spectrom. Ion Proc.* **2007**, *263*, 137-147.
4. Shvartsburg, A. A.; Danielson, W. F.; Smith, R. D. High-Resolution Differential Ion Mobility Separations using Helium-Rich Gases. *Anal. Chem.* **2010**, *82*, 2456-2462.
5. Chen, S.; Russell, D. H. How Closely Related are Conformations of Protein Ions Sampled by IMS-IMS to Native Solution Structures. *J. Am. Soc. Mass Spectrom.* **2015**, *26*, 1433-1443.
6. Krylov, E. V.; Nazarov, E. G.; Miller, R. A.; Tadjikov, B.; Eiceman, G. A. Field Dependence of Mobilities for Gas-Phase-Protonated Monomers and Proton-Bound Dimers of Ketones by Planar Field Asymmetric Waveform Ion Mobility Spectrometer (PFAIMS). *J. Phys. Chem. A.* **2002**, *106*, 5437-5444.
7. Shvartsburg, A. A.; Creese, A. J.; Smith, R. D.; Cooper, H. J. Separation of a Set of Peptide Sequence Isomers using Differential Ion Mobility Spectrometry. *Anal. Chem.* **2011**, *83*, 6918-6923.
8. Levin, D. S.; Vouros, P.; Miller, R. A.; Nazarov, E. G.; Morris, J. C. Characterization of Gas-Phase Molecular Interactions of Differential Mobility Ion Behavior Utilizing an Electrospray Ionization-Differential Mobility-Mass Spectrometer System. *Anal. Chem.* **2006**, *78*, 96-106.
9. Nazarov, E. G.; Coy, S. L.; Krylov, E. V.; Miller, R. A.; Eiceman, G. A. Pressure Effects in Differential Mobility Spectrometry. *Anal. Chem.* **2006**, *78*, 7697-7706.
10. An, X.; Eiceman, G. A.; Rodriguez, J. E.; Stone, J. A. Gas Phase Fragmentation of Protonated Esters in Air at Ambient Pressure through Ion Heating by Electric Field in Differential Mobility Spectrometry. *Int. J. Mass Spectrom.* **2011**, *303*, 181-190.



11. An, X.; Eiceman, G. A.; Rasanen, R.; Rodriguez, J. E.; Stone, J. A. Dissociation of Proton Bound Ketone Dimers in Asymmetric Electric Fields with Differential Mobility Spectrometry and in Uniform Electric Fields with Linear Ion Mobility Spectrometry. *J. Phys. Chem. A*. **2013**, *117*, 6389-6401.
12. Shvartsburg, A. A.; Li, F.; Tang, K.; Smith, R. D. Distortion of Ion Structures by Field Asymmetric Waveform Ion Mobility Spectrometry. *Anal. Chem.* **2007**, *79*, 1523-1528.
13. Robinson, E. W.; Shvartsburg, A. A.; Tang, K.; Smith, R. D. Control of Ion Distortion in Field Asymmetric Waveform Ion Mobility Spectrometry Via Variation of Dispersion Field and Gas Temperature. *Anal. Chem.* **2008**, *80*, 7508-7515.
14. Nazarov, E. G.; Coy, S. L.; Krylov, E. V.; Miller, R. A.; Eiceman, G. A. Pressure Effects in Differential Mobility Spectrometry. *Anal. Chem.* **2006**, *78*, 7697-7706.
15. Menlydiev, M. R.; Tarassov, A.; Kielnecker, A. M.; Eiceman, G. A. Tandem Differential Mobility Spectrometry with Ion Dissociation in Air at Ambient Pressure and Temperature. *Analyst.* **2015**, *140*, 2995-3002.
16. Veasey, C. A.; Thomas, C. Fast Quantitative Characterisation of Differential Mobility Responses. *Analyst.* **2004**, *129*, 198-204.
17. Schneider, B.; Covey, T.; Coy, S.; Krylov, E.; Nazarov, E. Chemical Effects in the Separation Process of a Differential Mobility/Mass Spectrometer System. *Anal. Chem.* **2010**, *82*, 1867-1880.
18. Butcher, D. J.; Asano, K. G.; Goeringer, D. E.; McLuckey, S. A. Thermal Dissociation of Gaseous Bradykinin Ions. *J. Phys. Chem. A*. **1999**, *103*, 8664-8671.
19. Racine, A. H.; Payne, A. H.; Remes, P. M.; Glish, G. L. Thermally Assisted Collision-Induced Dissociation in a Quadrupole Ion Trap Mass Spectrometer. *Analytical Chemistry*. **2006**, *78*, 4609-4614.
20. Krylov, E. V.; Coy, S. L.; Nazarov, E. G. Temperature Effects in Differential Mobility Spectrometry. *Int. J. Mass Spectrom.* **2009**, *279*, 119-125.
21. Shvartsburg, A. A. Differential Ion Mobility Spectrometry : Nonlinear Ion Transport and Fundamentals of FAIMS; CRC Press, Boca Raton, 2009.

22. Akridge, G. R.; Ellis, H. W.; Pai, R. Y.; McDaniel, E. W. Mobilities of  $\text{Li}^+$  Ions in He, Ne, and Argon and of  $\text{Na}^+$  in He, Ne, Ar, and  $\text{CO}_2$ . *J. Chem. Phys.* **1975**, 62, 4578-4579.
23. Doroshenko, V. M.; Cotter, R. J. Pulsed Gas Introduction for Increasing Peptide CID Efficiency in a MALDI/Quadrupole Ion Trap Mass Spectrometer. *Analytical Chemistry*. **1996**, 68, 463-472.
24. Vachet, R. W.; Glish, G. L. Effects of Heavy Gases on the Tandem Mass Spectra of Peptide Ions in the Quadrupole Ion Trap. *Journal of the American Society for Mass Spectrometry*. **1996**, 7, 1194-1202.
25. Fernandez-Maestre, R., Wu, C., Hill Jr., H. Buffer Gas Modifiers Effect Resolution in Ion Mobility Spectrometry through Selective Ion-Molecule Clustering Reactions. *Rapid. Commun. Mass Spectrom.* **2012**, 26, 2211-2223.
26. Shvartsburg, A. A.; Ibrahim, Y. M.; Smith, R. D. Differential Ion Mobility Separations in Up to 100% Helium using Microchips. *J. Am. Soc. Mass Spectrom.* **2014**, 25, 480-489.
27. Shvartsburg, A. A.; Tang, K. Q.; Smith, R. D. Differential Ion Mobility Separations of Peptides with Resolving Power Exceeding 50. *Anal. Chem.* **2010**, 82, 32-35.
28. Isenberg, S. L.; Armistead, P. M.; Glish, G. L. Optimization of Peptide Separations by Differential Ion Mobility Spectrometry. *J. Am. Soc. Mass Spectrom.* **2014**, 25, 1592-1599.
29. Friedrich, P. Ueber Die Zum Funkenübergang in Luft, Wasserstoff Und Kohlensäure Bei Verschiedenen Drucken Erforderliche Potentialdifferenz. *Annalen Der Physik*. **1889**, 273, 69-96.

## **CHAPTER 5: IMPROVED DIFFERENTIAL ION MOBILITY SPECTROMETRY SEPARATIONS USING LINKED SCANS OF CARRIER GAS COMPOSITION AND COMPENSATION FIELD**

### **5.1 Using Helium as a DIMS Carrier Gas**

The use of helium as the DIMS carrier gas, or as a part of a mixture of gases, can lead to the improvement of DIMS separations [1-5]. The cause for these improvements is that helium increases the differential ion mobility for all ions, although not equally. Ions with a higher differential ion mobility in nitrogen tend to undergo higher absolute increases in required compensation field upon the addition of helium to the carrier gas [6]. Although this is not universal, the general result is increased dispersion in the compensation field domain and improvement of DIMS separations [6,7]. However, the use of helium also results in a decrease in signal intensity due to the collisions of ions with either the DIMS electrodes or the housing containing the electrodes. This increase in ion collisions with the electrodes and housing stems from the differences in ion mobility through the smaller, less polarizable helium [1]. In comparison to nitrogen, helium decreases the reduced mass, the collisional cross-section, and long-range interactions of the collision partners [8,9]. These changes produce a greater difference between  $K_l$  and  $K_h$  and cause greater displacement during each period of the waveform, increasing the likelihood that ions will strike an electrode and be neutralized. Additionally, the ion motion parallel to the electrodes and transverse to the carrier gas flow is dictated by diffusion. The addition of helium to the carrier gas increases diffusion coefficients making ions

more likely to diffuse the width of the electrodes and be neutralized on the housing [10]. One can think of this from the perspective of the space of the separation. With the addition of helium and increased ion mobilities, the ions spread out into a greater space, but the available space is fixed by the dimensions of the device. This is very different from chromatographic and DT-IMS separations, where lengthening the separation time increases band broadening due to diffusion, yet the peaks are still detected and separation performance improves despite the band broadening. Both the height and width of the electrode gap in DIMS set a limit upon the maximum allowable ion motion. Beyond that the ions are neutralized upon collision with the DIMS housing and not detected. Ultimately, this loss of ion signal can reduce peak capacity by restricting the number of chemical species that can be separated and detected in a single analysis [8].

## 5.2 Introduction to Linked Scans

Linked scans were developed to improve separation characteristics through the use of helium while also reducing the ion losses typically seen when helium is used in the DIMS carrier gas. During linked scans the amount of helium present in the carrier gas is decreased as the compensation field is increased. An example of the linked scan produced is shown in Figure 5.1, where the helium content is scanned from 40 to 0% while the compensation field is scanned from 80 to 260 V/cm. By scanning the two parameters simultaneously, ions that require a low compensation field pass through DIMS with relatively high helium percentages, whereas the ions that pass through DIMS later in the compensation field scan do so with a primarily nitrogen carrier gas. In this work, each analyte studied has  $K_l > K_h$ . Thus analytes with a high difference between  $K_l$  and  $K_h$  can be expected to have  $K_l$  play the leading role in ion mobility. Dropping the amount of helium present in the carrier gas lowers  $K_l$ , ultimately reducing the likelihood of ion

collisions with the DIMS electrodes during any one cycle of the waveform and with the housing of the electrodes due to diffusion.

An example of the effects of adding helium to the carrier gas is shown in Figure 5.2, where compensation field scans with constant helium were taken in 5% increments from 0 to 60% helium. In this plot the normalized intensities of four ions as a function of carrier gas composition and compensation field are shown. The presence of helium in the carrier gas results in the ions having greater differential ion mobilities. This increases the characteristic  $E_C$  of the peaks and improves the separation capabilities of the analysis. Additionally, helium causes the peak centroids to be more widely distributed in the compensation field domain, with higher helium percentages resulting in greater distances between peaks. The reduction of the helium

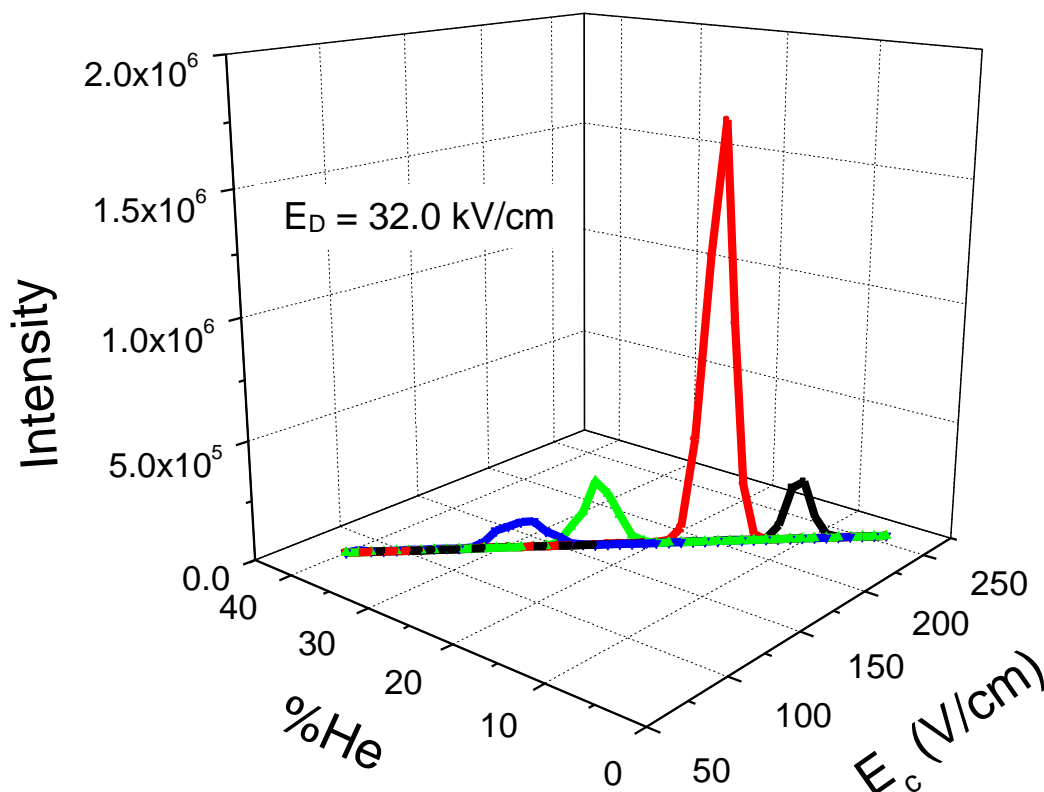


**Figure 5.1. A representative linked scan during which  $m/z$  622 (black), 922 (red), 1522 (green), and 2122 (blue, intensity x 5) from Agilent ESI tuning mix are separated. Here the helium is decreased from 40% to 0% as the compensation field is scanned**

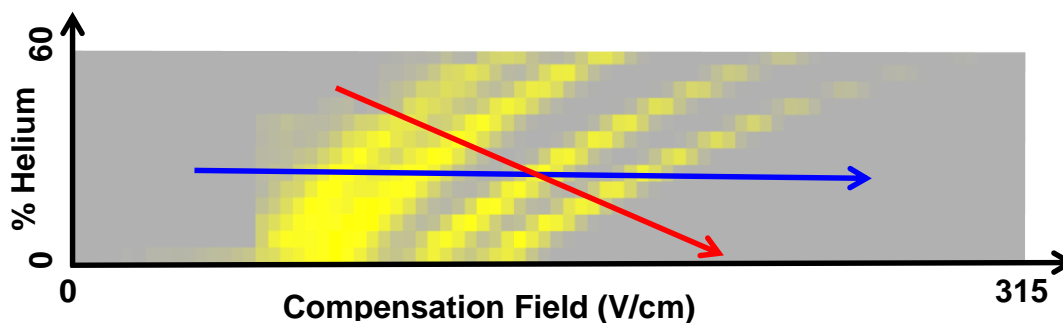


**Figure 5.2. Normalized intensities for  $m/z$  2122, 1522, 922, and 622 (left to right) as a function of helium content of the carrier gas and compensation field. The blue arrow represents the scan line of a compensation field scan with constant helium whereas the red arrow depicts the scan line of a linked scan**

content during linked scans results in peaks with centroids more closely spaced in the compensation field domain than compensation field scans with constant helium. However, the relationship between ion differential mobility and helium is such that in a linked scan the width of the intersection of the scan line with stable trajectories through DIMS (represented by the intensity plot in Figure 5.2) is reduced. Thus, the peaks will be narrowed along the scan line; potentially leading to improvements in resolution and peak capacity over compensation field scans with constant helium.

### **5.3 40 to 0% Linked Scans vs. Compensation Field Scans with Constant Helium**

The use of resolving power as a metric to describe DIMS separations has become commonplace because it allows for the rapid characterization and comparison of DIMS separations. However, the inability of resolving power to accurately describe linked scans would only become apparent through the studies presented herein. Thus, to begin to compare linked scans and compensation field scans with constant helium, the resolving power of peaks from three charge states of the protein ubiquitin were examined. For this work, the helium content of the carrier gas was lowered linearly from 40 to 0% during linked scans as the compensation field was linearly increased. These linked scans were compared to compensation field scans with 0,

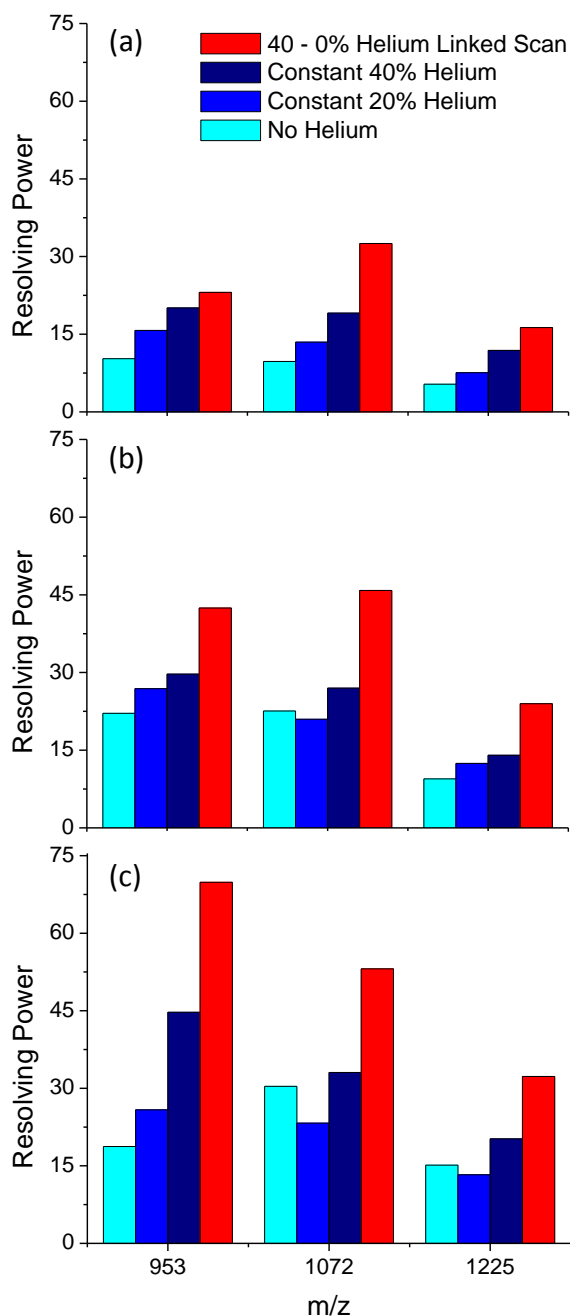


**Figure 5.3. Plots comparing the resolving powers for three charge states of ubiquitin. Compensation field scans with constant helium and linked scans from 40 - 0% helium are shown at  $E_D$  of (a) 26.0 kV/cm, (b) 30.0 kV/cm, and (c) 34.0 kV/cm. The  $9^+$  charge state of ubiquitin presented multiple peaks during DIMS scans. Peak statistics were taken for the most abundant peak, which required the highest compensation field to pass through DIMS**

20, or 40% constant helium. Shown in Figure 5.3, it was observed that for the  $7^+$  ( $m/z$  1225),  $8^+$  ( $m/z$  1072), and  $9^+$  ( $m/z$  953) charge states of ubiquitin linked scans yield higher resolving powers. At dispersion fields of 26.0, 30.0, and 34.0 kV/cm linked scans improved resolving power by an average of 54% over compensation field scans with 40% constant helium. Even greater gains in resolving power are observed for the 40 to 0% linked scans when compared to compensation field scans with 0 and 20% constant helium, as the compensation field scans with lower amounts of helium yielded lower resolving powers.

#### 5.4 Linked Scans vs. Compensation Field Scans with Constant Helium: Peak at Same Helium Percentage in both

The previous use of linked scans gave improved resolving powers, even though the ions passed through DIMS at lower than 40% helium during linked scans. For example, the linked scan in Figure 5.1

begins with 40% helium yet the peaks for  $m/z$  1522 and 922 pass through DIMS at 23.8 and 16.1% helium, respectively. A lower amount of helium leads to lower differential ion mobility, yielding lower resolving powers. Thus it was believed that to more accurately portray the improvements of linked scans, peaks should be compared to compensation field scans with constant helium at the same helium percentage present at the centroid of each peak in the linked scan. For this assessment the resolving powers of four peaks from Agilent ESI tuning mix were compared for linked scans and compensation field scans with constant helium. Compensation field scans with constant helium were taken in 5% increments from 0 to 60% at a dispersion field of 28.0 kV/cm, and the resolving power of the linked scan peak was compared to the compensation field scan with the closest amount of constant helium. To elaborate, one experiment gave the peak for  $m/z$  922 to be centered at 16.1% helium in the helium domain during a linked scan. The resolving power of this peak was compared to a compensation field scan with constant 15% helium present in the carrier gas. The results presented in Figure 5.4 show that linked scans from 20-0, 40-0, and 60-0% helium improve the resolving powers of the four analyte ions ( $m/z$  622, 922, 1522, and 2122) versus compensation field scans with constant helium.

## **5.5 Issues with Experimental Design to this Point**

Despite these promising results it was suspected that the point in the helium/compensation field scans at which the peak passed through DIMS might be causing inconsistencies in the data. For example, a higher amount of helium in the carrier gas causes higher required compensation fields for the ubiquitin peaks. However, if the scanned compensation field range was not properly adjusted when increasing the helium range of a linked scan, the peaks would pass through DIMS after more steps were taken in the compensation field



and helium domains. This can be seen in Figure 5.5 where rather than shift the entire compensation field range such that the peaks are centered in the 60-0% helium scan, the compensation field range was extended on only the lower end. The compensation field scan ends at 225 V/cm in both the 40-0 and 60-0% helium scans, but the 60-0% helium scan begins at a lower  $E_c$ . Based on the relationship between ion mobility and helium, this causes the peaks to pass through DIMS after significantly more compensation field steps. Thus, the ions would pass through DIMS at a lower helium content and have lower than expected differential ion mobilities, necessitating lower compensation fields to correct for their net displacement. In Figure 5.5, this essentially results in the peaks in the two scans passing through DIMS at the same required compensation fields, rather than a higher helium range raising the required compensation fields. A similar effect

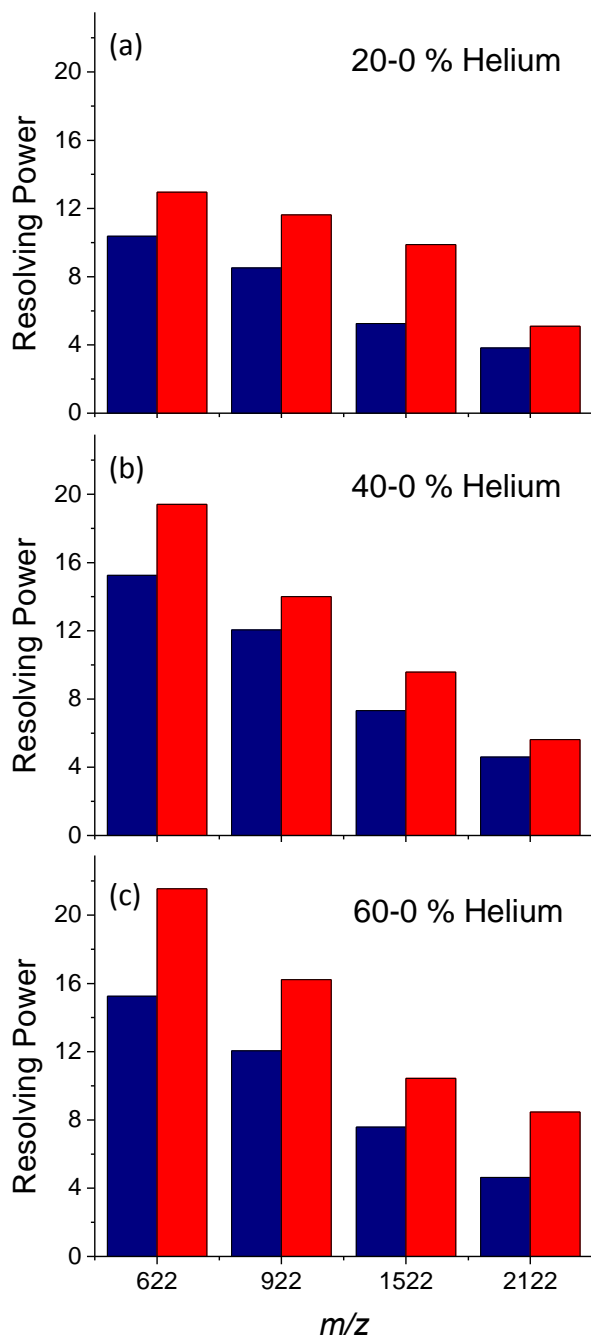


**Figure 5.4. Plots comparing the resolving power of linked scans (red) to compensation field scans with constant helium (blue). The scans with constant helium were taken with approximately the same helium content that was present when the peaks passed through DIMS in the linked scan. The linked scan helium ranges shown are (a) 20-0%, (b) 40-0%, and (c) 0-60% helium**

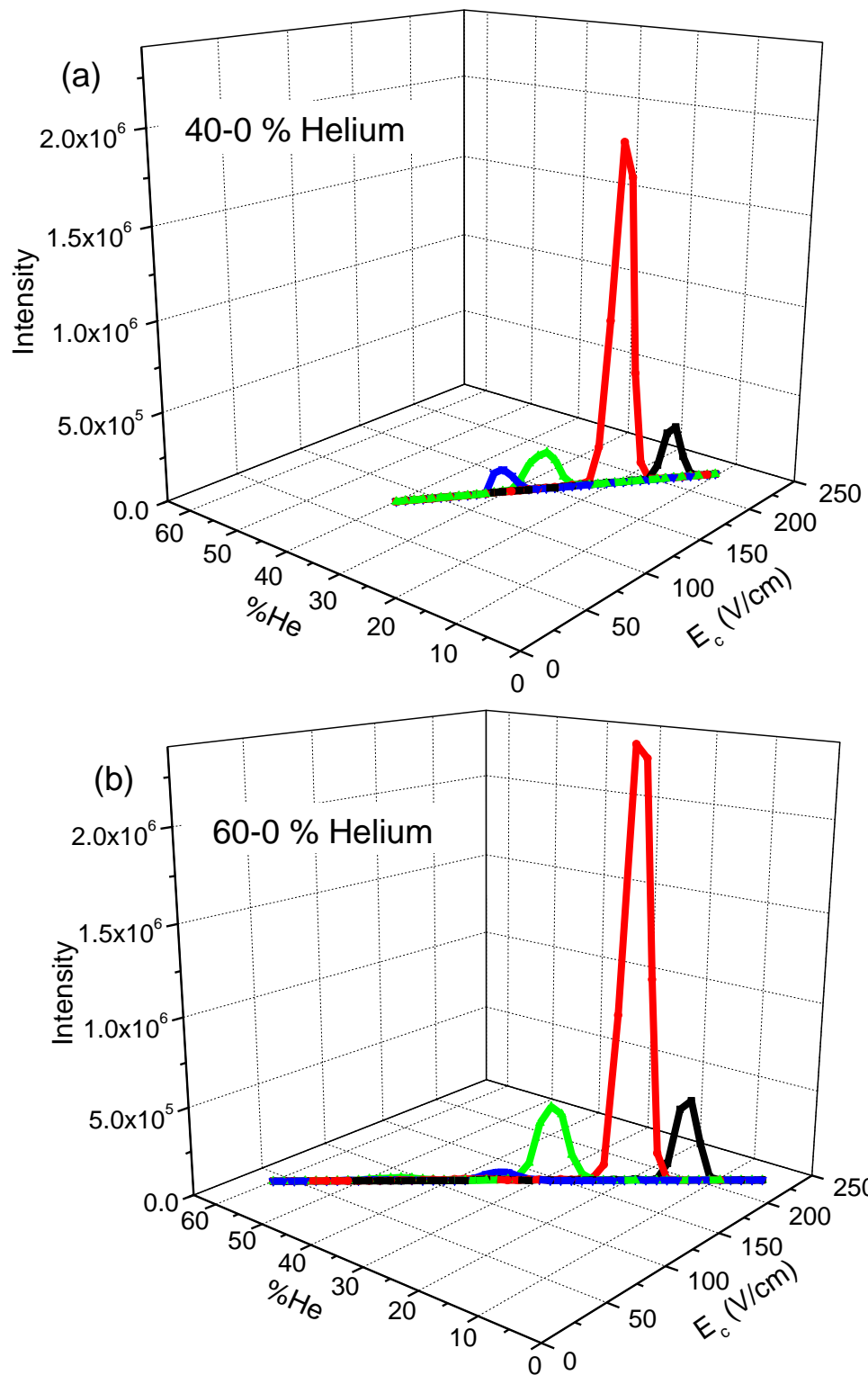


**Figure 5.5. Plots showing how the scanned compensation field range was changed between (a) 40-0% and (b) 60-0% helium linked scans**

could be expected when increasing dispersion field, which also increases the required compensation fields for the ubiquitin peaks.

## **5.6 Slope Experiment: One $E_C$ , One Helium %**

Based on these studies it was determined that the peak position in both the helium domain and compensation field domain needed to be controlled to allow for the true value of linked scans to be determined. Therefore, compensation field scans were performed with the peak centroid of  $m/z$  922 held constant in both domains. This would allow for the effect of passing through the point at different angles, such as in linked scans with different rates at which the helium content is lowered with respect to compensation field (i.e. linked scans with different slopes), to be compared to a compensation field scan with constant helium.

The difference between this experiment and a typical linked scan experiment is shown in Figure 5.6. Linked scans without holding the centroid of a peak constant in both scans are depicted in Figure 5.6a. In these experiments each ion passes through DIMS at different  $E_C$  and helium content depending on the linked scan used. Holding the centroid constant in the two dimensions while changing the slope of the linked scan is depicted in Figure 5.6b. Here it is shown how changing the slope of the linked scan affects the intersection of the linked scan line and the stable trajectories through DIMS. The effect of this slope on resolving power is shown in Figure 5.7. At dispersion fields of 24.0 and 32.0 kV/cm it is observed that changing the slope of the helium scan with respect to compensation field increases the resolving power for  $m/z$  922 in a linear fashion.

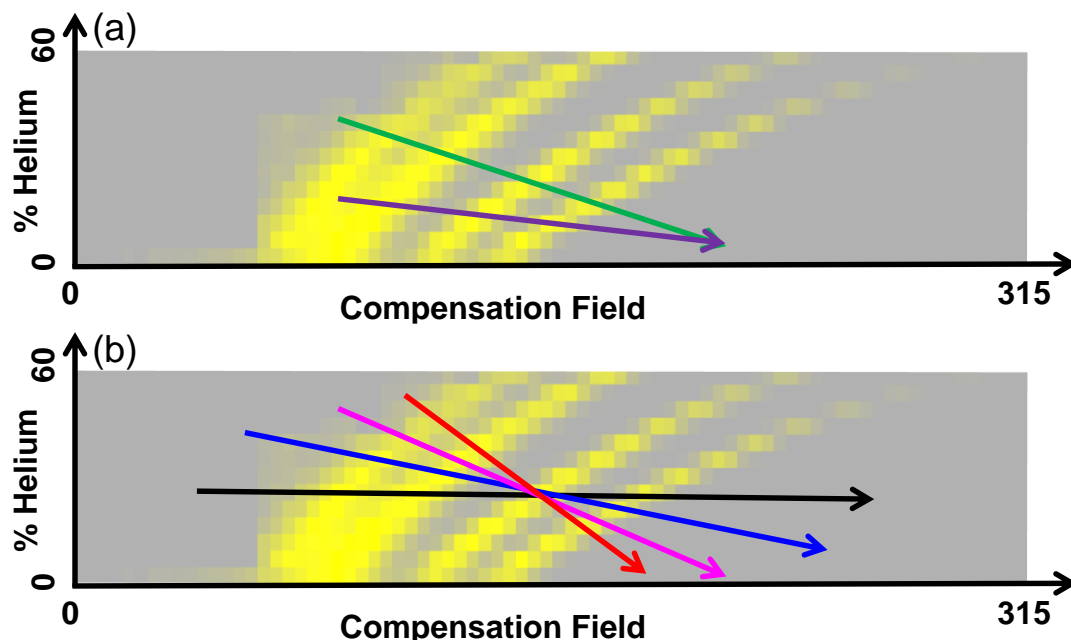
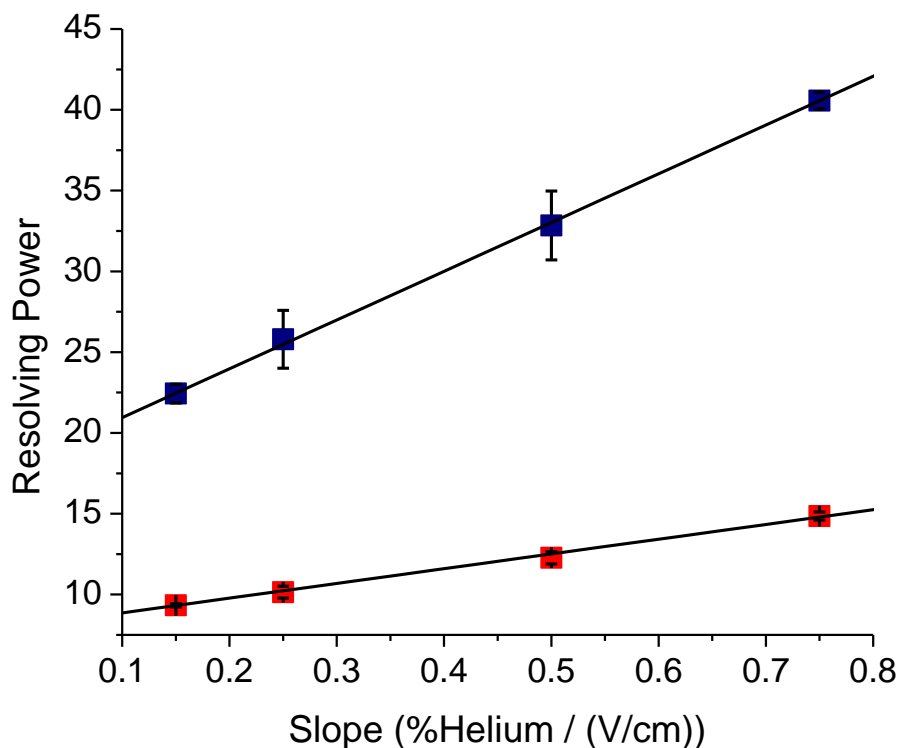


Figure 5.6. In both (a) and (b) the normalized intensities for  $m/z$  2122, 1522, 922 and 622 (left to right) are shown as a function of helium and compensation field. The intensity (shown in yellow) depicts stable trajectories through the DIMS device. (a) Depiction of 40-0% (green) and 20-0% (purple) helium linked scans without holding the centroid of a peak constant in both scans. (b) The black (constant helium), blue, magenta, and red arrows, respectively, are indicative of increasing the rate at which helium is changed with regards to compensation field. The common intersection of the arrows is representative of keeping the peak centroid for  $m/z$  922 constant in the helium and compensation field domains

## 5.7 Maximizing Resolving Power

### 5.7.1. Agilent ESI Tuning Mix

In an attempt to maximize resolving power, the slope of the helium scan was increased by almost two orders of magnitude, the results of which can be seen in Figure 5.8. Increasing the helium scan rate to (90% Helium)/(V/cm) increases the resolving powers for  $m/z$  922 and  $m/z$  1522 to 1573 and 1716, respectively, at 31.0 kV/cm. These values are over 3 times greater than the best reported value in the literature of 500 [11]. However, during these experiments it was observed that as the resolving power increased for the two peaks, the ability to separate the two analytes stayed constant. Upon calculation of the resolution between the two peaks, it was observed that despite the impressive gains in resolving power no improvement in resolution was measured (Figure 5.9).



**Figure 5.7. Plots of resolving power versus the rate at which helium percentage is lowered with respect to compensation field at dispersion fields of 24.0 kV/cm (red) and 32.0 kV/cm (blue)**

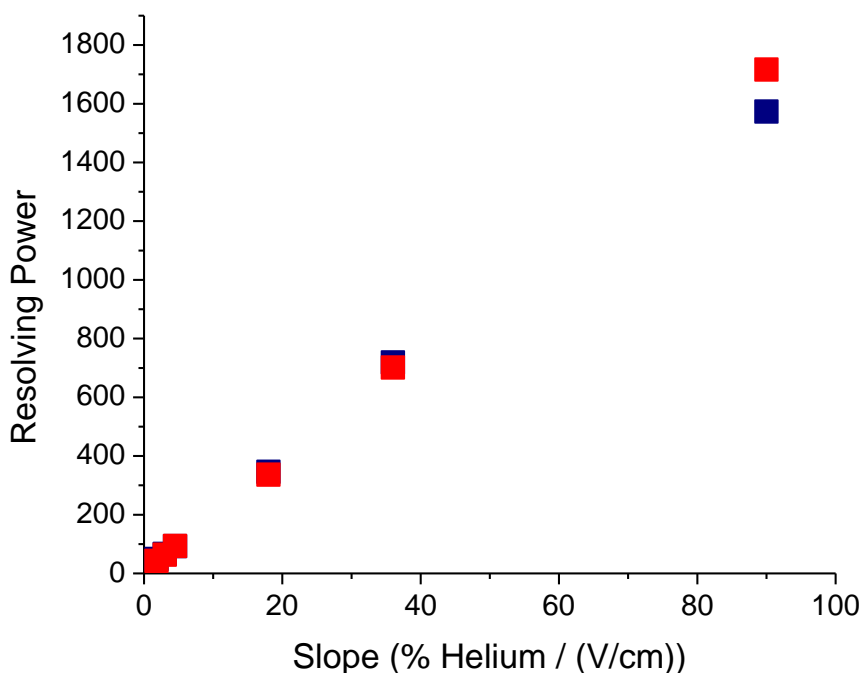


**Figure 5.8. Plot showing the effect on resolving power of increasing the rate at which helium content is lowered relative to compensation field. The resolving powers for  $m/z$  922 (blue) and  $m/z$  1522 (red) reach 1573 and 1716, respectively**

This seemingly contradictory result stems from the manner in which resolving power is calculated. Resolving power is determined solely based on the required compensation field and the width of the peak, measured as the full width at half maximum in the compensation field domain. By changing the slope of the helium scan the peak width is narrowed in regards to the compensation field domain. The peak FWHM were reduced from an average of 21.8 V/cm with no helium present to 0.1 V/cm at the highest linked scan slope. However, at the same time the distance between the peak centroids was decreased from 36.8 to 0.3 V/cm. The combination of these factors yields impressive resolving powers but no improvement in resolution between the two peaks.

#### 5.7.2. Syntide 2

To more closely compare the resolving powers attained using linked scans to the best values reported in the literature for DIMS, the effect of slope was investigated using the peptide

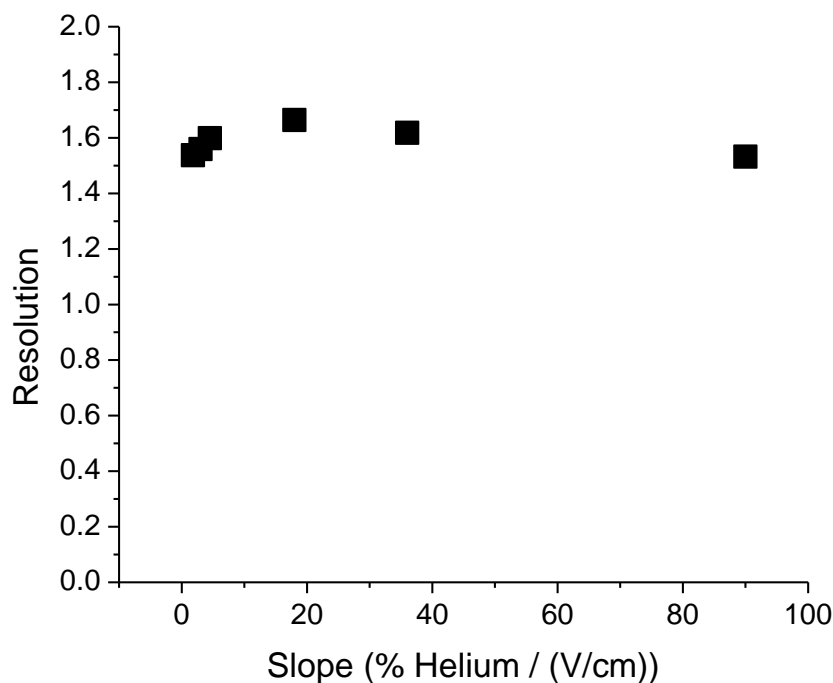


**Figure 5.9. Plot of resolution versus the rate at which helium content is lowered relative to compensation field**

syntide 2 [3,6,9,11,12]. Multiple peaks were observed for the triply charged species during compensation field scans, however, only the most intense DIMS peak was analyzed in a similar manner as the peak for  $m/z$  922 in the previous experiment. Holding the peak centroid constant in both the compensation field and helium domains, increasing the slope of the helium scan with respect to the compensation field scan once again increased resolving power in a linear fashion (Figure 5.10). At a dispersion field of 28.7 kV/cm, resolving powers above 7900 were obtained using syntide  $2^{3+}$ . This value is consistent with the values obtained for  $m/z$  922 from Agilent ESI tuning mix as the syntide  $2^{3+}$  peak was more narrow (12.4 V/cm versus 19.3 V/cm) during compensation field scans with no helium present, and the compensation field centroid used during this slope experiment for syntide  $2^{3+}$  was higher (327.9 V/cm versus 170.5 V/cm). The resultant resolving power is over 16 times greater than the best previously reported value;

however, as stated above the increase in resolving power does not correlate to improvement in the separation capabilities of the device [11] .

It should be noted that the resolving power of a peak is dependent on a number of attributes of the device. Parameters such as the ion transit time through the DIMS device and the reduced electric field strength used affect the resolving power measured. For example, at a dispersion field of 28.7 kV/cm and constant 40% helium carrier gas the DIMS device discussed in this work gave a resolving power of 30.1 for syntide  $2^{3+}$ . Under those conditions the DIMS device that produced resolving powers of 500 yielded a resolving power of 175 for syntide  $2^{3+}$  [12] . Thus it could be expected that the combination of the linked scans discussed here and the DIMS device described elsewhere would yield even greater resolving powers.

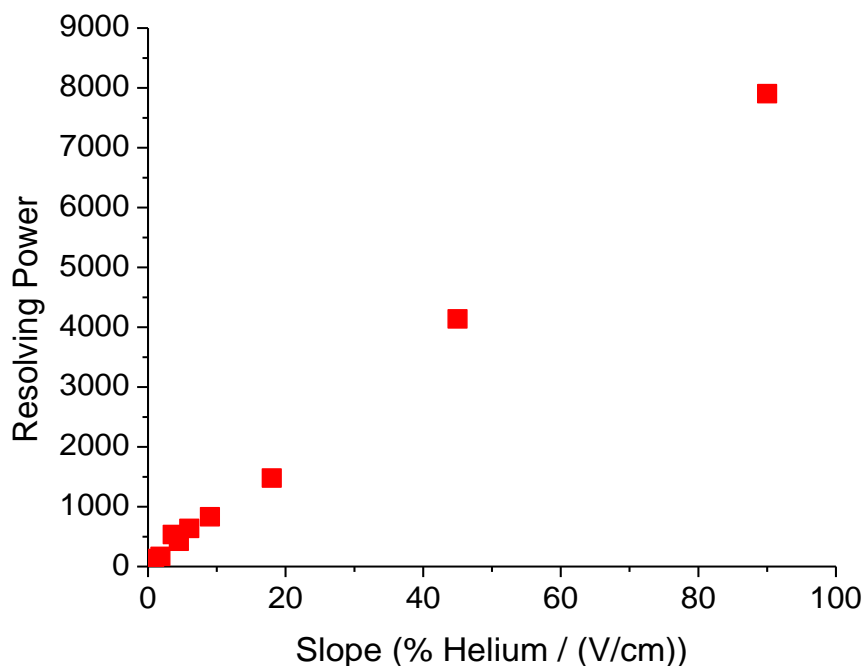


**Figure 5.10. Plot showing the effect on resolving power of increasing the rate at which helium content is lowered relative to compensation field. The resolving powers for syntide  $2^{3+}$  reaches 7903 (FWHM = 0.04 V/cm) at the highest slope used**



Another issue that presents itself when using resolving power is that because DIMS separates ions based on their differences in mobilities between the high and low fields, a higher resolving power stemming from a greater required compensation field gives little information about ion motion within the DIMS gap. In chromatographic and DT-IMS separations it can be expected that all peaks will be detected, the last of which will have the highest resolving power. In DIMS, the spatial restrictions set by the physical dimensions disallow these generalizations. Ion populations with a greater differential ion mobility than that of the ion used to report resolving power can be entirely lost due to collisions with the electrodes. Alternatively, ion populations with large  $K_l$  and  $K_h$  can require minimal compensation field, yet be lost by diffusion to the DIMS housing or to an electrode due to an oscillation during one portion of the waveform. Thus, in either case the number of analyte peaks detected is lowered and the overall peak capacity of the separation can be reduced, even though the reported resolving power is increased.

## **5.8 Switching Characterization Figures of Merit**

### **5.8.1. Ubiquitin**

To more accurately compare linked scans and compensation field scans with constant helium, experiments were performed evaluating the resolution between charge states of the protein ubiquitin. As shown in Figure 5.11, at dispersion fields of 23.3 and 26.7 kV/cm an increase in helium content improves the resolution between the  $8^+$  and  $9^+$  charge states of the protein for both compensation field scans with constant helium and linked scans. However, these improvements do not stem from the same cause. For compensation field scans with constant

helium resolution is improved when using helium predominantly due to the distance between the peak centroids being increased in the compensation field domain. This effect combines with a slight narrowing of the DIMS peaks due to the greater likelihood of ions striking the electrodes to give the improvements in resolution observed. Alternatively, linked scans result in peaks with centroids less dispersed in the compensation field domain. The improvement in resolution comes from a more drastic narrowing of the peaks that compensates for the shorter distance between centroids. This occurs because of the narrower intersection of the scan line with stable trajectories (i.e. % He vs. compensation field, Figure 5.2) through the DIMS device.

A comparison between compensation field scans with constant helium and linked scans with regards to signal intensity can be seen in Figure 5.11.

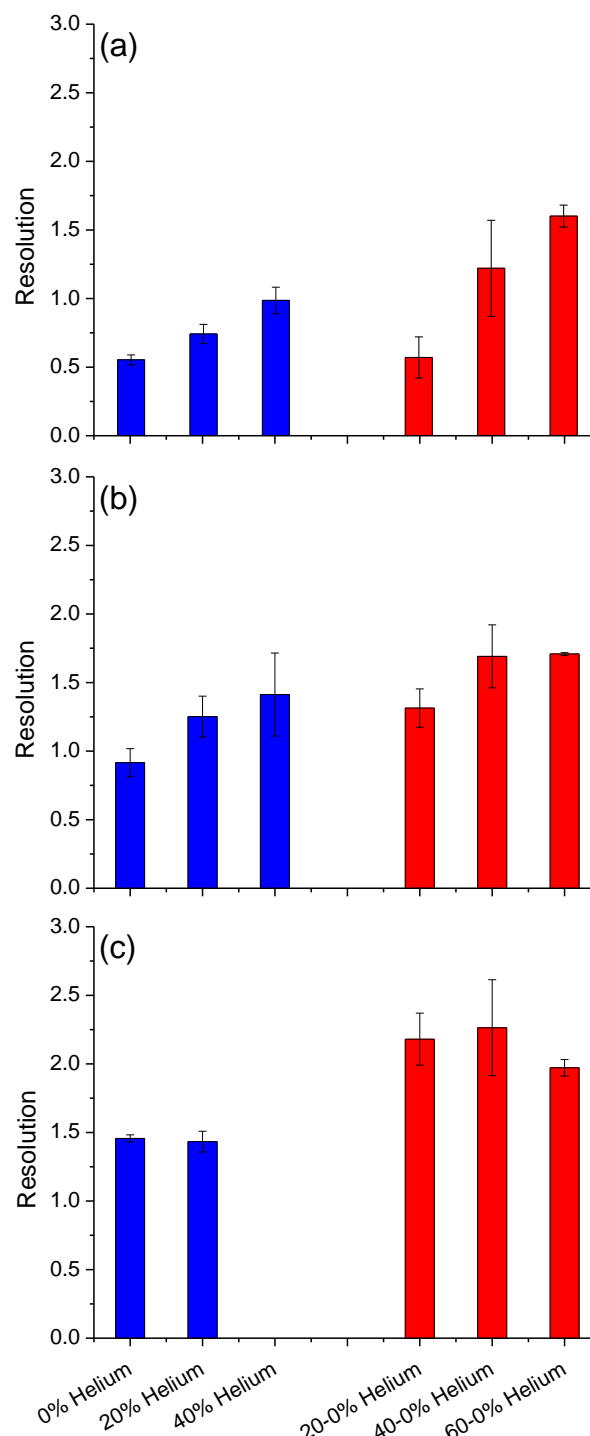


**Figure 5.11. Comparison of resolution between the  $8^+$  and  $9^+$  charge states of ubiquitin using compensation field scans with constant helium (blue) and linked scans (red). The benefits of linked scans become more apparent as the dispersion field is increased from (a) 23.3 kV/cm, to (b) 26.7 kV/cm, and finally to (c) 30.0 kV/cm**

With constant 40% helium and dispersion field of 30.0 kV/cm, the signal for the 9<sup>+</sup> charge state is reduced to an extent that no peak statistics could be obtained. The amount of helium present in the carrier gas produces an ion mobility high enough that an insufficient number of ions passes through the DIMS device to the mass spectrometer. However, in the linked scan this peak is readily detectable because it passes through DIMS at a high compensation field and low helium percentage. This type of reduction in signal loss is further exemplified in Figure 5.12, where the addition of helium has a drastic effect on the measured signal for each protein charge state detected. Linked scans, however, exhibit a much less severe loss of signal intensity in

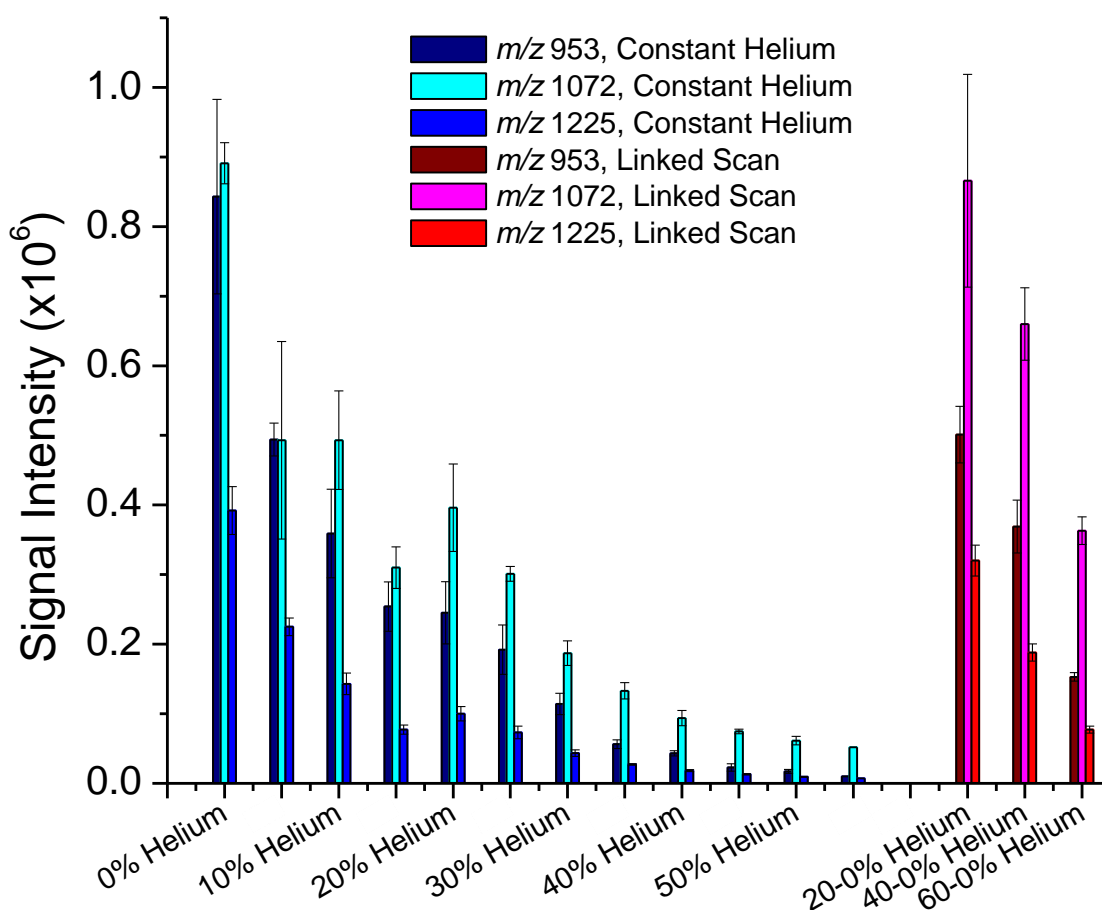


**Figure 5.12. Signal intensity for the 9<sup>+</sup> ( $m/z$  953), 8<sup>+</sup> ( $m/z$  1072), and 7<sup>+</sup> ( $m/z$  1225) charge states of ubiquitin as a function of helium present in the DIMS carrier gas ( $E_D = 23.3$  kV/cm)**

comparison to compensation field scans with constant helium, while providing improved resolution.

A potentially more useful comparison might be found in examining signal intensity at similar resolutions. For example, compensation field scans with constant 40% helium and linked scans from 40 - 0% helium give similar resolution between ions of  $m/z$  953 and 1072 (Figure 5.11) at  $E_D = 23.3$  kV/cm. However, the signal intensity of the three charge states is on average a factor of 8.6 times higher in the linked scans than in the compensation field scans with constant helium. The combination of improved resolution and signal intensity make linked scans a potentially useful technology for the analysis of difficult to separate, low abundance analytes.

#### 5.8.2. Trypsin Digest of BSA

The overall peak capacity of DIMS separations can also be increased when using helium in the DIMS carrier gas [8]. The use of helium raises the characteristic compensation field of all analytes to higher absolute values, but does not do so equally; ions with higher differential mobilities typically have a greater increase in compensation field than ions with low differential mobilities. One example of this is shown in figure 5.2b, where the peak centroids for ions of  $m/z$  622 and 1522 are located at 145 and 93 V/cm, respectively, when no helium is present in the carrier gas. When the carrier gas is comprised of 45% helium, ions of  $m/z$  622 pass through the DIMS device at a compensation field of 239 V/cm, whereas ions of  $m/z$  1522 require a compensation field of 146 V/cm. Thus, the change in characteristic  $E_c$  was 96 V/cm for the ions with higher initial differential ion mobility whereas the increase was only 53 V/cm for the other species. The practical application of this is that if all peaks are detected during an analysis the compensation field range over which ions pass through the DIMS device can be increased and peak capacity improved when helium is added to the carrier gas. However, the ions responsible

for extending the sampled compensation field range at the highest end in pure nitrogen commonly have mobilities too high to make it through the DIMS device when helium is present in the carrier gas. If too few of the analyte ions requiring the highest compensation field pass through DIMS, there will be no peak for that analyte during the compensation field scan. Therefore the  $E_C$  of those ions is no longer used in the peak capacity calculation and instead the  $E_C$  of the ions with the next highest differential ion mobility is used. Thus, the compensation field range over which analytes are detected is limited at the high end as peaks become undetectable. Additionally, the ions with the lowest differential mobility are still detected, and their characteristic  $E_C$  continues to increase as helium is added. This would be analogous to increasing the dead time in chromatography by increasing the length of the column but meanwhile there is a time limit beyond which peaks cannot be detected. As the length of the column increases the amount of time over which peaks can elute would ultimately be reduced. In DIMS this upper limit is the physical limitation on ion movement imparted by the electrodes, which combines with the increases in  $E_C$  on the low side when helium is added to shorten the compensation field range over which ions are detected. Thus, the peak capacity is diminished even though resolution between peaks or overall resolving power is increased when helium is added.

To examine the use of linked scans to alleviate this issue, the peak capacities of linked scans and compensation field scans with constant helium were compared using a tryptic digest of BSA. The overall separation characteristics of the scan modes are compared through use of the 50 most intense peaks in the mass spectrum of trypsin digested BSA. The results are shown in Figure 5.13, where it can be observed that linked scans improve DIMS peak capacity over

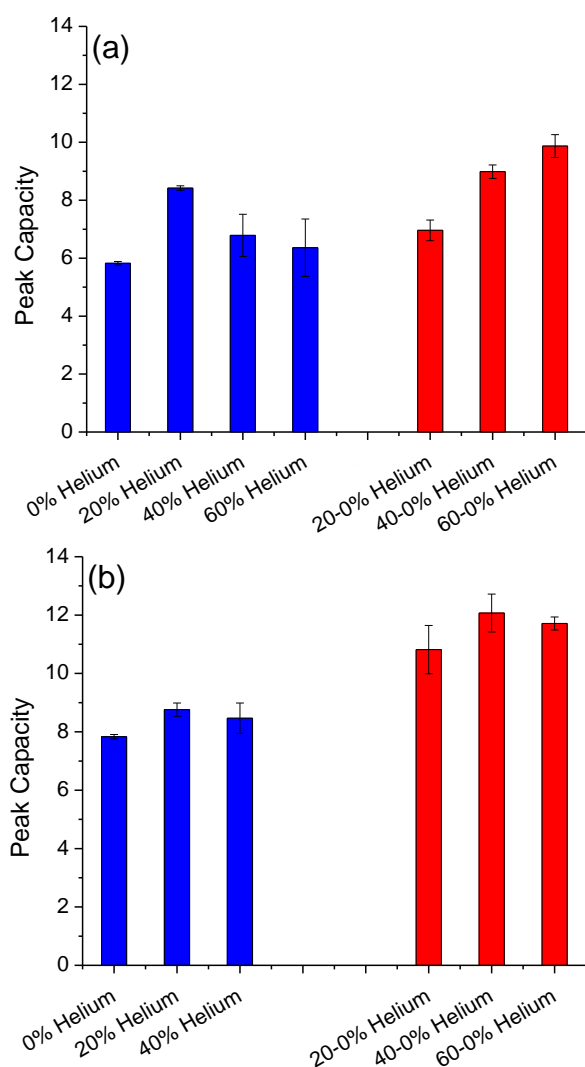


**Figure 5.13. Comparison of the peak capacity during analyses of BSA using compensation field scans with constant helium (blue) and linked scans (red). Linked scans offer improved peak capacities at both 26.7 kV/cm (a) and 30.0 kV/cm (b), particularly at higher helium contents and scan ranges**

compensation field scans with constant helium. At a dispersion field of 26.7 kV/cm, the use of constant 20% helium improves peak capacity. However, further addition of helium causes a drop in peak capacity. This contrasts with linked scans, which exhibit a distinct increase in peak capacity as the range of scanned helium increases to 40 - 0% and 60 - 0%.

Increasing the dispersion field to 30.0 kV/cm yields a similar trend for compensation field scans with constant helium, but the peak capacity of each linked scan range is greater than that of best compensation field scan with constant helium. It should be noted that compensation field scans with constant 60% helium were not performed at 30.0 kV/cm due to the increased likelihood of arcing within the DIMS electrodes at

these settings. The 60-% helium linked scan posed significantly less risk as the amount of helium in the carrier gas was 60% for only a few moments at the start of the each scan.

These improvements in peak capacity of linked scans over compensation field scans with constant helium are not solely due to the same causes as the improved resolution discussed previously. Here again, the average FWHM decreases as a function of increased helium for both the linked scans and compensation field scans with constant helium (Table 5.1). This alone would lead to improved peak capacity, suggesting another factor is the cause for the lower peak capacities in the compensation field scans with higher constant helium. In Table 1 it is shown that the fall off in peak capacity stems from a decrease in the compensation field range over which peaks are detected. The high helium content of the carrier gas in compensation field scans with 40 and 60% constant helium increases the likelihood that the analyte ions will be lost to neutralization by both increasing the differential ion mobility and lateral diffusion to the electrode housing. If the peaks for the analytes with the highest differential ion mobilities go undetected, the compensation field range is shortened as previously discussed and peak capacity is lowered. This is exacerbated at the higher dispersion fields, as increases in dispersion field also increase the differential mobility of peptide ions causing more ions to be neutralized via collisions with the electrodes. However, the reduction of helium during linked scans decreases the likelihood of ion neutralization due to collisions with the electrodes or electrode housing.

	Compensation Field Scans with Constant Helium				Linked Scans		
	0%	20%	40%	60%	20 - 0%	40 - 0%	60 - 0%
FWHM	20.8 ± 0.3	20.3 ± 0.3	18.5 ± 0.6	15.0 ± 1.1	17.7 ± 1.8	15.5 ± 0.4	13.4 ± 0.3
Lowest E <sub>C</sub>	57.0 ± 1.5	71.5 ± 3.3	87.2 ± 1.8	113.3 ± 4.2	66.7 ± 0.8	78.1 ± 0.8	93.9 ± 3.7
Highest E <sub>C</sub>	178.3 ± 1.2	242.6 ± 5.2	212.6 ± 12.6	208.0 ± 5.2	189.8 ± 1.2	217.2 ± 2.3	223.1 ± 7.1
Δ E <sub>C</sub>	121.3 ± 1.8	171.1 ± 1.8	125.3 ± 12.2	94.6 ± 7.34	123.1 ± 0.7	138.9 ± 1.7	132.2 ± 7.0

**Table 5.1. FWHM, lowest and highest E<sub>C</sub> present in the DIMS scan, and compensation field range over which analytes pass through DIMS at E<sub>D</sub> = 26.7 kV/cm**

Thus these peaks are detected during linked scans, leading to further improvements in peak capacity as the helium range scanned increases to 60% and FWHM decreases.

The loss of analyte ions in compensation field scans with constant helium discussed in the previous section is shown in Figure 5.14 when observing the total ion current during a compensation field scan. The total ion current scan has two distinct peaks, from the separation of peptides of  $1^+$  and  $2^+$  charge states. At a dispersion field of 26.7 kV/cm, the initial addition of helium leads to significant ion loss, especially for the  $2^+$  peptides, which have higher differential ion mobility. A greater percentage of helium in compensation field scans with constant helium results in further reduction of signal intensity, with approximately 36% and 11% of the signal intensity retained for the two distributions when a 40% helium compensation field scan is compared to a 0% helium compensation field scan. Alternatively, increased helium ranges in linked scans result in less ion loss compared to compensation field scans with constant helium. With a helium scan range of 40 - 0% the signal intensity is 66% and 50% retained for the  $1^+$  and  $2^+$  peptides, respectively, compared to a 0% helium compensation field scan. A helium scan range of 60 - 0% yields signal intensity that is roughly 40% of the original intensity for both charge states. As with ubiquitin, linked scans provide improved separation characteristics in addition to improved signal for the analytes of interest.



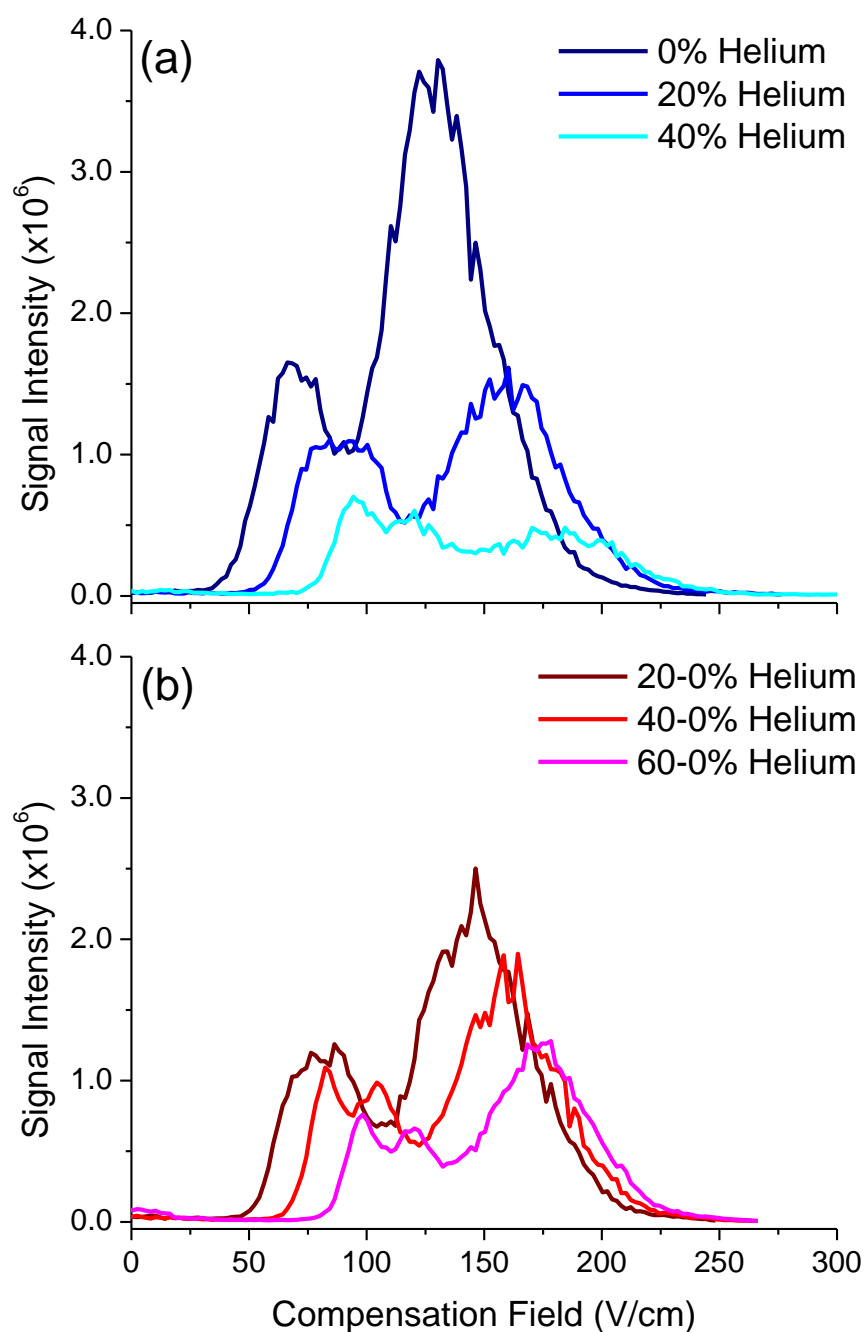


**Figure 5.14. Signal intensity for the TIC of bovine serum albumin as a function of helium content in the carrier gas for compensation field scans with constant helium (a) and linked scans (b) at  $E_D = 26.7$  kV/cm**

## 5.9 Summary and Conclusions

Initial studies comparing linked scans from 40 to 0 % helium and compensation field scans with constant helium yielded higher resolving powers during linked scans. Linked scans improved resolving power by 54% versus compensation field scans with constant 40% helium, and by even greater amounts compared to compensation field scans with constant 0 or 20% helium. A study was also completed where the resolving power of the peaks in linked scans were compared to those in compensation field scans with the same amount of helium as was present at the peak centroid in the linked scan. Again linked scans gave improved resolving powers. However, it was observed that the manner in which linked scans were adjusted when changing helium percentages and compensation field ranges caused inconsistencies in the results.

Due to this issue, experiments were conducted where the peak centroid was held constant in both the helium and compensation field domains. Varying the rate at which the helium percentage in the carrier gas was changed with respect to compensation field yielded a linear increase in the measured resolving power. This method was used to obtain resolving powers of over 7900; more than 16 times greater than the previously best reported value. However, while these linked scans provide significant increases in resolving power over compensation field scans with constant helium, these increases in resolving power do not translate to increases in resolution between peaks. For the particular ions from Agilent ESI tuning mix discussed the resolution between them was relatively constant. Thus, resolving power was unable to accurately describe the separations taking place during linked scans. The physical restrictions set by the dimensions of the DIMS gap, in combination with DIMS separations being based on differential ion mobility, makes resolving power an uninformative value for describing the separation capabilities of a DIMS device.

Instead, metrics such as resolution and or peak capacity should be used. Linked were shown to increase the resolution between charge states of ubiquitin. The best separation using linked scans improved the resolution between the 8<sup>+</sup> and 9<sup>+</sup> charge by 50% over the best compensation field scan with constant helium. These improvements can be attributed to the narrower intersections of the linked scan line with the stable ion trajectories through the DIMS device. This narrower intersection causes a significant reduction of FWHM for the peaks during linked scans. The addition of helium in both linked scans and compensation field scans with constant helium results in the separation of the peak centroids in the compensation field domain, while the lowering of the helium content in the linked scans results in less separation of the centroids. However, when coupled to the reduction in FWHM, resolution is improved in comparison to compensation field scans with constant helium. Linked scans were also shown to improve peak capacity for the analysis of trypsin digested bovine serum albumin, with the best linked scan increasing peak capacity by 38% over the best compensation field scan with constant helium.

This improvement in peak capacity is a result of the preservation of signal intensity for peaks at the highest compensation fields during linked scans. The mobilities of these ions in compensation field scans with high percentages of constant helium result in ion losses such that the ions were not detected, shortening the compensation field range used in the peak capacity calculation. These types of signal reduction at higher constant helium carrier gas percentages were apparent in the analyses of both ubiquitin and bovine serum albumin, whereas linked scans offered improved signal intensity retention at greater resolution or peak capacity. The combination of improved separation characteristics and signal intensity could allow for linked

scans to be used more widely for the analysis of complex mixtures, particularly those with analytes at low concentrations.

## REFERENCES

1. Shvartsburg, A. A.; Tang, K. Q.; Smith, R. D. Understanding and Designing Field Asymmetric Waveform Ion Mobility Spectrometry Separations in Gas Mixtures. *Anal. Chem.* **2004**, 76, 7366-7374.
2. Shvartsburg, A. A.; Li, F. M.; Tang, K. Q.; Smith, R. D. High-Resolution Field Asymmetric Waveform Ion Mobility Spectrometry using New Planar Geometry Analyzers. *Anal. Chem.* **2006**, 78, 3706-3714.
3. Shvartsburg, A. A.; Tang, K. Q.; Smith, R. D. Differential Ion Mobility Separations of Peptides with Resolving Power Exceeding 50. *Anal. Chem.* **2010**, 82, 32-35.
4. Isenberg, S. L.; Armistead, P. M.; Glish, G. L. Optimization of Peptide Separations by Differential Ion Mobility Spectrometry. *J. Am. Soc. Mass Spectrom.* **2014**, 25, 1592-1599.
5. Shvartsburg, A. A.; Ibrahim, Y. M.; Smith, R. D. Differential Ion Mobility Separations in Up to 100% Helium using Microchips. *J. Am. Soc. Mass Spectrom.* **2014**, 25, 480-489.
6. Shvartsburg, A. A.; Danielson, W. F.; Smith, R. D. High-Resolution Differential Ion Mobility Separations using Helium-Rich Gases. *Anal. Chem.* **2010**, 82, 2456-2462.
7. Santiago, B. G.; Harris, R. A.; Isenberg, S. L.; Ridgeway, M. E.; Pilo, A. L.; Kaplan, D. A.; Glish, G. L. Improved Differential Ion Mobility Separations using Linked Scans of Carrier Gas Composition and Compensation Field. *J. Am. Soc. Mass Spectrom.* **2015**, 26, 1746-1753.
8. Schneider, B.; Covey, T.; Coy, S.; Krylov, E.; Nazarov, E. Chemical Effects in the Separation Process of a Differential Mobility/Mass Spectrometer System. *Anal. Chem.* **2010**, 82, 1867-1880.
9. Shvartsburg, A. A.; Creese, A. J.; Smith, R. D.; Cooper, H. J. Separation of a Set of Peptide Sequence Isomers using Differential Ion Mobility Spectrometry. *Anal. Chem.* **2011**, 83, 6918-6923.
10. Giddings, J. C. Unified Separation Science; John Wiley and Sons, Inc., New York, 1991; p. 320.

11. Shvartsburg, A.; Seim, T.; Danielson, W.; Norheim, R.; Moore, R.; Anderson, G.; Smith, R. High-Definition Differential Ion Mobility Spectrometry with Resolving Power Up to 500. *J. Am. Soc. Mass Spectrom.* **2013**, 24, 109-114.
12. Shvartsburg, A. A.; Prior, D. C.; Tang, K.; Smith, R. D. High-Resolution Differential Ion Mobility Separations using Planar Analyzers at Elevated Dispersion Fields. *Anal. Chem.* **2010**, 82, 7649-7655.

## **CHAPTER 6: IMPROVED DIFFERENTIAL ION MOBILITY SPECTROMETRY SEPARATIONS USING SOLVENT VAPORS**

### **6.1 Benefits of adding Solvent Vapors to DIMS Carrier Gas**

It has previously been shown that the differential mobility of ions can vary based on changes in the position of functional groups within the ion and that the change in differential ion mobility can be intensified through the addition of polar solvents such as water, isopropyl alcohol, or acetonitrile to the DIMS carrier gas [1-7]. The solvent molecules interact with the ions as they travel through the DIMS device in a way that has been described using the cluster-decluster model [1,2,4]. During the low field portion of the waveform the effective temperature of the ion is relatively low and solvent molecules cluster around the ion, which reduces the mobility of the ion. The extent of the clustering is dependent on characteristics of both the ion and the solvent, including polarity, steric hindrance, and temperature [6-8]. During the high field portion of the waveform the effective temperature of the cluster is raised by collisions with the carrier gas [9]. This causes desolvation of the ion to occur and it travels as a bare ion until its effective temperature becomes low enough for clustering to reoccur. The net result of this cluster-decluster process is a change in the differential ion mobility, with the extent of that change being based on the specific properties of the ion, potentially increasing the selectivity of the DIMS separation. For ions with mobilities that increase as electric field strength increases, solvent molecules further lower the low field mobility while the high field mobility is relatively unaffected. Thus the differential ion mobility of the ion increases. Ions with mobilities that decrease as electric field increases when no solvent is present can also exhibit increases in

differential ion mobility upon the addition of solvent vapors to the DIMS carrier gas. In those cases the low field mobility of the ions is so reduced by the clustering of solvent molecules that the low field mobility is shifted such that it is actually lower than the high field mobility. In this case the differential ion mobility could be increased, but the polarity of the  $E_c$  required to pass the ions through DIMS would be reversed.

## **6.2 DIMS Separation of Glucose and Glucose Isomers**

One application where the use of DIMS and dopants could provide improvements over the currently used technology is for the separation of isomeric monosaccharides. Liquid chromatography coupled to mass spectrometry has commonly been used for the separation of sugar isomers but the speed of the analyses is often limited by the length of the chromatographic separations, which are typically 10-25 minutes in duration [10-13]. An alternative might be to utilize the selectivity of MS/MS to distinguish between the isomers, without chromatographic separation prior to ionization. However, it has been observed in our lab that when these molecules are ionized via ESI without a pre-ionization separation they show a preference towards forming the sodiated ion ( $[M+Na]^+$ ) with sodium atoms present in the ESI spray solvents versus the protonated ion ( $[M+H]^+$ ). Although the solvents are of Optima grade quality, various salts are used in the glass manufacturing process and these metals can leach from the glass in the presence of solvents. The formation of the sodiated ion makes MS/MS experiments ineffective for differentiation between structures because during CID the most common fragmentation is the removal of the neutral sugar molecule, which is undetectable via MS. Therefore, a rapid separation technique that gives differentiation between the isomers would be preferable to the technology currently used.



With that goal, glucose and three of its isomers were examined using DIMS with and without dopant vapors added to the DIMS carrier gas. The comparison between the DIMS separations without dopants versus the separation obtained when solvent was added at a flow rate of 1.8 mL/hour to the DIMS carrier gas is shown in Table 6.1. The resolution between the peaks of the sugars tested at each  $E_D$  and solvent vapor composition are shown, with the best separation between any two isomers highlighted in red. An example of each of the separations highlighted in red is also shown in Figure 6.1, where the DIMS scan for each combination of sugars is plotted. The fact that each of the best separations occurs when solvent vapors are added to the DIMS carrier gas emphasizes the ability of solvent vapors to improve the selectivity of DIMS separations. However, that the best separation between any two of the isomers does not take place using the same solvent or  $E_D$  points to a difficulty of using this technique. Even structures as similar as the ones used here can have differential ion mobilities affected in dissimilar ways by the addition of solvent vapor to the DIMS carrier gas, and the optimal combination of solvent and  $E_D$  must be determined empirically for each set of analytes. This optimization is similar to the development of a liquid chromatography method; however, and once it is complete for a set of analytes it does not need to be repeated each analysis. Despite this need for optimization, the improvement when dopant vapor is added to the DIMS carrier gas is clearly shown by the improvement in separations over DIMS separations when no solvent vapor is added.

$E_D = 25.0 \text{ kV/cm}$				$E_D = 29.2 \text{ kV/cm}$			
No Dopants	Glucose	Galactose	Fructose	No Dopants	Glucose	Galactose	Fructose
Galactose	0.09			Galactose	0.13		
Fructose	0.25	0.16		Fructose	0.87	0.33	
Mannose	0.04	0.06	0.22	Mannose	0.23	0.10	0.23
Methanol	Glucose	Galactose	Fructose	Methanol	Glucose	Galactose	Fructose
Galactose	0.15			Galactose	0.24		
Fructose	0.09	0.02		Fructose	(-)	0.12	
Mannose	0.11	0.25	0.17	Mannose	(-)	0.31	0.20
Water	Glucose	Galactose		Water	Glucose	Galactose	
Galactose	0.13			Galactose	0.20		
Fructose	0.15	0.13		Fructose	0.26	0.45	
Isopropyl Alcohol	Galactose			Isopropyl Alcohol	Galactose		
Glucose	0.12			Glucose	0.19		

$E_D = 33.3 \text{ kV/cm}$				$E_D = 37.5 \text{ kV/cm}$			
No Dopants	Glucose	Galactose	Fructose	No Dopants	Glucose	Galactose	Fructose
Galactose	0.14			Galactose	0.21		
Fructose	0.71	0.60		Fructose	0.83	0.66	
Mannose	0.42	0.29	0.32	Mannose	0.60	0.39	0.31
Methanol	Glucose	Galactose	Fructose	Methanol	Glucose	Galactose	Fructose
Galactose	(-)			Galactose	0.05		
Fructose	0.57	0.95		Fructose	<b>1.75</b>	1.03	
Mannose	0.08	<b>0.47</b>	0.45	Mannose	<b>1.12</b>	0.42	<b>0.64</b>
Water	Glucose	Galactose		Water	Glucose	Galactose	
Galactose	0.19			Galactose	0.05		
Fructose	0.48	0.68		Fructose	0.87	<b>0.98</b>	
Isopropyl Alcohol	Galactose			Isopropyl Alcohol	Galactose		
Glucose	<b>0.70</b>			Glucose	0.31		

**Table 6.1. Resolution between sugar isomer peaks during DIMS scans at different  $E_D$  and solvent vapor conditions**

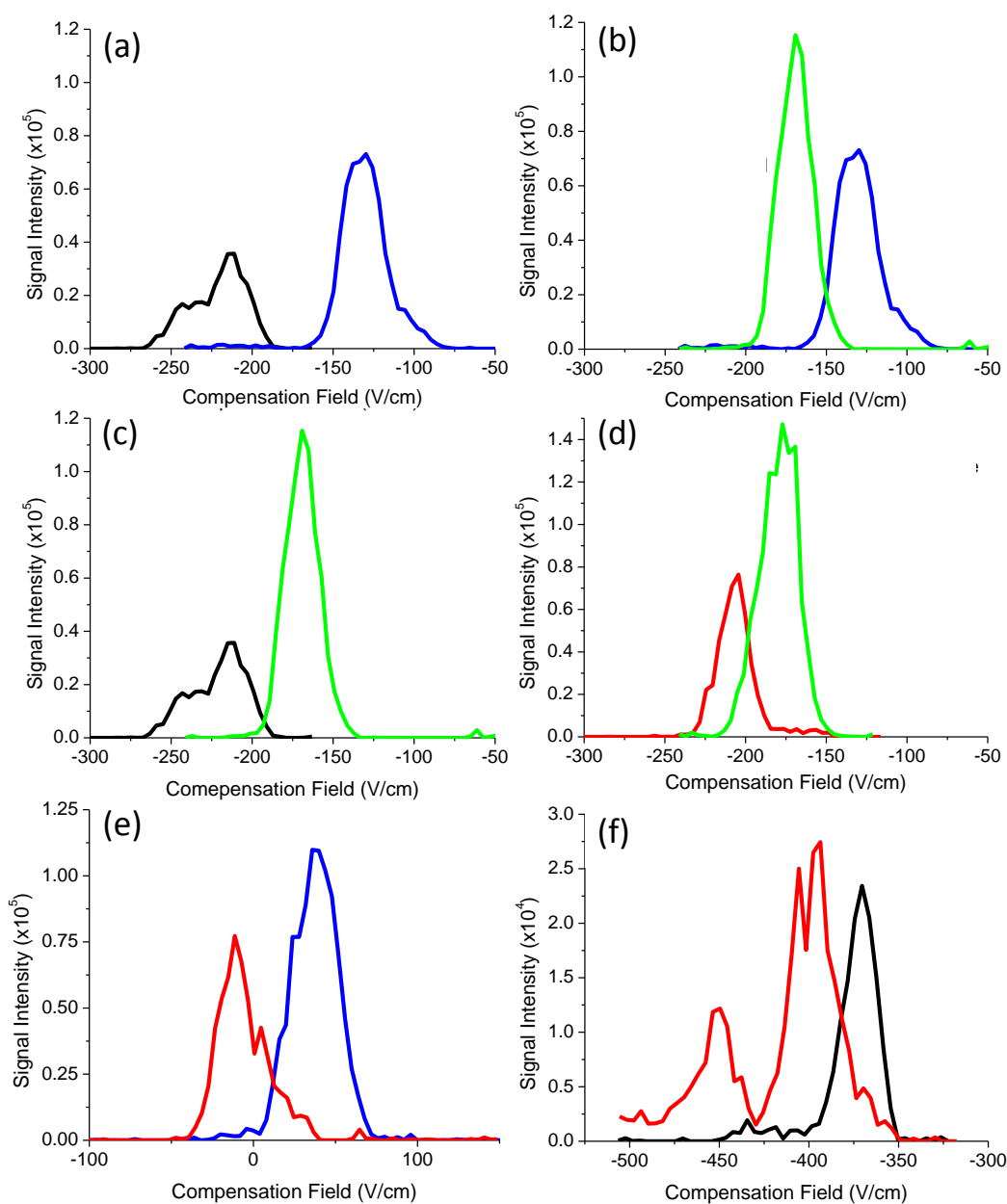


**Figure 6.1. DIMS spectra of the resolutions highlighted in red in Table 6.1.**  
 (a) D-glucose (black) and D-fructose (blue) (b) D-mannose (green) and D-fructose (blue) (c) D-glucose (black) and D-mannose (green) (d) D-galactose (red) and D-mannose (green) (e) D-galactose (red) and D-fructose (blue) (f) D-glucose (black) and D-galactose (red)

Also worth noting from Figure 6.1 is that some combinations of sugar, solvent vapor, and  $E_D$  led to the appearance of significant shoulders on peaks during DIMS scans or two peaks being present when only one isomer was expected. One example is present in Figure 6.1a and 6.1c, where it is shown that with 0.33% (v/v) methanol added to the DIMS carrier gas and an  $E_D = 37.5$  kV/cm applied D-glucose shows a shoulder on the more negative  $E_C$  side of the peak. An even more obvious example is the analysis of D-galactose with 0.17% (v/v) isopropyl alcohol added to the DIMS carrier, shown in Figure 6.1f and also Figure 6.2a-b. The analysis at  $E_D = 29.2$  kV/cm shown in Figure 6.2a yields a peak that is significantly wider than those typically observed for the glucose isomers, suggesting that two species may be present. Increasing the  $E_D$  to 33.3 kV/cm produces the DIMS scan shown in Figure 6.2b, which contains two distinct peaks for D-galactose. Alternatively, when analyzing D-fructose with an  $E_D = 29.2$  kV/cm and 0.33% methanol (v/v) present in the DIMS carrier gas two peaks for D-fructose are observed in the DIMS scan, as shown in Figure 6.2c. Whereas increasing the  $E_D$  to 33.3 kV/cm improved the separation between the two D-galactose species, the same increase in  $E_D$  yields a DIMS scan of D-fructose with only one peak, which is shown in Figure 6.2d. Based on the data collected no pattern was discernable for the combination of solvent and  $E_D$  that caused multiple peaks to be detected for a single compound. D-glucose, D-fructose, and D-galactose each yielded two peaks at different combinations of  $E_D$  and solvent vapor present in the DIMS carrier gas. In cases where significant shoulders or second peaks appeared in DIMS scans, the peak(s) was fit with two Gaussian peaks using Origin. The resolution reported in Table 6.1 is the resolution between the two nearest peaks in the DIMS scans from different sugars. For example, the

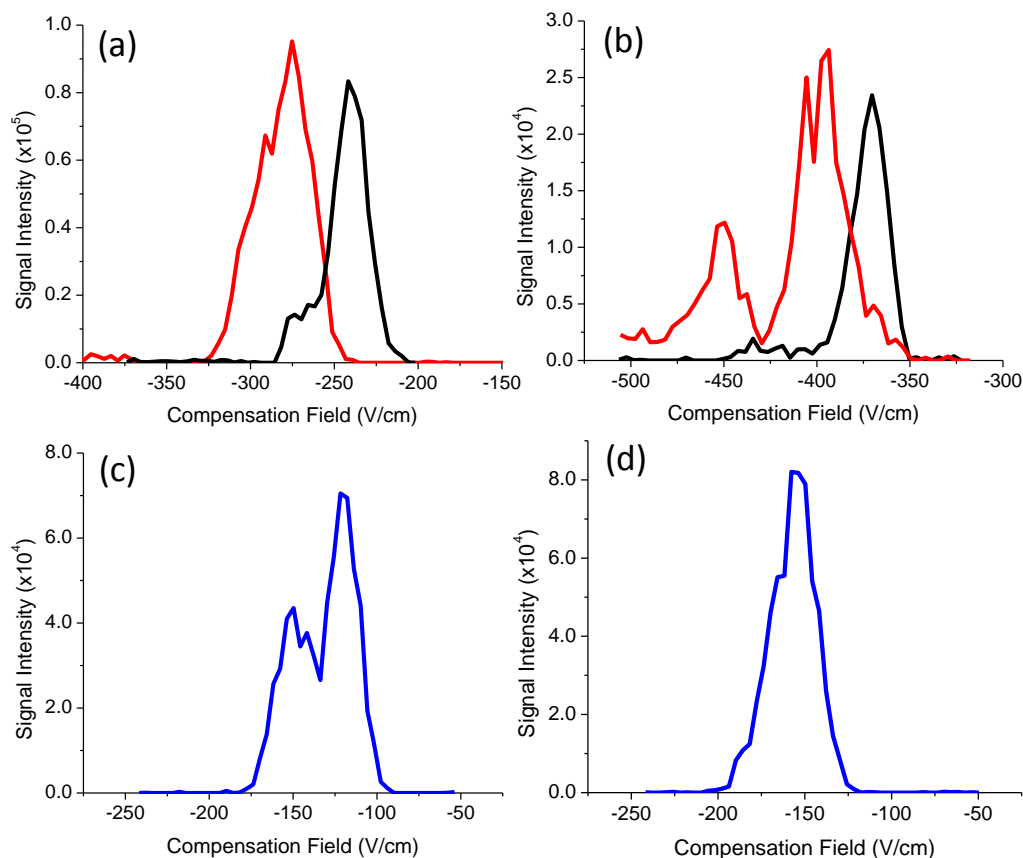


**Figure 6.2. DIMS scans showing the effects changing  $E_D$  and solvent vapor composition can have on DIMS separations. DIMS scans of D-galactose (red) and D-glucose (black) with 0.17% (v/v) isopropyl alcohol present in the carrier gas at (a)  $E_D = 29.2$  kV/cm and (b)  $E_D = 33.3$  kV/cm are shown. DIMS scans of D-fructose with 0.33% (v/v) methanol present in the carrier gas at (c)  $E_D = 29.2$  kV/cm and (d)  $E_D = 33.3$  kV/cm are also shown**

resolution reported that corresponds to Figure 6.1f is the average resolution between the D-glucose peak and the D-galactose peak present at an average  $E_C$  of -391.3 V/cm. Despite this approach to calculating resolution, for some combination of sugars, solvent vapor, and  $E_D$  no resolution is reported in Table 6.1 (designated by (-)). This is due to the presence of multiple peaks from both sugars which overlap, or the peak from one sugar being between two peaks from another sugar.

One possible explanation for the multiple peaks observed is the ability for sugars to undergo a ring opening process to an open-chain form. This dramatic change to the structure of

the ion could be expected to shift the differential ion mobility significantly, such as the shift in  $E_C$  shown in Figure 6.3 between DIMS scans of D-glucose and D-sorbitol. D-sorbitol might be expected to have a structure and differential ion mobility similar to that of open-chain glucose because D-sorbitol is the reduced form of D-glucose and cannot form a ring. However, the  $E_C$  of D-sorbitol is significantly more negative than both peaks present in the DIMS scan of D-glucose. Another fact that suggests the two peaks are not due to a ring opening process is that the open-chain aldehyde structure accounts for only 0.02% of the total amount of D-glucose in solution [14]. Although this is not directly relatable to the gas phase, studies investigating the gaseous conformation of sugars such as D-glucose, D-fructose, and D-ribose have found the open-chain structure to be in low abundance in the gas phase and significantly higher in energy than the cyclic forms [15-19].

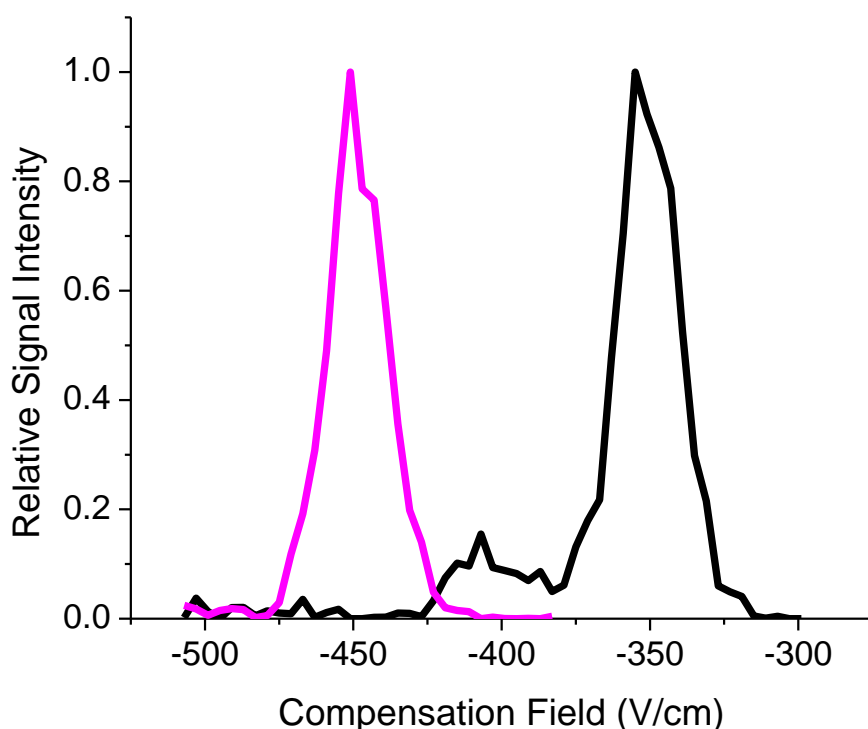


**Figure 6.3. DIMS scans of D-glucose (black) and D-sorbitol (magenta) with  $E_D = 33.3\text{kV/cm}$  and 0.17% (v/v) isopropyl alcohol present in the DIMS carrier gas**

An isomerization with expected ratios in solution more similar to those observed for D-glucose and D-galactose is the transition between  $\beta$  and  $\alpha$  anomers. Studies have shown D-glucose to be present as 62%  $\beta$ -D-glucose pyranose and 38%  $\alpha$ -D-glucose pyranose in solution [20]. During DIMS scans of D-glucose with 0.33% (v/v) methanol added to the carrier gas the signal intensity of the larger of the two peaks made up  $81.3 \pm 2.5\%$  of the combined signal with  $E_D = 33.3$  kV/cm and  $67.9 \pm 0.3\%$  of the combined signal with  $E_D = 37.5$  kV/cm. The same work that yielded the D-glucose solution phase ratios stated above also reported that D-galactose is present as 64%  $\beta$ -D-galactose pyranose and 30%  $\alpha$ -D-galactose pyranose in solution, with the remaining portion split between  $\beta$  and  $\alpha$  furanose structures [20]. Based on that  $\beta$ -D galactose pyranose would make up 68% of the signal intensity when considering just the two major conformations. In DIMS scans of D-galactose with 0.17% (v/v) isopropyl alcohol added to the carrier gas the signal intensity of the larger of the two peaks (the peak at the more positive  $E_C$ ) made up  $66.7 \pm 3.3\%$  of the combined signal with  $E_D = 33.3$  kV/cm and  $59.7 \pm 10.2\%$  of the combined signal with  $E_D = 37.5$  kV/cm. Although the gas phase ratios cannot be directly inferred from the solution phase ratios, work studying D-ribose in the gas phase has found the ratios to be within 5% of those reported for solution phase studies [15]. Other sugar anomers have been separated using DIMS previously, and assuming D-glucose and D-galactose follow the same trend in solution and gas phase ratios as D-ribose, it can be suggested that certain combinations of  $E_D$  and solvent vapor give DIMS the capability to separate anomers of the sugars studied in this work because the ratios reported for solution phase D-glucose and D-galactose largely align with the peak intensity ratios observed in DIMS scans [21].

However, this explanation does not fit for D-fructose because D-fructose is not expected to be present as  $\beta$  and  $\alpha$  pyranose anomers in solution [20]. Instead, fructose has been measured

as consisting of 65%  $\beta$ -D-fructose pyranose and 25%  $\beta$ -D-fructose furanose [9]. Based on just those two peaks,  $\beta$ -D-fructose pyranose would be expected to account for 72% of the combined signal intensity. This value is slightly higher than those detected during DIMS scans, where with 0.33% (v/v) methanol added to the carrier gas the signal intensity of the larger of the two peaks made up  $63.3 \pm 1.9\%$  of the combined signal with  $E_D = 25.0$  kV/cm and  $62.9 \pm 1.0\%$  of the combined signal with  $E_D = 29.2$  kV/cm. However, these differences in signal intensity ratio from the expected ratio might be attributed to unequal ion transmission through DIMS as the two ion populations have distinct differential ion mobilities. It should be noted that the presence of two peaks in this work contradicts the idea that D-fructose should have only one expected gas phase conformation described elsewhere; however, the cause for this discrepancy is still unknown [19]. Regardless, the general alignment of the signal ratios when two species are present during DIMS scans of D-glucose, D-galactose, or D-fructose with the expected solution phase ratios supports the identification of the species described above although absolute confirmation is not attained.

### **6.3 DIMS Separation of Phosphorylated Sugar Isomers**

Another example where DIMS analysis could be found valuable is for the separation of phosphorylated hexose isomers. Glucose-1-phosphate, glucose-6-phosphate, and fructose-6-phosphate play prominent roles in biological processes such as glycogenolysis, glycolysis, and the pentose phosphate pathway [22]. These compounds are typically found in low levels in cellular extracts, and as such have historically been measured using techniques such as enzyme assays [22]. More recently methods using LC-MS/MS have been of interest within the field; however, the length of the chromatographic separation necessary is a limiting factor during analysis [22-25]. Despite this limitation, the use of a LC separation prior to mass analysis is required because not only are the ions detected at the same mass-to-charge ratio, but many of the



ions formed during MS/MS experiments are present for all three isomers. This makes differentiation and quantitation of the isomers difficult when using only mass spectrometry [22,26].

To examine the potential of DIMS separations for these compounds the optimization of solvent vapor for the separation of deprotonated glucose-1-phosphate and glucose-6-phosphate ions was completed. From previous work in our lab and literature published on the use of dopants with DIMS it was believed that isopropyl alcohol and acetonitrile would provide the best separation of the isomers [6,27]. In Figure 6.4a it is shown that the resolution between glucose-1-phosphate and glucose-6-phosphate ions when no dopants are added to the DIMS carrier gas increases as the  $E_D$  is increased. However, upon the addition of isopropyl alcohol or acetonitrile to the DIMS carrier gas the resolution between the isomer ions is much improved, with acetonitrile yielding the best resolution. Although a level of separation sufficient to distinguish between the two species is reached with all three dopant conditions, signal intensity during DIMS analyses typically decreases as  $E_D$  is increased. This provides motivation to achieve separation at the lowest possible  $E_D$ , which occurs when acetonitrile is added to the desolvation

gas. An example of the separation achieved with each solvent setting at an  $E_D = 29.2$  kV/cm is displayed in Figure 6.4b-d and shows the improvement in separation when acetonitrile is used.

The ability to separate the glucose-1-phosphate and glucose-6-phosphate ions from ions of isomeric fructose-6-phosphate was then tested using acetonitrile. In Figure 6.5 it is shown that fructose-6-phosphate ions passes through DIMS at a higher  $E_C$  than the two glucose species, with the differential ion mobility of fructose-6-phosphate ions being more closely aligned with that of the glucose-6-phosphate ions. Also shown in Figure 6.5 is that there is less separation between

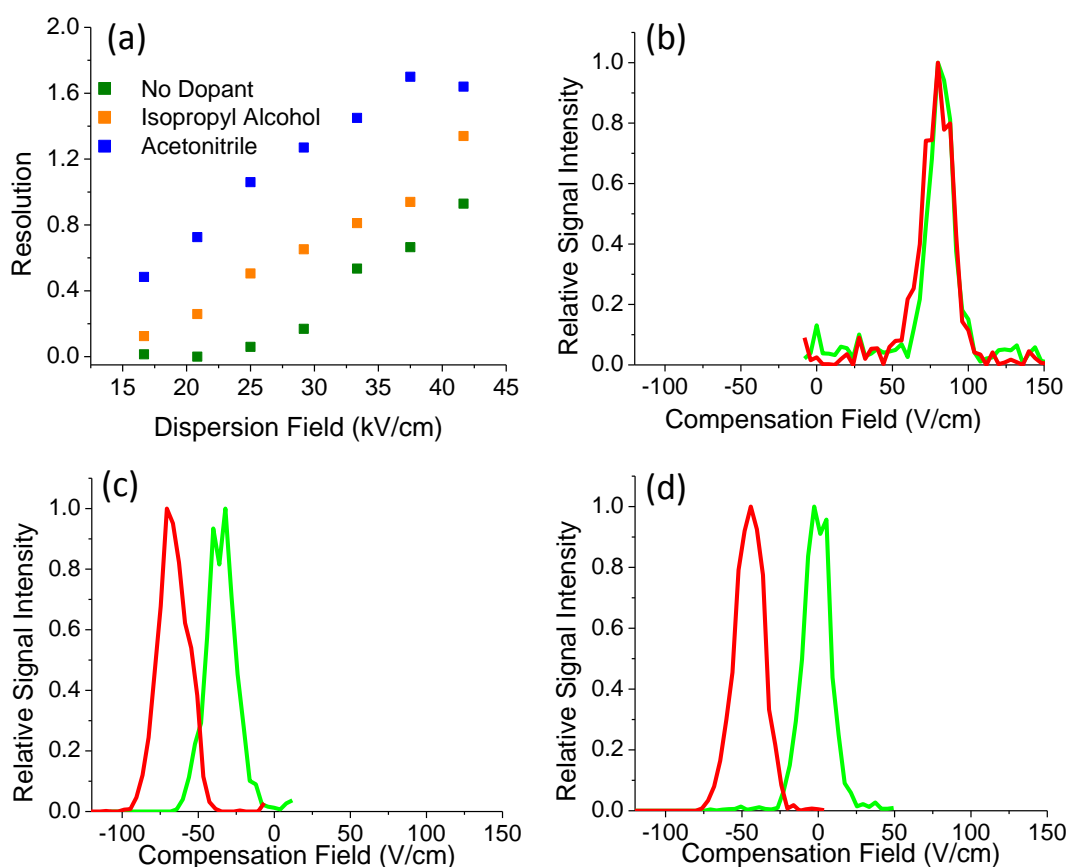


**Figure 6.4.** (a) Plot showing the effect of  $E_D$  on resolution between glucose-1-phosphate and glucose-6-phosphate peaks during DIMS scans. DIMS scan at  $E_D = 29.2$  kV/cm of glucose 1-phosphate (red) and glucose-6-phosphate (green) with (b) no dopant present in the DIMS carrier gas, (c) 0.17% (v/v) isopropyl alcohol present in the DIMS carrier gas, and (d) 0.25% (v/v) acetonitrile present in the DIMS carrier gas

fructose-6-phosphate and glucose-6-phosphate ions than between glucose-1-phosphate and glucose-6-phosphate, pointing to the impact the position of the phosphate group has on differential ion mobility. The inability of dopants to improve the separation between glucose-6-phosphate and fructose-6-phosphate ions as significantly as was observed for glucose-1-phosphate and glucose-6-phosphate agrees with the cluster-decluster model. As the deprotonation site for all three of these isomers is the phosphate group, the ability for solvent molecules to cluster around the charge might be expected to be more similar for the two species where the phosphate group is in the same position [6]. Thus, the change in differential ion mobility that occurs when dopants are added to the DIMS carrier gas is more similar for the isomers with the phosphate group located in the same position and they are not as well separated by DIMS. The separation that occurs when a mixture of the three isomers is infused for ESI is

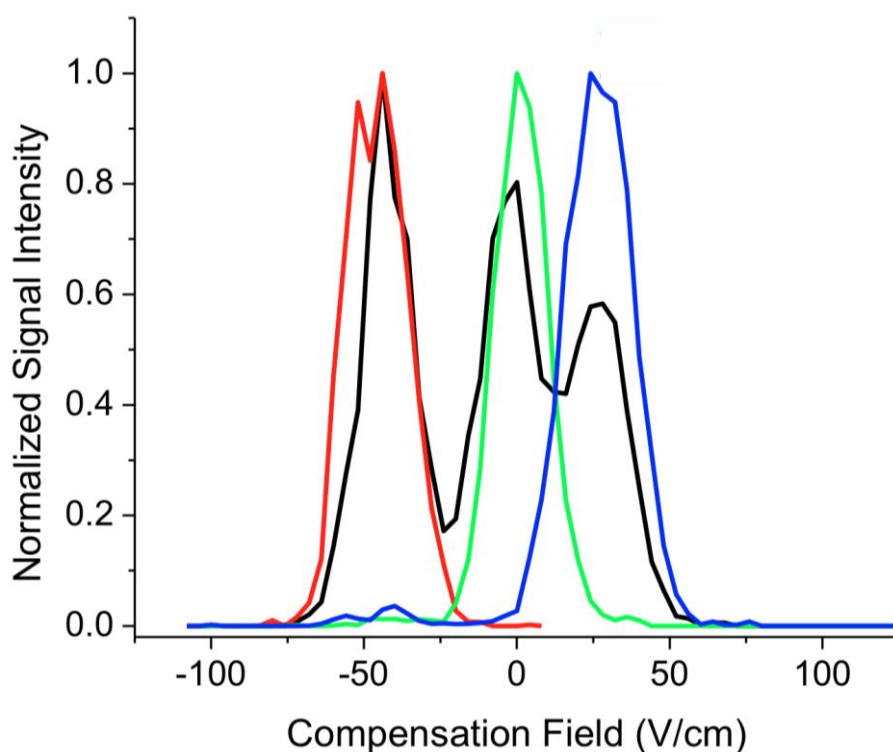


**Figure 6.5. DIMS scans of glucose-1-phosphate (red), glucose-6-phosphate (green), fructose-6-phosphate (blue) standards. A DIMS scan of the mixture of the three isomers is shown in black**

also shown in Figure 6.5, showing good agreement with the analysis of the standards and that the analysis of samples with all three isomers present could be achieved.

The ability of DIMS to separate the ions of the three isomers from each other at biological levels from a complex background was then tested by the analysis of mouse liver cell extracts. Following extraction the samples were infused for ESI and analyzed using MS/MS. The spectrum produced after isolation and fragmentation of ions of  $m/z$  259 when DIMS was not used is shown in Figure 6.6a. Comparison to the MS/MS spectra of the three isomer standards in Figure 6.6b-d suggests that a mixture of at least glucose-1-phosphate and glucose-6-phosphate is present in the mouse liver extract. DIMS analyses of the sample using 0.25% (v/v) acetonitrile, an  $E_D = 29.2$  kV/cm, and averaging 50 mass spectra at each  $E_C$  are shown in Figure 6.7a-c.

Despite the low signal-to-noise of the runs it was believed that at least two peaks were present in the DIMS scan, with a prominent peak centered at 5 V/cm and another centered at -40 V/cm. To improve the signal-to-noise of the DIMS scan, the scan was further slowed and 100 mass spectra were averaged at each  $E_C$  to produce the DIMS scans shown in Figure 6.8a. The two peaks are more clearly defined in Figure 6.8a, and were fit with two Gaussian distributions using Origin 6.0 in Figure 6.8b. The peak centered at -40 V/cm was fit by a Gaussian with a width of 18.2 V/cm whereas the peak at 5 V/cm is wider, and was fit by a Gaussian 33.8 V/cm wide. The width of the peak centered at 5 V/cm suggests the

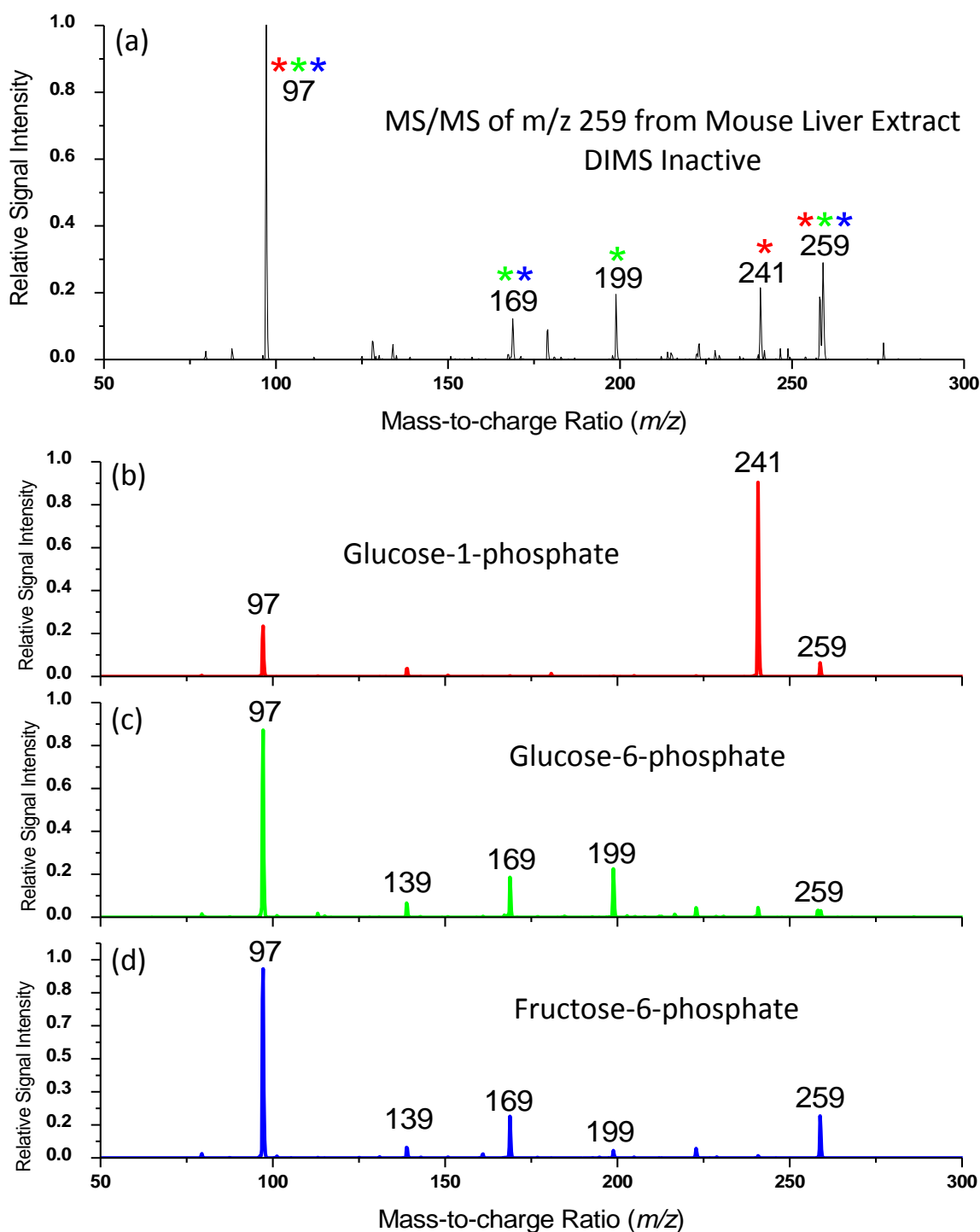


**Figure 6.6.** (a) MS/MS spectra of ions of  $m/z$  259 from mouse liver extract. Mass-to-charge ratios that align with mass-to-charge ratios from the MS/MS spectra of the standards are denoted by asterisks of the corresponding color. (b) MS/MS spectra of glucose 1-phosphate, (c) MS/MS spectra of glucose-6-phosphate, and (c) MS/MS spectra of fructose-6-phosphate

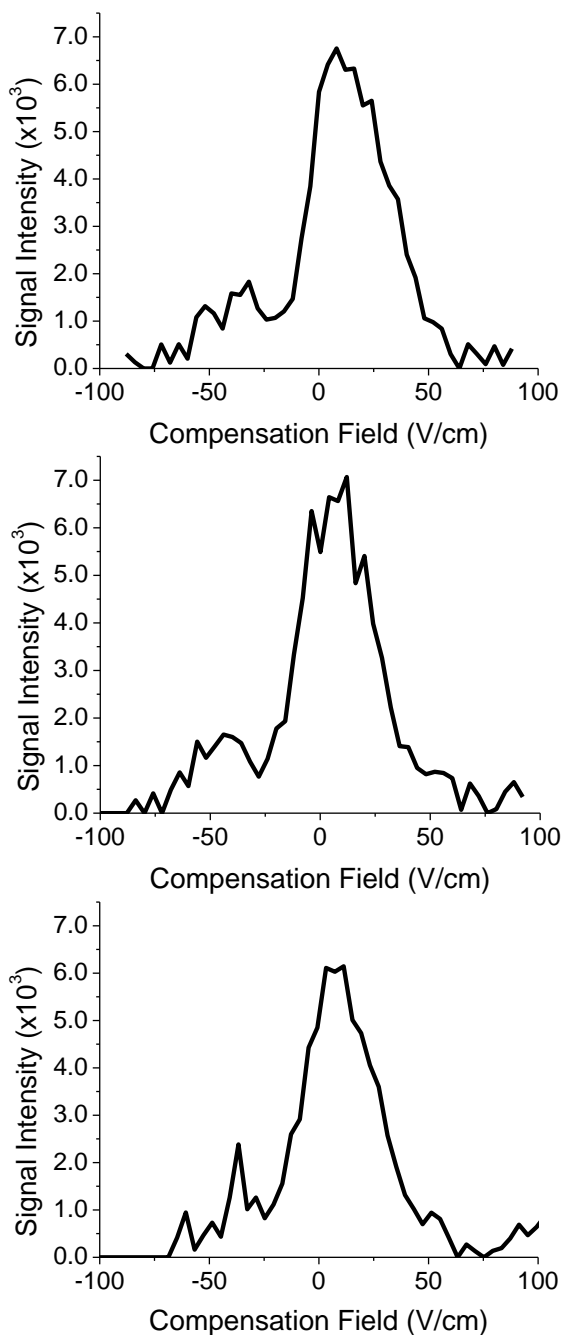


**Figure 6.7. Three DIMS scans taken with  $E_D = 29.2$  kV/cm and 0.25% (v/v) acetonitrile added to the DIMS carrier gas. Fifty mass spectra were averaged at each  $E_C$**

presence of multiple structures, as the average peak widths of the three hexose phosphate standards was between 15-20 V/cm.

Overlaying the DIMS scans of the three standards

with the DIMS scan of the mouse liver extract as in Figure 6.9 shows the peak at -40 V/cm aligns well with the peak for glucose-1-phosphate. The peak centered at 5 V/cm is less clearly defined, and could be a mixture of glucose-6-phosphate and fructose-6-phosphate where glucose-6-phosphate is present at higher concentrations.

To further confirm the identities of the species present at each  $E_C$ , MS/MS spectra were taken with the  $E_C$  kept at a constant voltage. The MS/MS spectrum taken at an  $E_C = -34$  V/cm is shown in Figure 6.10a. The most dominant fragment ion in the spectrum is detected at  $m/z$  241, with  $m/z$  97 being the next most intense peak. This

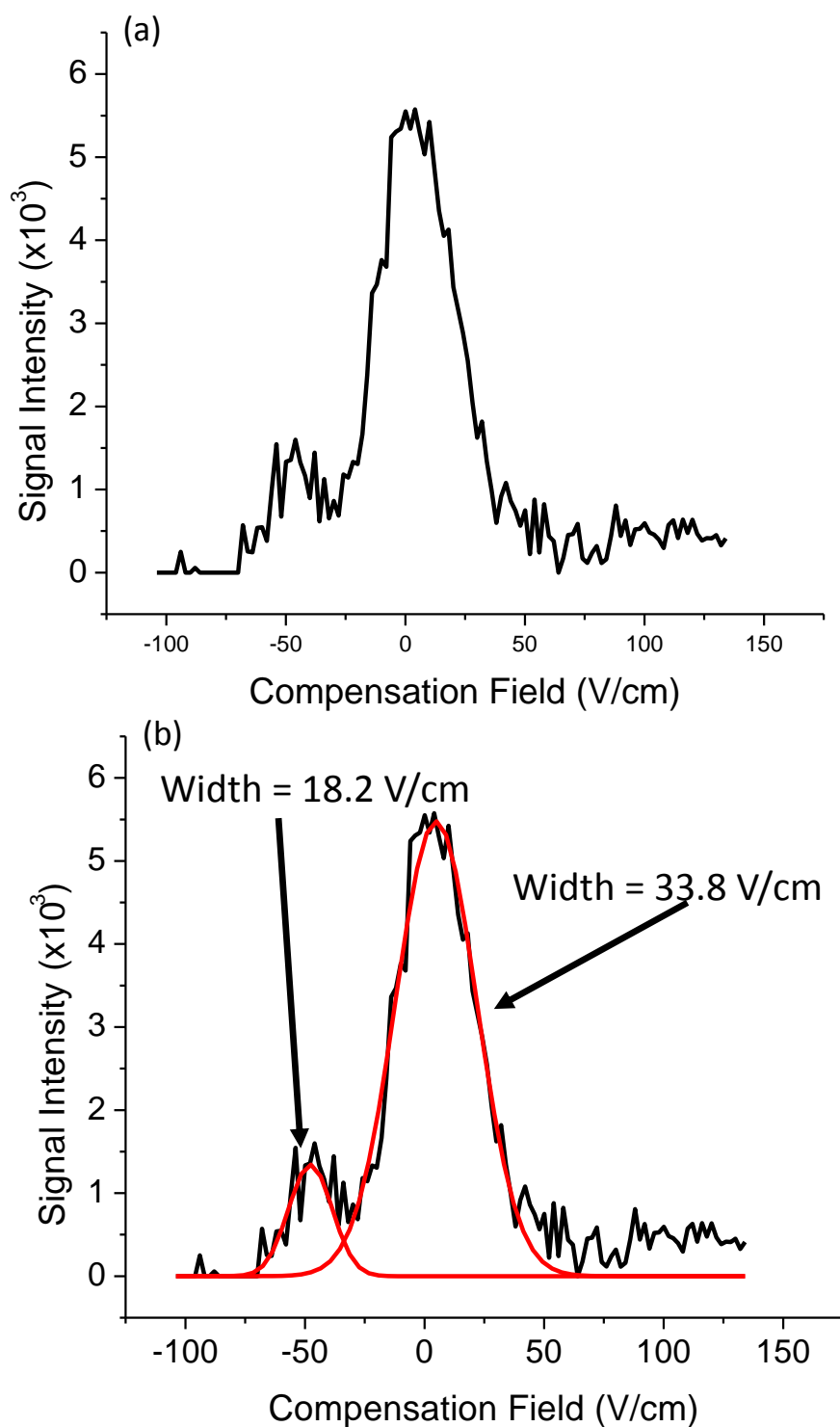


**Figure 6.8. (a) DIMS scan taken with  $E_D = 29.2$  kV/cm, 0.25% (v/v) acetonitrile added to the DIMS carrier gas, and 100 mass spectra averaged each  $E_C$  (b) DIMS scan from (a) fit with two Gaussian peaks using Origin 6.0**

spectrum matches well with the MS/MS spectrum of glucose-1-phosphate standard, shown in Figure 6.7b. The MS/MS spectra produced with an  $E_C = 3$  V/cm is shown in Figure 6.10b. In this spectrum the most prevalent fragment ion detected is at  $m/z$  97 followed by  $m/z$  199 and  $m/z$  169, which agrees with the MS/MS spectrum of glucose-6-phosphate. The lack of a peak at  $m/z$  241 shows that glucose-1-phosphate ions are not passing through the DIMS device at the  $E_C$  that selects for the other two isomers. Further attempts to differentiate between glucose-6-phosphate and fructose-6-phosphate were unsuccessful due to low signal intensities.

The ability to park at a particular  $E_C$  and detect the analyte of interest is one of the key benefits of DIMS separations. Whereas each chromatographic separation may take minutes to hours and must be used during every analysis, DIMS scans must only be

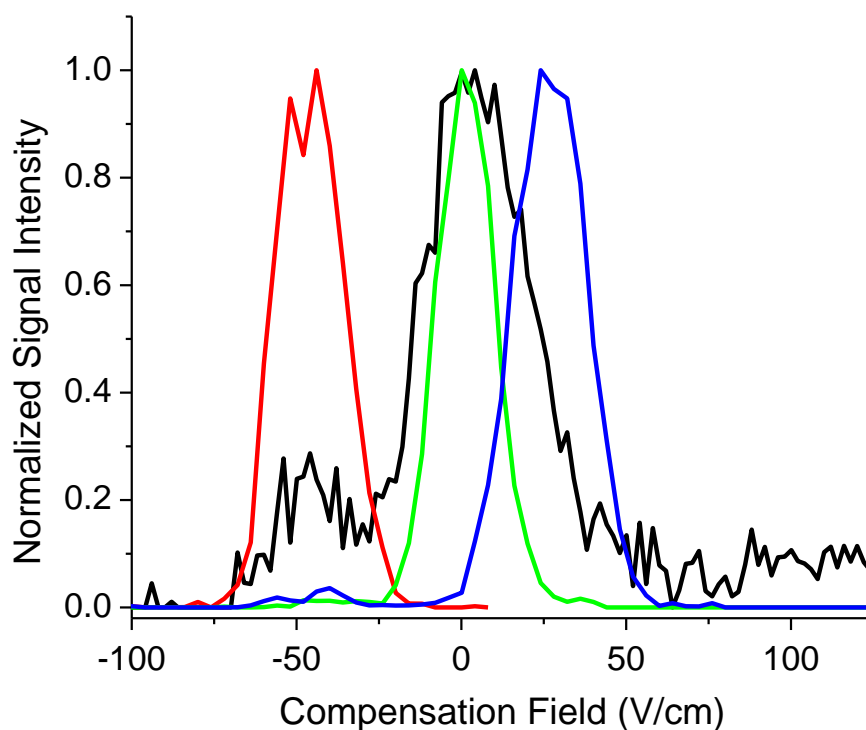


**Figure 6.9. DIMS scans of glucose-1-phosphate (red), glucose-6-phosphate (green), and fructose-6-phosphate (blue) standards overlaid with the DIMS scan of mouse liver extract (black)**



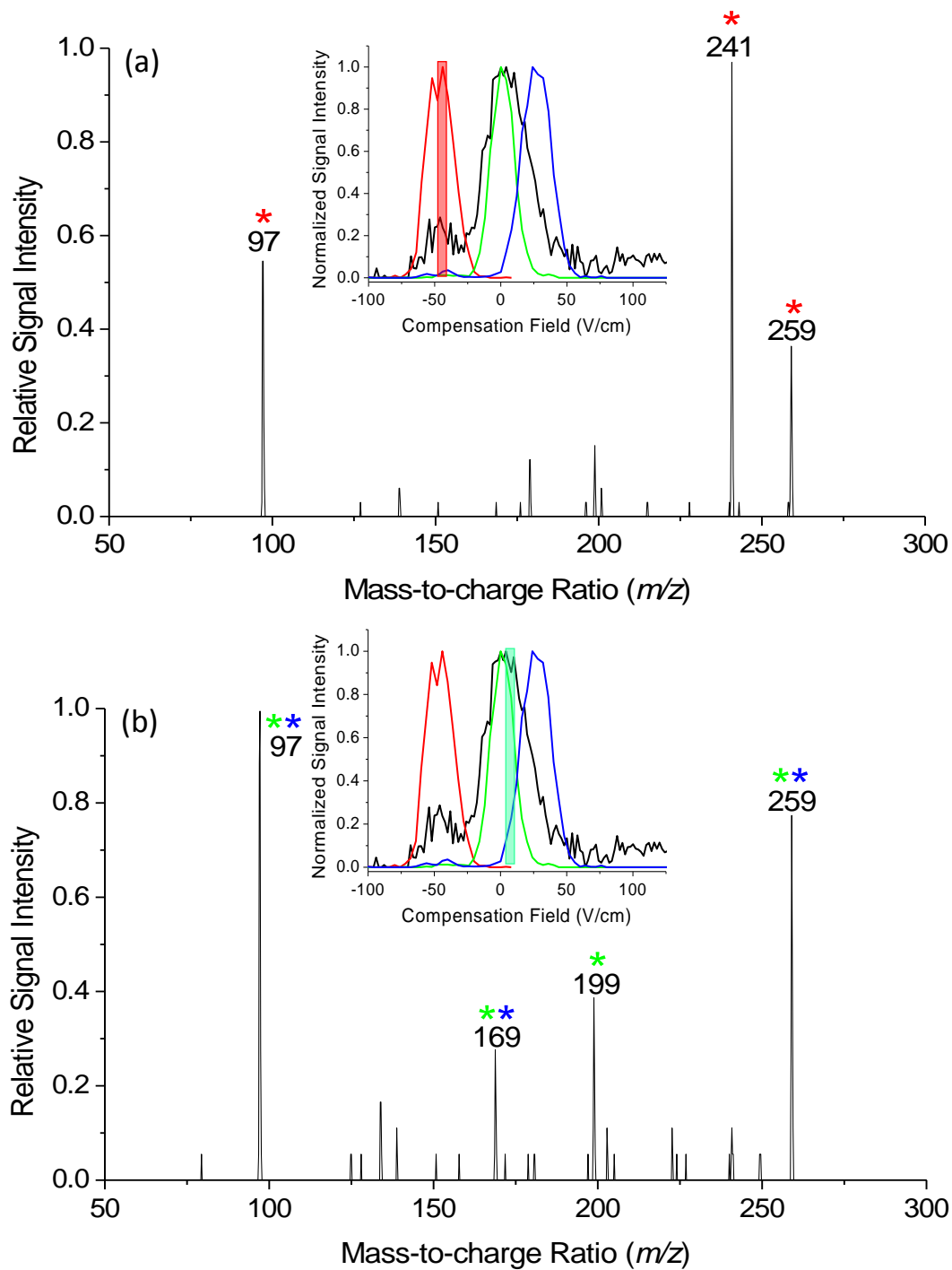


**Figure 6.10.** MS/MS spectra of  $m/z$  259 taken with (a)  $E_c = -34$  V/cm and (b)  $E_c = 3$  V/cm. Mass-to-charge ratios that also appear in the MS/MS spectra of the standards are denoted by an asterisk. The asterisk is red for mass-to-charge ratios present in the MS/MS spectra of glucose-1-phosphate, green for mass-to-charge ratios present in the MS/MS spectra of glucose-6-phosphate, and blue for mass-to-charge ratios present in the MS/MS spectra of fructose-6-phosphate

completed during the optimization steps. After the peak  $E_C$  has been determined for the analytes in question those  $E_C$  may be applied in rapid succession, with the time limiting factor being how many spectra are required at each  $E_C$  to give the desired signal-to-noise. This could also be thought of from the standpoint of the analytical duty cycle. Whereas an analyte is detected for only a small portion of the entire length of a chromatographic or electrophoretic separation, DIMS can allow for the duty cycle for the detection of an analyte, or the combined duty cycle for multiple analytes, to be nearly 100% when appropriate detection methods are used. This would allow for a much more rapid analysis of targeted compounds than traditional liquid phase separations.

#### **6.4 Summary and Conclusions**

Improvements in the ability of DIMS to separate D-glucose and its isomers D-galactose, D-fructose, and D-mannose have been shown when solvent vapors are added to the DIMS carrier gas. The ability to distinguish any one of the isomers from another has also been shown. The best separation for each combination of isomers was found to occur in the presence of solvent vapor in the carrier gas, but no one set of optimal  $E_D$  and solvent vapor was found to yield the best separations for all combinations of isomers. This fact highlights how subtle changes to the compound structure can vary the differential ion mobility, particularly when solvent vapors are present to enhance these differences.

Another point of interest that arose during the analysis of D-glucose and its isomers is the appearance of multiple peaks during DIMS scans when only one sugar isomer was thought to be present. Although a ring opening process cannot be ruled out, it is believed that the two peaks present during DIMS scans at particular  $E_D$  and solvent vapor conditions are due to the separation of  $\alpha$  and  $\beta$  anomers for D-glucose and D-galactose. The relative ratio of the two peaks

during DIMS scans aligns well with the expected ratio in solution of the two anomers. The presence of two peaks during DIMS scans of D-fructose is believed to occur due to the separation of ions formed from molecules in  $\beta$ -D-fructose pyranose and  $\beta$ -D-fructose furanose configurations. Here again the relative ratio of signal intensities for the two peaks during DIMS scans and the expected ratio in solution aligns.

Using the previously summarized work separating D-glucose and its isomers as a foundation, a DIMS method was then developed for the separation of three hexose phosphates that is more rapid than the LC methods typically used to separate these compounds. The use of acetonitrile as the solvent vapor added to the DIMS carrier gas was determined to yield the best separation between glucose-1-phosphate and glucose-6-phosphate, with adequate separation of glucose-6-phosphate and fructose-6-phosphate. This methodology was then applied to the separation of the compounds in a mouse liver extract. DIMS scans of the mouse liver extract contained two peaks for  $m/z$  259, which were believed arise from glucose-1-phosphate ions and a combination of glucose-6-phosphate and fructose-6-phosphate ions. MS/MS experiments of the standards and the mouse liver extract were used to confirm the identities of the species present at -34 V/cm and 3 V/cm. Overall, this method would allow for the rapid distinction between the analytes, particularly when using the ability to park at the distinctive  $E_C$  of each analyte.

## REFERENCES

1. Krylova, N.; Krylov, E.; Eiceman, G. A.; Stone, J. A. Effect of Moisture on the Field Dependence of Mobility for Gas-Phase Ions of Organophosphorus Compounds at Atmospheric Pressure with Field Asymmetric Ion Mobility Spectrometry. *J. Phys. Chem. A*. **2003**, *107*, 3648-3654.
2. Eiceman, G. A.; Krylov, E. V.; Krylova, N. S.; Nazarov, E. G.; Miller, R. A. Separation of Ions from Explosives in Differential Mobility Spectrometry by Vapor-Modified Drift Gas. *Anal. Chem.* **2004**, *76*, 4937-4944.
3. Levin, D. S.; Vouros, P.; Miller, R. A.; Nazarov, E. G.; Morris, J. C. Characterization of Gas-Phase Molecular Interactions of Differential Mobility Ion Behavior Utilizing an Electrospray Ionization-Differential Mobility-Mass Spectrometer System. *Anal. Chem.* **2006**, *78*, 96-106.
4. Schneider, B.; Covey, T.; Coy, S.; Krylov, E.; Nazarov, E. Chemical Effects in the Separation Process of a Differential Mobility/Mass Spectrometer System. *Anal. Chem.* **2010**, *82*, 1867-1880.
5. Rorrer, L. C. R. L. C.; Yost, R. A. Solvent Vapor Effects on Planar High-Field Asymmetric Waveform Ion Mobility Spectrometry. *Int. J. Mass Spectrom.* **2011**, *300*, 173-181.
6. Campbell, J. L.; Zhu, M.; Hopkins, W. S. Ion-Molecule Clustering in Differential Mobility Spectrometry: Lessons Learned from Tetraalkylammonium Cations and their Isomers. *J. Am. Soc. Mass Spectrom.* **2014**, *25*, 1583-1591.
7. Liu, C.; Le Blanc, J.; Shields, J.; Janiszewski, J.; Ieritano, C.; Ye, G.; Hawes, G.; Hopkins, W.; Campbell, J. Using Differential Mobility Spectrometry to Measure Ion Solvation: An Examination of the Roles of Solvent and Ionic Structures in Separating Quinoline-Based Drugs. *Analyst.* **2015**, *140*, 6897-6903.
8. Rorrer III, L.; Yost, R. Solvent Vapor Effects in Planar High-Field Asymmetric Waveform Ion Mobility Spectrometry: Solvent Trends and Temperature Effects. *Int. J. Mass Spectrom.* **2015**, *378*, 336-346.
9. Shvartsburg, A. A. Differential Ion Mobility Spectrometry : Nonlinear Ion Transport and Fundamentals of FAIMS; CRC Press, Boca Raton, 2009.
10. Lowenthal, M.; Kilpatrick, E.; Phinney, K. Separation of Monosaccharides Hydrolyzed from Glycoproteins without the Need for Derivatization. *Anal. Bioanal. Chem.* **2015**, *407*, 5453-5462.

11. Yan, J.; Shi, S.; Wang, H.; Liu, R.; Li, N.; Chen, Y.; Wang, S. Neutral Monosaccharide Composition Analysis of Plant-Derived Oligo and Polysaccharides by High Performance Liquid Chromatography. *Carbohydrate Polymers*. **2016**, *136*, 1273-1280.
12. Ricochon, G.; Paris, C.; Girardin, M.; Muniglia, L. Highly Sensitive, Quick and Simple Quantification Method for Mono and Disaccharides in Aqueous Media using Liquid Chromatography–atmospheric Pressure Chemical Ionization–mass Spectrometry (LC–APCI–MS). *J. Chromatogr. B*. **2011**, *879*, 1529-1536.
13. Hammad, L.; Derryberry, D.; Jmeian, Y.; Mechref, Y. Quantification of Monosaccharides through Multiple-Reaction Monitoring Liquid Chromatography/Mass Spectrometry using an Aminopropyl Column. *Rapid Commun. Mass Spectrom.* **2010**, *24*, 1565-1574.
14. Fessenden, R.; Fessenden, J.; Logue, M. Organic Chemistry, 6th ed.; Brooks/Cole Publishing Company, Pacific Grove, CA, 1998; p. 1170.
15. Coninero, E.; Lesarri, A.; Ecija, P.; Basterretxea, F.; Grabow, J.; Fernandez, J.; Castano, F. Ribose found in the Gas Phase. *Angew. Chem. Int. Ed.* **2012**, *51*, 3119-3124.
16. Szczepaniak, M.; Moc, J. Conformational Studies of Gas-Phase Ribose and 2-Deoxyribose by Density Functional, Second Order PT and Multi-Level Method Calculations: The Pyranoses, Furanoses, and Open-Chain Structures. *Carbohydrate Research*. **2014**, *384*, 20-36.
17. Azofra, L.; Quesada-Moreno, M.; Alkorta, I.; Aviles-Moreno, J.; Loez-Gonzalez, J.; Elguero, J. Carbohydrates in the Gas Phase: Conformational Preference of D-Ribose and 2-Deoxy-D-Ribose. *New J. Chem.* **2014**, *38*, 528-538.
18. Alonso, J.; Lzoya, M.; Pena, I.; Lopez, J.; Cabezas, C.; Mata, S.; Blanco, S. The Conformational Behaviour of Free D-Glucose- at Last. *Chem. Sci.* **2014**, *5*, 515-522.
19. Cocinero, E.; Lesarri, A.; Ecija, P.; Cimas, A.; Davis, B.; Basterretxea, F.; Fernandez, J.; Castano, F. Free Fructose is Conformationally Locked. *J. Am. Chem. Soc.* **2013**, *135*, 2845-2852.
20. Collins, P.; Ferrier, R. Monosaccharides; John Wiley & Sons, New York, 1995.
21. Hernandez, O.; Isenberg, S.; Steinmatz, V.; Glish, G.; Maitre, P. Probing Mobility-Selected Saccharide Isomers: Selective Ion– Molecule Reactions and Wavelength-Specific IR Activation. *J. Phys. Chem. A*. **2015**, *119*, 6057-6064.

22. Antonio, C.; Larson, T.; Gilday, A.; Graham, I.; Bergstrom, E.; Thomas-Oates, J. Quantification of Sugars and Sugar Phosphates in *Arabidopsis Thaliana* tissues using Porous Graphitic Carbon Liquid Chromatography-Electrospray Ionization Mass Spectrometry. *J. Chromatogr. A*. **2007**, *1172*, 170-178.
23. Wamelink, M.; Struys, E.; Huck, J.; Roos, B.; van der Knaap, M.; Jakobs, C.; Verhoeven, N. Quantification of Sugar Phosphate Intermediates of the Pentose Phosphate Pathway by LC–MS/MS: Application to Two New Inherited Defects of Metabolism. *J. Chromatogr. B*. **2005**, *823*, 18-25.
24. Carpenter, M.; Joyce, N.; Butler, R.; Genet, R.; Timmerman-Vaughan, G. A Mass Spectrometric Method for Quantifying C3 and C6 Phosphorylation of Starch. *Anal. Biochem.* **2012**, *431*, 115-119.
25. Xu, Y.; Lu, W.; Rabinowitz, J. Avoiding Misannotation of in-Source Fragmentation Products as Cellular Metabolites in Liquid Chromatography–Mass Spectrometry-Based Metabolomics. *Anal. Chem.* **2015**, *87*, 2273-2281.
26. Luo, B.; Groenke, K.; Takors, R.; Wandrey, C.; Oldiges, M. Simultaneous Determination of Multiple Intracellular Metabolites in Glycolysis, Pentose Phosphate Pathway and Tricarboxylic Acid Cycle by Liquid Chromatography–mass Spectrometry. *J. Chromatogr. A*. **2007**, *1147*, 153-164.
27. Purves, R.; Ozog, A.; Amborse, S.; Prasad, S.; Belford, M.; Dunyach, J. Using Gas Modifiers to significantly Improve Sensitivity and Selectivity in a Cylindrical FAIMS Device. *J. Am. Soc. Mass Spectrom.* **2014**, *25*, 1274-1284.

## **CHAPTER 7: SUMMARY AND FUTURE DIRECTIONS**

### **7.1 General Summary**

The work presented in this dissertation has been focused on fundamental studies of DIMS separations coupled to mass spectrometry. After an introduction to DIMS and the variables that affect the separation capabilities of DIMS, an explanation of the experimental designs of each experiment is included. The work goes on to discuss the importance of the mass spectrometer desolvation gas flow rate and temperature in separations, and then examines how internal energy can be deposited into ions as they travel through a DIMS device. The factors that influence the amount of internal energy gained and cause intra-DIMS fragmentation are also described. The development and use of linked scans are then explained in Chapter 5, as are the merit of metrics such as resolving power, resolution, and peak capacity to describe DIMS separations. Following these fundamental based discussions, the application of adding solvent vapors to the DIMS carrier gas to improve the separation of sugar isomers is described. The current chapter provides a summary of each chapter along with describing potential future directions for the work.

### **7.2 Effects of Desolvation Gas Flow Rate and Temperature on Differential Ion Mobility Spectrometry Separations**

#### **7.2.1. Summary**

Chapter 3 is a description of the work completed investigating the effects of the mass spectrometer desolvation gas on DIMS separations. The desolvation gas flow rate and temperature were varied while using ion sources that introduce different amounts of solvent into the region in front of the inlet to the DIMS device. Without high enough desolvation gas flow

rates and/or temperatures, solvent droplets would be drawn into the DIMS device at a high enough concentration to affect the transit of ions through the DIMS device via a cluster-decluster process. These changes would then be measurable as changes to the characteristic  $E_C$  of the ions or the peak widths during DIMS scans.

No differences in characteristic  $E_C$  were observed for ions of multiple analytes generated by ESI and nESI using desolvation gas settings of 5.0 L/minute and temperature settings between 200 and 300 °C. However, both ion sources introduce solvent in front of the DIMS device and differences in evaporation/desolvation might just be immeasurable with the current experimental setup. To further investigate what desolvation gas flow and temperature settings were required to prevent DIMS separations from being affected by solvent, the peak characteristics during DIMS scans were compared for ions formed by LTPI and ESI. These experiments were conducted by changing the desolvation gas flow rate between 1.0, 3.0, and 5.0 L/minute with a temperature setting of 300 °C, and also by varying the temperature setting between 100, 200, and 300 °C with a desolvation gas flow rate of 5.0 L/minute. In summary, desolvation gas flow rate was found to be the critical variable in keeping solvent molecules from entering the DIMS device. Only a desolvation gas flow rate of 1.0 L/minute caused measurable differences in characteristic  $E_C$  and peak widths during DIMS scans between ions formed by ESI and LTPI.

#### 7.2.2. Future Directions

Understanding the roles the mass spectrometer desolvation gas temperature and flow rate play when using DIMS will facilitate future work with different or novel ion sources. Work in our lab has included the development of ion sources such as LTPI, extractive electrospray ionization (EESI), and paper spray ionization. Each ion source has its own set of optimum



conditions with respect to desolvation gas flow and temperature, and this work gives a baseline for the required conditions if these ion sources are to be coupled to a DIMS device.

An ongoing project in the Glish laboratory is the analysis of ions formed after the pyrolysis of natural polymers. DIMS separations prior to mass analysis can help distinguish between isomeric compounds produced during pyrolysis. Ion sources in development that will be used with complex pyrolysis samples are EESI and a newly developed coaxial EESI. Each EESI setup uses different solvent and nebulizer gas flows, and is likely to have its own combination of optimal desolvation gas settings that improve desolvation and ion sampling. These values can be used in combination with the work presented in Chapter 3 of this work to facilitate the achievement of useful results.

There is also potential for DIMS separations to be coupled to paper spray ionization of complex samples. The analysis of pesticides in commercial formulations has been a challenging issue, and while the use of paper spray minimizes sample preparation steps, the complex mixtures of ions generated can be difficult to analyze by mass spectrometry alone. A DIMS separation step prior to mass analysis might be beneficial, but desolvation of the droplets formed from the paper tip would be necessary. The work presented in Chapter 3 will reduce the optimization necessary for coupling paper spray and DIMS, as the effects of desolvation flow rate and temperature on DIMS separations have been shown.

### **7.3 Characterization of Variables Affecting Internal Energy Deposition Inside a Differential Ion Mobility Spectrometer**

#### **7.3.1. Summary**

The work discussed in Chapter 4 examined the unexpected intra-DIMS fragmentation of multiply charged peptide ions. These fragmentation occurred due to increases in the internal energy of the ions as they passed through the DIMS device and underwent energetic collisions

with the DIMS carrier gas. The variables that affected the amount of internal energy deposited into both  $[M+3H]^{3+}$  ions of bradykinin and  $[M+2H]^{2+}$  ions of GLISH were investigated. It was observed that the amount of fragmentation increased as  $E_D$  was raised, and that ions with a higher charge state were more likely to fragment. Additionally, the fragmentation patterns observed are similar to those observed during CID in an ion trap mass spectrometer. Thus, it is believed that internal energy is deposited in small increments in DIMS, which causes intra-DIMS fragmentation to occur via the lowest energy pathway.

Intra-DIMS fragmentation was also studied as a function of the temperature of the mass spectrometer desolvation gas, and therefore as a function of the internal energy of the ions before they enter the DIMS device. As expected, the amount of fragmentation observed at any  $E_D$  for both the  $[M+3H]^{3+}$  ions of bradykinin and  $[M+2H]^{2+}$  ions of GLISH was related the internal energy of the ions prior to their entering the DIMS device. Using these studies the relationship between  $E_D$  and the amount of internal energy added to the ions was determined. Each increase in  $E_D$  was observed to raise the internal energy of the  $[M+3H]^{3+}$  ions of bradykinin more than of the  $[M+2H]^{2+}$  ions of GLISH, although bradykinin has significantly more degrees of freedom over which to spread the energy. The higher charge state of the bradykinin ion is believed to be the cause for this greater internal energy increase as  $E_D$  is increased.

Changing the composition of the DIMS carrier gas also allowed for differences in the amount of intra-DIMS fragmentation to be observed. The addition of helium or argon to the typically nitrogen DIMS carrier gas caused more fragmentation, whereas the addition of carbon monoxide had the opposite effect. Using the same principles as during the temperature study, the differences in internal energy added by each carrier gas composition was calculated. Measuring intra-DIMS fragmentation at three different levels of carbon monoxide presence in the carrier

gas allowed for the observation that the relationship between the  $E_D$  necessary for a 50% fragmentation efficiency of the  $[M+3H]^{3+}$  ions of bradykinin and the amount of carbon monoxide present in the carrier gas is linear.

The effects changing the DIMS carrier gas temperature and composition have on the separation capabilities of the DIMS device were also discussed. With regards to the peptide ions studied in this work, the separation ability of the DIMS device will be greatest at those conditions that most facilitate fragmentation. Based on this observation, the optimum use of the ability to vary internal energy deposition through manipulation of the carrier gas temperature and composition must be determined on a case-by-case scale.

### 7.3.2. Future Directions

Along with the intra-DIMS fragmentation of the peptides bradykinin and GLISH, Chapter 4 also describes the methods that can be used to modulate the amount of internal energy added to an ion as it travels through a DIMS device. That work can be applied to systems where preserving ion structure while performing a separation is of importance. One example might be a DIMS-IMS-MS experiment in which the IMS device can provide collisional cross section, but DIMS is required to provide separation. In that case a more gentle DIMS separation might be applied so that isomerization due to increases in internal energy does not occur.

Rather than use the current work in an applied sense, the work can also be used as a starting point for further characterization of the internal energy deposition into ions. Polar carbon monoxide reduces fragmentation significantly compared to non-polar gases, and this stream of work can be continued to include even more polar compounds through the use of the system used in Chapter 6. The addition of vapors from solvents such as methanol, isopropyl alcohol, or acetonitrile (albeit at much lower concentrations than the gases were added) might further reduce

the internal energy added in DIMS. However, as molecules the size of peptides are not typically considered to participate in the cluster-decluster process described in Chapter 1, another interesting study might be to look at these effects with small molecules that do participate in the proposed cluster-decluster mechanism. The internal energy addition for an ion that undergoes the cluster-decluster process could be significantly changed if the solvent molecules surrounding the ion absorb a portion of the energy gained by collisions with the carrier gas.

## **7.4 Improved Differential Ion Mobility Separations using Linked scans of Carrier Gas and Compensation Field**

### **7.4.1. Summary**

The development of linked scans, a version of DIMS scans during which the carrier gas composition and the compensation field are scanned simultaneously, is discussed in Chapter 5. The iterations of how linked scans were implemented are explained, including issues with how the scans should be designed and executed. The process of initially using resolving power as the metric of choice to characterize the separations and the issues that arose are explored, including the ability to achieve resolving powers greater than 7900. The transition away from resolving power to metrics including resolution and peak capacity is also discussed.

Linked scans are then compared to compensation field scans with constant helium using resolution, peak capacity, and signal intensity. The >50% improvement in resolution between peaks from different charge states of ubiquitin are discussed. Those experiments were followed by work done that increased peak capacity by 38% for a tryptic digest of BSA when using linked scans. The origin of these improvements is discussed, and the improvement in signal intensity during linked scans versus compensation field scans with constant helium is reported for the analyses of both ubiquitin and the tryptic digest of BSA.

#### 7.4.2. Future Directions

The improvements linked scans provide in resolution, peak capacity, and signal intensity over compensation field scans with constant helium provide potential for linked scans to be applied to the analyses of complex mixtures. One such complex mixture is the pyrolysis of natural polymers. The ions formed from these mixtures are often isomeric, and mass spectrometry alone is not sufficient for the identification of species present in the sample. Linked scans would provide improved separations compared to compensation field scans with constant helium as a separation step prior to mass analysis. Additionally, the use of helium typically causes significant losses in signal intensity because many of the ions formed after pyrolysis are relatively small. Here again linked scans provide improvement, as signal intensity is greater during linked scans than compensation field scans with constant helium. Aside from improving detection ability, the better signal intensity also provides the ability to gather improved quality MS/MS spectra. If linked scans of pyrolysis samples with helium and nitrogen still yield insufficient separations, the separation abilities of linked scans could be further improved through the implementation of other carrier gas combinations. The use of mixtures including hydrogen have been shown to yield greater improvements in separation abilities than helium and would not require changes to the current system [1].

### **7.5 Separations of Sugar Isomers using Differential Ion Mobility Spectrometry with Solvent Dopants**

#### 7.5.1. Summary

In Chapter 6 the effects of adding solvent vapors to the DIMS carrier gas were investigated for the separation of the ions formed from isomeric sugar molecules. Using glucose and three of its biologically relevant hexose isomers, the addition of solvent vapors provided an improvement in separation for each set of two isomers; however, the optimal conditions were

dependent on the particular isomers to be separated. These differences in optimal solvent vapor and  $E_D$  point to the fact that subtle differences in structure that can make a large impact on how solvent molecules cluster to ions during DIMS analyses and how the results can be difficult to predict prior to the experiment. During these studies it was also observed that different combinations of solvent vapor and  $E_D$  introduced the separation of anomers of both D-glucose and D-galactose. DIMS scans of D-fructose also produced two peaks at particular solvent and  $E_C$  combinations, but these ion populations were assigned to  $\beta$ -D-fructose pyranose and  $\beta$ -D-furanose structures. Based on these findings, no one combination of instrumental parameters can be concluded as ideal, but the addition of solvent vapors to the DIMS carrier gas was determined to improve the separation between the sugar isomers studied.

The information gained from the studies of glucose and related sugars was then applied to the separation the phosphorylated sugars glucose-1-phosphate, glucose-6-phosphate, and fructose-6-phosphate. These compounds are produced at the cellular level during glycogenolysis, but are difficult to separate via traditional methods such as liquid chromatography. In this work a method was developed using acetonitrile as the solvent dopant to separate these three isomers. Additionally, glucose-1-phosphate and glucose-6-phosphate were separated at biologically relevant concentrations from a sample of mouse liver extract. Thus, DIMS was shown as a potential option to facilitate the differentiation between these compounds in complex samples.

#### 7.5.1. Future Directions

The analysis of these phosphorylated sugars from biological samples using DIMS still has areas where improvements can be made. For example, the addition of isotopically labeled molecules to samples would allow for quantitation of these components. Additionally, the separation of glucose-6-phosphate and fructose-6-phosphate could be further optimized.

Although the two are separated at the  $E_D$  used in this work, improved separation would facilitate differentiation at the low and unequal quantities potentially present in samples. The separation of fructose 1,6-bisphosphate and fructose 2,6-bisphosphate is another system where DIMS separations might be valuable. Similar to the phosphorylated monosaccharides discussed, these compounds are only separated by lengthy chromatographic analyses, and a rapid DIMS separation could increase throughput [2,3].

The use of dopants also added a level of chemical specificity to the ability of DIMS to separate ions of interest from other ions in a complex mixture. This capability could be applied to the analysis of ions formed after the pyrolysis of natural polymers. One example of a natural polymer is cellulose, which consists of repeating D-glucose units. Although the ionization of the pyrolysate from these samples results in complex mixtures, dopants might shift the characteristic  $E_C$  of ions with structures resembling glucose in a way that is similar to glucose analyzed from a simpler matrix. This practice could then be applied to other groups of compounds that have similar structures or contain the same functional groups, as these factors have been shown to affect the differential mobility of ions similarly when solvent vapors are added to the DIMS carrier gas.

## REFERENCES

1. Shvartsburg, A.; Smith, R. Accelerated High-Resolution Differential Ion Mobility Separations using Hydrogen. *Anal. Chem.* **2011**, 83, 9159-9166.
2. Sekiguchi, Y.; Mitsuhashi, N.; Kokaji, T.; Miyakoda, H.; Mimura, T. Development of a Comprehensive Analytical Method for Phosphate Metabolites in Plants by Ion Chromatography Coupled with Tandem Mass Spectrometry. *J. Chromatogr. A.* **2005**, 1085, 131-136.
3. Arrivault, S.; Guenther, M.; Ivakov, A.; Feil, R.; Voslosh, D.; Van Dongen, J.; Stitt, M. Use of Reverse-Phase Liquid Chromatography, Linked to Tandem Mass Spectrometry, to Profile the Calvin Cycle and Other Metabolic Intermediates in Arabidopsis Rosettes at Different Carbon Dioxide Concentrations. *The Plant Journal.* **2009**, 59, 824-839.